SUSTAINABLE CARBON SEQUESTRATION: INCREASING CO_2-STORAGE EFFICIENCY THROUGH A CO_2-BRINE DISPLACEMENT APPROACH

A Dissertation

by

OYEWANDE AYOKUNLE AKINNIKAWE

Submitted to the Office of Graduate Studies of
Texas A&M University
in partial fulfillment of the requirements for the degree of

DOCTOR OF PHILOSOPHY

August 2012

Major Subject: Petroleum Engineering

SUSTAINABLE CARBON SEQUESTRATION: INCREASING CO_2-STORAGE EFFICIENCY THROUGH A CO_2-BRINE DISPLACEMENT APPROACH

A Dissertation

by

OYEWANDE AYOKUNLE AKINNIKAWE

Submitted to the Office of Graduate Studies of
Texas A&M University
in partial fulfillment of the requirements for the degree of

DOCTOR OF PHILOSOPHY

Approved by:

Chair of Committee, Christine Ehlig-Economides
Committee Member, Maria Barrufet
Hisham Nasr-El-Din
Mark Holtzapple
Head of Department, A. Daniel Hill

August 2012

Major Subject: Petroleum Engineering

ABSTRACT

Sustainable Carbon Sequestration: Increasing CO_2-Storage Efficiency through a CO_2-Brine Displacement Approach. (August 2012)

Oyewande Ayokunle Akinnikawe, B.S., Obafemi Awolowo University;

M.S., Illinois Institute of Technology

Chair of Advisory Committee: Dr. Christine A. Ehlig-Economides

CO_2 sequestration is one of the proposed methods for reducing anthropogenic CO_2 emissions to the atmosphere and therefore mitigating global climate change. Few studies on storing CO_2 in an aquifer have been conducted on a regional scale. This study offers a conceptual approach to increasing the storage efficiency of CO_2 injection in saline formations and investigates what an actual CO_2 storage project might entail using field data for the Woodbine aquifer in East Texas.

The study considers three aquifer management strategies for injecting CO_2 emissions from nearby coal-fired power plants into the Woodbine aquifer. The aquifer management strategies studied are bulk CO_2 injection, and two CO_2-brine displacement strategies.

A conceptual model performed with homogeneous and average reservoir properties reveals that bulk injection of CO_2 pressurizes the aquifer, has a storage efficiency of 0.46% and can only last for 20 years without risk of fracturing the CO_2 injection wells. The CO_2-brine displacement strategy can continue injecting CO_2 for as many as 240 years until CO_2 begins to break through in the production wells. This offers 12 times greater CO_2 storage efficiency than the bulk injection strategy.

A full field simulation with a geological model based on existing aquifer data validates the storage capacity claims made by the conceptual model. A key feature in the geological model is the Mexia-Talco fault system that serves as a likely boundary between the saline aquifer region suitable for CO_2 storage and an updip fresh water region. Simulation results show that CO_2 does not leak into the fresh water region of the

aquifer after 1000 years of monitoring if the faults have zero transmissibility, but a negligible volume of brine eventually gets through the mostly sealing fault system as pressure across the faults slowly equilibrates during the monitoring period. However, for fault transmissibilities of 0.1 and 1, both brine and CO_2 leak into the fresh water aquifer in increasing amounts for both bulk injection and CO_2-brine displacement strategies. In addition, brine production wells draw some fresh water into the saline aquifer if the Mexia-Talco fault system is not sealing.

A CO_2 storage project in the Woodbine aquifer would impact as many as 15 counties with high-pressure CO_2 pipelines stretching as long as 875 km from the CO_2 source to the injection site. The required percentage of power plant energy capacity was 7.43% for bulk injection, 7.9% for the external brine disposal case, and 10.2% for the internal saturated brine injection case. The estimated total cost was \$0.00132–\$0.00146/kWh for the bulk injection, \$0.00191–\$0.00211/kWh for the external brine disposal case, and \$0.0019–\$0.00209/kWh for the internal saturated brine injection case.

ACKNOWLEDGEMENTS

I would like to thank my advisor Christine Ehlig-Economides for her invaluable guidance and support. It has been a great experience working with her and I have learned a lot from her, which has helped me in my academic, professional and personal development. Indeed she has been an excellent mentor and a great role model to me. I am particularly grateful for the attention she gives to her students despite tight schedules and the supportive, friendly, and collaboratively work environment that she helped create.

I would like to thank my committee members, Maria Barrufet, Hisham Nasr-El-Din, and Mark Holtzapple for their help, support, and patience. My work has been improved by their insights and suggestions.

I would like to thank the Computer Modeling Group (CMG) for providing the license of the software package. I am particularly grateful to Bob Brugman from CMG for his prompt response when I needed help with the GEM GHG (Green House Gas) module of CMG. Special thanks go to David, Stuart, Brandon, and Jason from the IT support group at the Department of Petroleum Engineering Texas A&M University.

Without my family, I would not be here in the first place. I am indeed grateful to them for their love, support, and encouragement during my PhD program. I will like to thank my dad Francis and my mum Josephine for their incessant prayers and comforting words. I am also appreciative of my brothers Deji and Ayo, and my wonderful sister Bose for the assistance and suggestions they provided over the course of my program.

Finally, I would like to thank my wife Simisola for her patience, support, and encouragement.

NOMENCLATURE

C_{Comp}	capital cost of compressor ($)
C_{pump}	capital cost of pump ($)
CR	compression ratio of each stage (dimensionless)
D	pipeline diameter (in)
D_{pipe}	injection tubing diameter (m)
ff	fraction of completion of the well in the gridblock
F_r	fanning friction factor (dimensionless)
g	acceleration due to gravity (m^2/s)
h	gridblock thickness in the well direction (m)
H	aquifer depth (m)
I	injectivity bbl/(d·psi)
J	productivity,bbl/(d·psi)
k	effective permeability in the plane perpendicular to the well direction (mD)
$K_{r,CO2}$	relative permeability to CO_2 (dimensionless)
K_{rg}	relative permeability to gas (dimensionless)
$k_{r,SCO2}$	relative permeability to CO_2 in the dry zone (dimensionless)
K_{rw}	relative permeability to water (dimensionless)
k_s	(C_p/C_v) = average ratio of specific heats of CO_2 for each individual stage
m	CO_2 mass flowrate (tonnes/day)
m_{train}	CO_2 mass flow rate through each compressor (kg/s)
M	molecular weight of CO_2 (kg/kmol)
N_{stage}	number of compressor stages

N_{train} number of parallel compressor trains

N_{well} number of injection wells

$\bar{P}$ average reservoir pressure (psi)

P_{ave} average pressure in pipeline (MPa)

P_{bh} bottom hole pressure (kPa)

P_{cutoff} pressure at which compression switches to pumping (MPa)

$P_{initial}$ initial pressure of CO_2 directly from capture system (MPa)

P_{final} final pressure of CO_2 for pipeline transport (MPa)

P_h hydraulic power (W)

$P_{o,i}$ pressure at *i*-th gridblock containing the well (kPa)

P_{wf} wellbore flowing pressure (psi)

P_{wi} bottomhole injection pressure (psi)

$q_{co2,r}$ injection rate (bbl/d)

Q_j flowrate of Phase *j* (*j* = *g*,*w*) at reservoir conditions (m^3/day)

$q_{w,r}$ brine production rate (bbl/d)

r_{BL} radius of the Buckley Leveret zone (m)

r_{dry} radius of the dry zone (m)

r_w wellbore radius (ft or m)

s skin factor (dimensionless)

S_{wD} dimensionless water saturation

S_w water saturation

S_{wr} residual water saturation

S_{gr} residual gas saturation

T_{in} CO_2 temperature at the compressor inlet (^oC)

$\mathcal{T}$ formation transmissibility (mD.ft)

Trans fault transmissibility (dimensionless)

V_{pipe} CO_2 velocity in injection tubing (m/s)

Wfrac well fraction

$WI_{j,l}$ well injectivity index for Phase *j* (*j*=*g*,*w*) to Layer l

W_p pumping power requirement (kW)

$W_{s,I}$ compression power requirement for each individual stage (kW)

X saturated brine fraction of produced brine

Z_s average CO_2 compressibility for each individual stage

ε pipeline roughness factor (ft)

α miscellaneous escalation cost factor

β right-of-way escalation cost factor

γ material escalation cost factor

λ escalation cost factor

λ_T total mobility of fluid in the well block

μ viscosity (Pa·s)

μ_{co2} viscosity of CO_2 (cP)

μ_w viscosity of water (cP)

η_{is} isentropic efficiency of compressor (dimensionless)

ρ density (kg/ m^3)

Re Reynold's number (dimensionless)

TABLE OF CONTENTS

Page

Page

Page

LIST OF FIGURES

Page

Page

Page

Page

Page

LIST OF TABLES

Page

CHAPTER I

INTRODUCTION

[1]Carbon sequestration, also known as carbon storage, is a process of storing CO_2 that would otherwise be emitted to the atmosphere. Carbon storage is a potential way to enable electricity generation from combustion or conversion of fossil fuels without continuing atmospheric CO_2 emissions. When compared with other storage options, deep saline aquifers are more abundant and have enormous pore volumes, and therefore are considered in this study. This chapter will start with an overview of carbon sequestration. Next will be an explanation of the problem and objective of this research. Finally, there is a summary of the dissertation.

1.1 Overview

Since the industrial revolution, the increase in atmospheric carbon dioxide (CO_2) concentrations has long been linked with human activities, and has been claimed by some scientists as the main gas contributing to the greenhouse gas (GHG) effect and global climate change. Brook (2005) said that the current concentration of atmospheric CO_2 (380 parts per million by volume) is the highest it has been in 650,000 years and is expected to keep increasing if nothing mitigates it. Current atmospheric CO_2 concentrations are 27% higher than the highest recorded level in pre-industrial times and are projected to increase at 0.4% per year. This situation suggests that there is need to find effective methods of reducing CO_2 emission.

According to the Intergovernmental Panel on Climate Change (IPCC) (2005), one of the technological options for reducing anthropogenic CO_2 emissions to the atmosphere and therefore mitigating global climate change is capturing and storing CO_2 chemically or physically. Underground carbon storage is the transportation of CO_2 from point sources, through pipelines or other suitable transport medium and injection into a deep subsurface geological formation for long-term storage. Carbon storage is a possible

---

This dissertation follows the style of *SPE Reservoir Evaluation and Engineering*.

strategy to keep burning fossil fuels without continuing to increase the CO_2 concentration in the atmosphere.

The types of formations in which CO_2 can be stored are depleted oil and natural gas reservoirs, deep unmineable coal seams, and deep saline aquifers (Ehlig-Economides and Economides 2009; Ghomian et al., 2008; Juanes et al., 2006; National Energy Technology Laboratory 2007; Pruess et al., 2003). To date, NETL (2010) through its regional partners have documented the location of more than 143 billion tonnes of sequestration potential in matured oil and natural gas reservoirs, 60 to 117 billion tonnes in unmineable coal seams, and 1,653 to 20,213 billion tonnes in deep saline formations. Calculations done by NETL (2010) indicate that at current CO_2 emission rates, the storage potential is more than 40 years, 15 years, and 450 years, respectively, for these options.

When the option is available, it will make sense to use depleted oil and natural gas reservoirs because they have held oil and gas in the reservoir for millions of years, and therefore have good seals (IEAGHG 2005). Also, they have a wealth of data to be used for planning and managing the CO_2 storage effort that must have been acquired for the field development.

Out of the above mentioned storage formations, deep saline formations offer considerably more potential pore volume, and are typically located nearer to CO_2 point emission sources than are enhanced oil recovery (EOR) operations (Folger 2007). The storage potential of deep saline formations dwarfs that of matured oil and natural gas fields or unmineable coal seams. For this reason, this dissertation will focus on injecting CO_2 in deep saline formations.

In the past 20 years, there have been several carbon storage projects. As of today, there exist only four major projects in the entire world to sequester large volumes of anthropogenic carbon dioxide: Weyburn operation in Canada, Sleipner west and Snohvit project in Norway, and In Salah CO_2 injection in Algeria. The Weyburn project, although different from the others as it is an EOR operation, started injecting CO_2 in late 2000 with an injection rate of 1.8 million tonnes per year and a total estimate of 20 million tonnes over an area of 180 square km (Protti 2005). The In Salah project initiated CO_2 injection in August 2004 at a rate of 1.2 million tonnes per year and a total estimate of 17 million

tonnes (Baroni et al., 2011) over an area of 23,000 square km. A horseshoe-shaped uplift pattern around one of the CO_2 injectors in the In Salah project has been a subject of interest. Davis (2011) used detailed interferometric synthetic aperture radar (InSAR) to measure subsurface deformation and his analysis indicates that a portion above the subsurface is affected by deformation. After further analysis with a seismic survey, he concludes that a strain source, likely either CO_2 or displaced aquifer brine, caused formation movement within the layer overlying the intended storage zone between April 2005 to August 2007. The Sleipner west project initiated CO_2 injection in October 1996 at a rate of 0.9 million tonnes over an area of 26,000 square km per year and a estimated total of 20 million tonnes had been injected by the year 2011 (Eiken et al., 2011).

1.2 Problem and Objectives

A typical 500-MW coal-fired power plant emits about 3 million tonnes of CO_2 per year or about 8200 tonnes per day. Therefore, although they are a start, none of the projects in progress today demonstrates the scale of interest. Most simulation studies of CO_2 injection in saline formations have been done on a small scale assuming a modest injection rate over a limited area (Kumar et al., 2005; Pruess et al., 2003). Only a few have been done on a regional scale (Ghomian et al., 2008; Yang 2008).

The objectives of this study are two-fold: 1) to consider a conceptual approach to increase the storage efficiency of CO_2 injection in saline formations, and 2) to investigate what an actual CO_2 storage project might entail using actual field data for the Woodbine aquifer in East Texas.

In a saline aquifer, bulk injection is the most commonly proposed method for CO_2 injection. Bulk injection causes substantial pressure buildup and limits the amount of CO_2 that can be stored in a given aquifer volume (Ehlig-Economides and Economides 2009; Nunez and Hovorka 2012). To avoid breaching the aquifer seal, CO_2 injection must not pressurize the aquifer above the formation fracture pressure. To increase the amount of CO_2 that can be stored in a given aquifer volume without pressurizing the aquifer, brine is produced at the same volume as the injected CO_2. Then, either the produced brine is disposed as any produced oil field water or desalinated. In the latter case, the saturated brine from the desalination is re-injected back into the same aquifer. The conceptual

study in Chapter III compares bulk injection to the CO_2-brine displacement approaches using global Woodbine aquifer properties.

To better understand the potential risk and challenges of injecting such large quantities of CO_2, Chapter IV uses mapped net and gross thickness, porosity, permeability, and salinity data on the Woodbine aquifer to generate a geological model for flow simulations of the same processes used for the conceptual modeling. Although the saline portion of the Woodbine aquifer is quite extensive, an updip freshwater portion is separated from the saline portion by an extensive system of faults that may or may not be hydraulically sealed. Therefore, an important aspect of this research is a sensitivity study to evaluate the implications of the CO_2 storage on the fresh water if the faults are conductive instead of sealed. In particular, is there a possibility of salt water intrusion or even CO_2 flow through the fault system?

1.3 Research Summary

This chapter describes the problem to be solved and the objective of this study, and also provides a brief summary of the motivation of this work. Chapter II presents a literature review on CO_2 injection into deep saline aquifers and an overview of the Woodbine aquifer geology and history. Chapter III describes three aquifer management strategies studied using four CO_2 injection well patterns. The storage efficiency for each CO_2 injection well pattern is calculated using average aquifer properties.

Chapter IV focuses on the geologic modeling of the Woodbine aquifer to enable a full-field simulation study. The first part of the chapter shows the structural and petrophysical properties of the Woodbine aquifer in contour maps and describes how the maps were used to create a 3D geologic model. In the second part, both bulk CO_2 injection and CO_2 brine displacement are simulated to refine the estimates for the storage capacity from the conceptual models. Finally, additional aspects are evaluated including the potential for saltwater or CO_2 intrusion into the fresh water portion of the aquifer, and possible geochemical reactions from the CO_2 and potential impurities from the CO_2 capture.

Chapter V considers the surface CO_2 transport and estimates what percentage of power plant capacity is needed to inject CO_2 in the Woodbine aquifer using the

management strategies described. The potential impact of such a project on the East Texas region is highlighted including the potential for earthquakes associated with the CO_2 injection. Chapter VI gives conclusions of the dissertation and provides recommendations for future work.

CHAPTER II

CARBON SEQUESTRATION IN SALINE FORMATIONS

Chapter I explained why the focus of this research is carbon sequestration in saline formations. An important goal for a carbon sequestration project should be to estimate how much CO_2 can be injected into the aquifer at what rate and for how long, or alternatively to estimate the aquifer volume sufficient to store CO_2 at a given injection rate and project duration. For this purpose, CO_2 storage efficiency is defined as the ratio between the volumes of CO_2 injected into an aquifer to the pore volume of the aquifer available. A high storage efficiency indicates that a formation requires a smaller area to store the same volume of CO_2 as a formation with a low storage efficiency. This chapter will begin by reviewing issues related to storage in saline aquifers. Next, it will make clear the reason for choosing the Woodbine aquifer as a case study and finally, the history, regional geology, and stratigraphy of the Woodbine aquifer will be reviewed.

2.1 Issues Related to Storage in Saline Aquifer

A 500-MW coal-fired power plant produces about 3 million tonnes of CO_2 per year (Ehlig-Economides and Economides 2009), or about 8200 tonnes per day. At aquifer pressure and temperature, the volume this represents depends on the depth of the aquifer. Typically, aquifers considered as good candidates for CO_2 storage will have sufficient depth to require supercritical CO_2 injection. Also, the supercritical state is better for pipeline transport of the CO_2. The most common method for carbon sequestration is by bulk injection in which CO_2 is continuously injected into a formation without any fluid being produced. When CO_2 is injected into a formation, it displaces the resident formation fluid and partly fills the pore spaces vacated by those fluids. In the case of a saline aquifer, the CO_2 displaces brine. The continuous injection of CO_2 into an aquifer will cause the pressure near the well to increase rapidly until a point where CO_2 injection must cease to avoid fracturing the formation. Therefore, for most aquifers, multiple injection wells will be required to inject CO_2 at a constant rate.

The study by Ehlig-Economides and Economides (2009) estimated storage efficiency for bulk injection to be less than 1% and pointed out that a large storage area would be needed to avoid aquifer pressurization. Akinnikawe et al. (2010) proposed that to minimize the risks of aquifer pressurization and increase storage efficiency, the same volume of CO_2 injected be produced as brine from the aquifer. However, this now poses the problem of how to manage the produced brine.

These issues will be addressed in Chapter IV.

2.1.1 Trapping mechanisms and storage efficiency

Several authors have performed studies to understand and quantify the most important storage mechanism, estimate storage efficiency, and identify which transport mechanism dominates during CO_2 injection.

Pruess et al. (2003) estimated the capacity of saline aquifers to store injected CO_2, either in the free gas phase, dissolved in the aqueous phase, or bound to solid minerals. They used volumetric averages, frontal displacement theory, and numerical simulation to estimate storage capacity factors. They assumed the aquifer to be infinite-acting and areally homogeneous, and neglected inertial and nonisothermal effects. The study found that the liquid phase capacity factor depends weakly on temperature and pressure but varies with salinity. Also, the accumulation of carbonates in the rock matrix, and induced rock mineral alteration caused by the presence of dissolved CO_2, leads to a considerable decrease in porosity. The authors conclude that for typical conditions expected in aquifer disposal of CO_2, the total amount of CO_2 that may be stored in gas, liquid, and solid phases is on the order of 30 kg/m^3 aquifer pore volume. At a representative density of 770 kg/m^3, this corresponds to a storage efficiency of nearly 4%, much higher than that estimated by Ehlig-Economides and Economides (2009).

Van der Meer (1995) states that the storage efficiency of an aquifer is directly related to the CO_2-water displacement process. The very optimistic CO_2 storage efficiency estimated in a previous study by the author was only 2% assuming a closed aquifer volume. In this study, a sensitivity analysis was performed on permeability, injection rates, and angle dip using a 2D simulator and assuming both closed and infinite aquifer volume. The storage efficiency is estimated using a "CO_2 bubble type concept"

and found to be between 1 to 6% depending on the vertical transmissibility of the storage reservoir.

Kumar et al. (2005) did a study to understand and quantify the most important storage mechanism during CO_2 injection into a heterogeneous, infinite-acting aquifer. The study concluded that the well completion strategy impacts CO_2 migration after injection ends; in particular, there is a reduction in mobile gas if CO_2 is injected at the bottom of the aquifer.

Taku Ide et al. (2007) performed simulations of CO_2 injection to investigate the interplay of viscous forces, gravity forces, and capillary trapping of CO_2. The reservoir model assumes a constant-pressure boundary. Their result shows that in a given aquifer, the amount of trapping can be maximized by injecting CO_2 at the lowest feasible values of gravity number (N_{gv}) and, the time scale for completion of capillary pressure entrapment is longer for low N_{gv}. Gravity number is a dimensionless number that relates the magnitude of the gravity force to the viscous force, which is defined as

$$N_{gv} = \frac{k_v L \Delta\rho g}{Hu\mu_{brine}} \tag{2.1}$$

where k_v is the vertical permeability, L the aquifer length, $\Delta\rho$ the density difference, g the acceleration due to gravity, H the aquifer height, u the total average Darcy flow velocity, and μ_{brine} is the viscosity of the brine. Large N_{gv} numbers indicates that the gravity force dominates.

The study also shows that capillary pressure effects and aquifer inclination increased the amount of CO_2 trapped.

Ukaegbu et al. (2009) performed sensitivity studies on the injection of CO_2 into a heterogeneous saline aquifer. The study assumed a closed aquifer system and experienced a sharp increase in pressure after CO_2 injection, consistent with the results of Ehlig-Economides and Economides. The study showed that advection is the dominant transport mechanism during the injection period. Diffusion of CO_2 in the aqueous phase significantly enhances solubility of CO_2 in brine by about 28% in 20 years when case modeled with hysteresis is compared with case modeled with hysteresis and diffusion.

Laboratory experiments using core data are sometimes used to study processes that occur during CO_2 injection, such as geochemical reactions or brine displacement

efficiency. Gunter et al. (1997) performed experiments using samples from glauconitic sandstone drill core to study geochemical reactions that might occur during CO_2 injection in the glauconitic sandstone reservoir in the Alberta sedimentary basin. Their experiment shows that little reaction occurred for one month and the reactions that occurred were because of fast-reacting carbonate minerals. The experiments were validated by a geochemical model. These CO_2-trapping reactions were found to take 100s of years if the model is extended to the field.

Kuo et al. (2010) used numerical simulation to interpret and extrapolate the results of core-scale laboratory experiments, which is used to determine the influences of sub-core scale heterogeneity, gravity, and flow rate on brine displacement efficiency. Simulation result shows that brine displacement efficiency is a strong function of capillary number and gravity number. The capillary number (Ca) is a dimensionless number that relates the magnitude of the capillary force to the viscous force and is defined as

$$Ca = \frac{u_t \mu_w}{\sigma} \tag{2.2}$$

where u_t is the total average Darcy flow velocity, μ_w is the viscosity of the brine, and σ is the interfacial tension between CO_2 and brine. Efficiency of brine displacements during vertical displacement falls into three regimes: viscous-dominated regime, capillary-force-dominated regime, and buoyancy-force dominated regime. The average saturation of the core is nearly independent of flowrate in the viscous-dominated regime. Saturation gradients are large and exist along the horizontal and vertical direction in the gravity-dominated regime and the displacement efficiency is highly sensitive to the flowrate. Flowrate dependency increases partly because of the presence of heterogeneity but largely because of buoyancy effects. Brine displacement efficiency drops by about 80% when the capillary number is below 10^{-7} and gravity number is 2. To improve brine displacement efficiency, a sequestration project should aim for a low N_{gv} and a high Ca.

Impacts of trapping to this study are addressed in Chapters III and IV.

2.1.2 Injection schemes

Several studies have been performed to investigate the impact of injection schemes and well placement on CO_2 injectivity. Delshad et al. (2010) conducted a reservoir simulation study to access the impact of various injection schemes on amount of CO_2 sequestered and the extent of vertical migration. In their study they assumed closed and partially open aquifers, homogeneous and heterogeneous permeability fields, and bulk and simultaneous CO_2 and brine injection. The study concludes that well placement, well completion, and injection rates should be made specific to each aquifer. Aquifer permeability is the key to identifying optimum well completion and injection schemes. Carbon dioxide injectivity reduced significantly when simultaneous CO_2 and water are injected in a ratio of 95 to 5 respectively.

Ghaderi et al. (2009) performed numerical simulations to study the injection of large volume of CO_2 (20 million tonnes per year for 50 years) in an aquifer. A sensitivity analysis of plume area and CO_2 storage capacity is presented within the range of aquifer parameters: thickness, permeability, rock compressibility, and different injection arrangements. Their reservoir model assumes an infinite-acting reservoir. Among other things, the authors conclude that injecting large CO_2 volumes into a reservoir would require a multiple injection well design; however, increasing the number of injection wells has diminishing returns. Results from the study show that permeability and net thickness of the formation directly impact injectivity. However, rock compressibility manifests its effect when a larger number of injectors are used. Also, applying stimulation techniques, such as hydraulic fracturing, can improve injectivity.

2.1.3 Mitigating aquifer pressurization

Aquifer pressurization is a concern during CO_2 injection in closed systems. Several authors have avoided this issue by assuming a constant-pressure boundary to model the aquifer. Ehlig-Economides and Economides (2009) pointed out that the reservoir pressure will increase if large quantities of CO_2 are injected at constant rate. Yang (2008) performed numerical simulations of CO_2 injection in the Browse Basin,

offshore Western Australia using a closed system. The study reveals that brine production is required to relieve rapid aquifer pressure increase and to increase storage efficiency.

According to Wilkinson and Szafranski (2009), having a good understanding of the regional pressure gradients is essential to predict long-term storage pressures and the potential for migration of injected fluids. In their study, they proposed the removal of brine to maintain pressure below formation fracturing pressure. The study suggests that the brine withdrawal point be placed below the CO_2 injection point. This would down-cone the buoyant CO_2 so that it would decrease the rate of lateral migration of the CO_2. Furthermore, the withdrawn brine could be re-injected into an overlying porous reservoir (if present) so that it could quench any buoyant CO_2 that escapes through the caprock. This operational option will increase the efficiency of pore space utilization.

Qi et al. (2009) proposed a carbon storage strategy where CO_2 and brine are injected into one corner of the aquifer while brine is produced from the other corner to prevent pressure increases and act as a source of brine injection. The reservoir volume of brine produced is equal to the reservoir volume of fluids injected. Their simulation results indicate that a combination of brine and CO_2 injection can lead to the trapping of a vast amount of CO_2 after a relatively short period of chase brine injection and with a storage efficiency that is higher than CO_2 injection alone. For the bulk injection case, the storage efficiency was 3% whereas that for the chase-brine case was 9%. The study finds that the minimum volume of chase brine required to trap most of the CO_2 occurs at a gas fractional flow of 0.85.

Anchliya and Ehlig-Economides (2009) proposed an engineered system to avoid aquifer pressurization and accelerate CO_2 dissolution and trapping. A horizontal brine injection well is positioned well above and parallel to a horizontal CO_2 injection well with horizontal brine production wells drilled parallel to the CO_2 injection well at the specified lateral spacing.

A volume balance is kept between injected and produced fluids. Simulation results showed that CO_2 accumulation at the top layer is prevented and 90% of the CO_2 is permanently dissolved or trapped after 50 years, including 30 years of injection.

2.1.4 Effects of impurities in CO_2-rich stream

The exit gas stream from a power plant contains CO_2 and other waste gases. For a coal-fired power plant, the amount of CO_2 in the flue gas stream is about 11–14%. Xu et al. (2003) reported the separation of CO_2 from flue gas of a gas/coal-fired power plant using a molecular solvent. According to their report, the composition of the flue gas from the gas-fired power plant is shown in Table 2.1.

Table 2.1—Exit flue gas composition from gas-fired and coal-fired power plants

Component	Gas-fired plant	Coal-fired plant
CO_2	7.4–7.7%	12.5–12.8%
H_2O	14.6%	6.2%
O_2	4.45%	4.4%
CO	200–300 ppm	50 ppm
NO_x	60–70 ppm	420 ppm
SO_2	N/A	420 ppm
N_2	73–74%	76–77%

MIT (2007) performed an interdisciplinary study that designed and compared various electric power generating technologies based on the Carnegie Mellon Integrated Environmental Control Model (IECM), which is specific to coal-based power generation. The designs were made to achieve emission levels lower than what was currently available and assumes the power plants burn Illinois #6 bituminous coal with a high heating value of 25,350 kJ/kg. Some of the technologies considered had electrostatic precipitator (ESP) and flue gas desulfurizer (FGD) to remove particulates and sulfur or its oxides. The exit gas streams for the technologies considered are listed in Table 2.2.

Table 2.2—Exit gas composition of different designed coal-based power generation technologies (vol %)

Component	Subcritical 500-MWe Pulverized Coal Unit	Ultra-supercritical 500-MWe Pulverized Coal unit	500-MWe Circulating Fluid-Bed unit burning Lignite	500-MWe IGCC unit
N_2	66.6	66.6	68.9	66.6
H_2O	16.7	16.7	10.2	16.7
CO_2	11	11	13.7	11
O_2	4.9	4.9	6.4	4.9
Ar	0.8	0.8	0.8	0.8
SO_2	22 ppm	22 ppm	58 ppm	22 ppm
NO_x	38 ppm	38 ppm	140 ppm	38 ppm
Hg	<1 ppb	<1 ppb	~22 ppb	<1 ppb

Carbon dioxide will be separated from other flue gases before it is pipelined for storage. Several methods are available for CO_2 capture from flue gases. The preferred option for post-combustion CO_2 capture is through adsorption processes based on chemical solvents (Intergovernmental Panel on Climate Change 2005). Solvents such as monoethanolamine (MEA) offer higher capture efficiency and selectivity at a lower energy and cost when compared to other existing post combustion capture processes. In practice, typical CO_2 recoveries are between 80 and 95%. The exact recovery is an economic trade off involving higher energy requirements and higher costs (Intergovernmental Panel on Climate Change 2005).

Inevitably, there will be some impurities in the rich CO_2 stream after it has been separated. Public information about CO_2 pipeline quality specification is scarce. To date most existing compositional specification appear only within private contracts between buyers and sellers (United States Department of Energy 2010). The quality specification for Kinder Morgan CO_2 pipeline is CO_2 ($\geq$ 95 vol%), H_2O ($\leq$ 30 lb/MMscf), H_2S ($\leq$ 20

ppmw), total sulfur (≤ 35 ppmw), N_2 (≤ 4 vol%), hydrocarbons (≤ 5 vol%), O_2 (≤ 10 ppmw), other (glycol: ≤ 0.3 gal/MMscf), temperature (≤ 120°F).

The gas composition of current EOR CO_2 pipelines are shown in Table 2.3 (Jung and Nicot 2010). These are mostly gas composition from naturally occurring CO_2 reservoirs, except for the Weyburn EOR project which is from a gasification unit.

Table 2.3—Gas composition in current EOR CO_2 pipelines (unit: vol %)

Component	Canyon Reef SACROC	Weyburn EOR	Bravo Dome	Cortez Pipeline	Sheep Mountain	Central Basin
CO_2	85–98	96.0	99.7	95	96.8–97.4	98.5
H_2S	<200 ppm	0.9	–	0.002	–	<20 ppm
CH_4	2–15	0.7	–	1–5	1.7	0.2
C2+	Trace	2.3	–	Trace	0.3–0.6	–
CO	–	0.1	–	–	–	–
N_2	–	<300 ppm	0.3	4	0.6–0.9	1.3
O_2	–	<50 ppm	–	–	–	<10 ppm
H_2O	50 ppm	<20 ppm	–	257 ppm	129 ppm	257 ppm

The exit gas composition data from the MIT report will be used to show the effect of impurities on carbon sequestration in Chapter IV.

Some studies have been performed to see the effects of some of these impurities during pipeline transport and CO_2 injection in saline aquifers. In the absence of moisture, neither CO_2 nor SO_2 will cause corrosion. Yoon-Seok et al. (2010) performed an experimental study to evaluate the corrosion property of carbon steel under CO_2-saturated water phase and water-saturated CO_2 phase with impurities O_2 and SO_2 at 80 bar CO_2 and 50ºC. Their results show that after 120 h, the corrosion rate of carbon steel in CO_2-saturated water phase was very high (10.6 mm/y) and increased to 14.1 mm/y with the addition of O_2 to the system. This is because O_2 inhibits formation of a protective $FeCO_3$ layer and forms another non-protective iron oxide. Carbon steel corrosion also occurs in

the presence of a water-saturated CO_2 phase under supercritical conditions when no free water is present, and addition of O_2 slightly increases the corrosion rate. However, in this case, the corrosion rate does not increase with increasing O_2 concentration but reaches a maximum of 1 mm/yr with 4% O_2. The addition of 0.8 bar SO_2 (1%) in the gas phase greatly increases the corrosion rate of carbon steel from 0.38 to 5.6 mm/yr. This further increases to more than 7 mm/yr with the addition of both O_2 and SO_2. The corrosion rates of 13Cr steel are very low compared to carbon steel in the CO_2-saturated water environments with O_2, but are similar to carbon steel in the presence of a water-saturated CO_2 phase with O_2 and SO_2.

Brian et al. (2010) used three model scenarios to gain more understanding of the magnitude and time scale of brine acidification for the case of SO_2 co-injection during geologic carbon sequestration in deep saline aquifers. Brine pH changes were predicted for three possible SO_2 reactions: hydrolysis, oxidation, or disproportionation. The model scenarios considered were geochemical model, phase equilibrium model, and a diffusion model accounting for diffusion-limited release of SO_2 from the CO_2 phase. Injection of pure CO_2 formed carbonic acid and caused a brine pH of 4.6 under typical reservoir and alkalinity conditions in a storage formation.

For the phase equilibrium model, co-injection of 1% SO_2 led to a pH close to 1 with SO_2 oxidation or disproportionation and close to 2 with SO_2 hydrolysis. Using diffusion modeling that considers SO_2 diffusion limitations in the supercritical CO_2 phase and uniform SO_2 distribution in a slowly advecting brine phase, SO_2 oxidation led to pH values near 2.5, 400 years after injection. In this scenario, SO_2 hydrolysis led to pH values only slightly less than those due to CO_2 alone. The authors conclude that the extent to which co-injected SO_2 can impact brine acidity is limited by diffusion-limited dissolution from the CO_2 phase, and may also be limited by the availability of oxidants to produce sulfuric acid. These results will be considered in Chapter IV.

2.2 Case Study—Woodbine Aquifer

The Woodbine aquifer is located in East Texas and has been used historically as a groundwater source. Because it contains oil and gas in other areas, the Woodbine

formation has been extensively studied in the study area. It was considered by FutureGen (2006) as a potential reservoir for carbon sequestration.

Regions where the Woodbine aquifer is used as a groundwater resource include the northwestern part of the aquifer near where it outcrops and in subsurface regions with artesian conditions at depths where aquifer sediments are filtered because of low permeability clay and carbonate-rich units confine the sand-rich aquifer (R.W. Harden & Associates Inc. 2004). Excessive development of the aquifer begun in the late 1800's led to regional artesian pressure decline, and many wells ceased flowing by early 1900's (R.W. Harden & Associates Inc. 2004). The Woodbine has a complex structure with two major fault systems: the Mexia-Talco faults system and the Elkhart-Mt. Enterprise fault zones. It has several turtle structure anticlines, salt anticlines, and salt diapirs. The Woodbine uncomformably overlies the Lower Cretaceous Washita group and its caprock is the Eagle Ford shale.

The following sections address the depositional history of the Woodbine aquifer, regional geology, and stratigraphy. The area used for this study is impacted considerably by these geologic factors.

2.2.1 Depositional history of Woodbine aquifer

The Cretaceous Woodbine formation is bounded by the outcrop on the west and north, the Sabine uplift in the east and by a line from Temple to College Station in the south (Oliver. 1971). It underlies an approximate area of 96,000 km^2 (37,000 mi^2) that encompasses 45 counties. To the north, it was bounded by the Ouachita system, which was a source of sediment for Woodbine depositional systems. The Woodbine has been one of the most productive oil and gas targets in the East Texas Basin. In October 1920, the first Woodbine discovery was made at Mexia and massive exploration followed since then.

The Woodbine formation is a clastic progradational wedge deposited into the East Texas Basin, one of the salt basins formed during the early Mesozoic. The thickest of the Woodbine sediments were deposited in fluvial and deltaic settings. The sorting of these sediments during the final phases of Woodbine deposition formed excellent-quality reservoirs. The Sabine Arch uplift at the eastern edge of the basin truncates the

Woodbine; the Austin Chalk unconformably covers the uplift. The Cretaceous Woodbine is overlain by a Tertiary sequence of mainly clastics and dips gently towards the Gulf. Salt pillows and diapirs formed during the Cretaceous and these diapirs have risen more slowly during the Cenozoic (Seni and Jackson 1984). The Woodbine sandstones within the East Texas Basin have been isolated from recharge zones in the Woodbine outcrops on the northwest by the Faults of the Mexia-Talco and in the east by Elkhart-Mt. Enterprise fault zones (Kreitler 1981). Figure 2.1 shows the location map of the East Texas field characterized by Ambrose et al., 2009.

2.2.2 Structural geology

The Woodbine was deposited in an era in which there were several structural activities occurring in the East Texas Basin. These activities include growth-faulting along the Mexia-Talco zone, faulting in the Mt. Enterprise fault zone in the South-Central portion of the Basin, and growth of numerous salt domes throughout the central basin area (Oliver. 1971). A map of the salt diapirs and salt pillows in the East Texas Basin is shown in Figure 2.2.

Throughout Cretaceous and early Tertiary basin sedimentation, the mobilization of the Middle Jurassic Louann salt, most commonly as diapirs caused a structural modification of more than 13,000 ft (>3960 m) of Mesozoic and Tertiary strata filled in the deepest part of the basin (Seni and Jackson 1984; Wood and Guevara 1981).

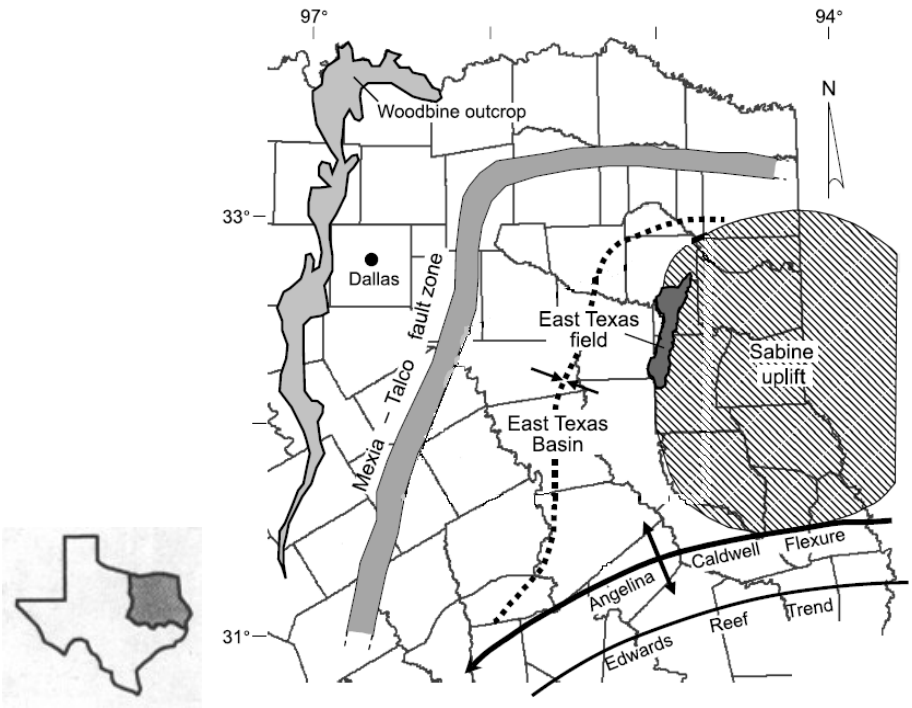

Figure 2.1—Location map of the East Texas field (modified from Ambrose et al., 2009).

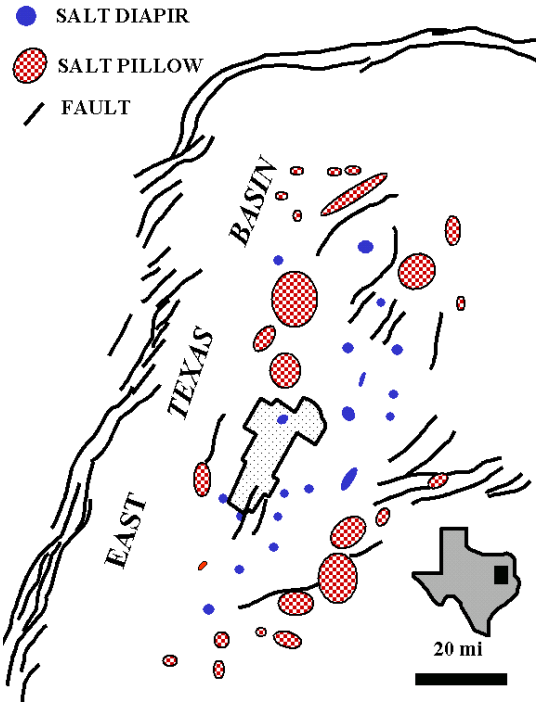

Figure 2.2—Salt diapirs and salt pillows, East Texas Basin (adapted from Maione, 2000).

If the area is already close to failure, fluid injection at relatively high pressures can induce adjacent seismicity, (Nicholson 1992). The best-known earthquake to have been triggered by fluid injection is a magnitude 5.5 earthquake that occurred near Denver, Colorado in 1967 (Healy et al., 1970; Nicholson 1992). This was a waste disposal well in which fluid was being injected into relatively impermeable crystalline basement rock (Nicholson 1992). On 31 October 2008, nine earthquakes with magnitudes between 2.5 and 3.0 occurred in Dallas-Fort Worth. These earthquakes are believed to have been triggered by deep saltwater disposal wells in the area (Frohlich et al., 2010). Another example of induced seismicity is that of the Geysers Geothermal Area in Northern California. Studies of the Geysers Geothermal Field seismicity have concluded that deep-well injection in the field produces micro-seismic events of low magnitude. The largest recorded event so far was a magnitude 4.6 earthquake in the 1980s (Majer et al., 2007)

Injection wells should be placed away from faults to avoid induced seismicity. Fault reactivation or failure can be analyzed based on in-situ stress and locally high pore pressure, which can occur if gas accumulation in a reservoir is adjacent to a long dormant normal fault (Wiprut and Zoback 2000). A geotechnical fault reactivates or opens whenever the shear stress reaches the Mohr-Coulomb failure criterion or the normal stress decreases to zero (Mendes et al., 2010).

To perform a rigorous stress fault analysis, rock properties regarding deformation and strength are required. The following parameters in Table 2.4 along with data their sources are needed for full definition of stress states (Chiaramonte 2008). Lucier et al. (2011) has indicated that inducing earthquakes is a major risk for CO_2 sequestration.

Table 2.4—Parameters and data needed to perform stress fault analysis

Parameter	Data Source
Vertical stress	Density logs
Minimum horizontal stress	Leak-off tests, minifrac
Maximum horizontal stress	Modeling wellbore failures
Stress orientation	Orientation of wellbore failures
Pore pressure	Sonic logs, Repeat formation Tester (RFT)
Rock strength	Triaxial shear tests, modeling well failure
Faults and fractures	Seismic, wellbore imaging

2.2.3 Stratigraphy

The Woodbine occurs between the older, limestone-dominated Washita Group and the younger, areally extensive Eagle Ford Group (lower Turonian), the principal source rock for East Texas field hydrocarbons (Ambrose et al., 2009; Dzou et al., 2000). The uppermost Washita section comprises the 170- to 200-ft-thick Buda Limestone, a deeper shelf limestone, and the overlying thick (60–75 ft) Maness Shale. The Woodbine Group reaches a maximum thickness of approximately 890 ft in the basin and thins gradually towards the Sabine uplift, where it is as much as 250 ft thick at the west (downdip) edge of the East Texas field (Ambrose et al., 2009). The stratigraphic column of the East Texas field is shown in Figure 3.

The Woodbine formation consists of three principal depositional systems, a fluvial system, a highly destructive delta system, and a shelf-strand plain system (Oliver. 1971). The Woodbine can be subdivided into two members: the Dexter member and the Lewisville member. The Dexter member (lower Woodbine) dominates in the north and northeast of a line from Dallas to Tyler. The Lewisville member (upper Woodbine) was formed because of continued subsidence of the area previously occupied by the fluvial system and migration towards the east throughout the Woodbine delta (Oliver. 1971).

The fluvial system has a tributary facies and a coarse-grained meander belt facies. These are two facies commonly encountered in Holocene (~10,000 years) fluvial

deposits. The difference in external geometry of the sand bodies and the ratio of channel to overbank deposits is the main distinction between the two (Oliver. 1971).

Developed immediately downslope from the fluvial system is the highly destructive delta system. It is the most significant Woodbine depositional system in terms of areal extent and volume of sediments deposited. There are three distinct component facies of the Woodbine delta system: the progradational channel-mouth bar sands, the coastal barrier sands, and the prodelta-shelf muds seaward of the coastline(Oliver. 1971).

The shelf-strandplain system was formed by the deposition of the Lewisville member (upper Woodbine) along an extensive coastline marginal to active deltas and is considered distinct genetically from facies of the delta system (Oliver. 1971). The two component facies of the system (shelf muds and strandplain sands) are distinguished largely based on gross lithology (Oliver. 1971).

The mineralogy of Woodbine formation is described by Wagner (1987) as fine- to coarse-grained, moderately sorted sandstones with abundant quartz grains with secondary overgrowths, varying amounts of clay, including authigenic chlorite and kaolinite, and minor amounts of feldspar.

ERA	SYSTEM	SERIES	GROUP	FORMATION
CENOZOIC	TERTIARY	EOCENE	CLAIBORNE	YEGUA
				COOK MOUNTAIN
				SPARTA
				WECHES
				QUEEN CITY
				REKLAW
				CARRIZO
			WILCOX	UNDIFFERENTIATED
		PALEOCENE	MIDWAY	UNDIFFERENTIATED
MESOZOIC	CRETACEOUS	UPPER CRETACEOUS	NAVARRO	UPPER NAVARRO CLAY
				UPPER NAVARRO MARL
				NACATOCH SAND
				LOWER NAVARRO
			TAYLOR	PECAN GAP
			AUSTIN	AUSTIN CHALK
			EAGLE FORD	EAGLE FORD SHALE
				SUB CLARKSVILLE
			WOODBINE	LEWISVILLE Mbr.
				DEXTER SAND Mbr.
		LOWER CRETACEOUS	WASHITA	MANESS SHALE
				BUDA LIMESTONE
				GRAYSON SHALE
				GEORGETOWN
			FREDERICKSBURG	KIAMICHI SHALE
				GOODLAND LIMESTONE
			TRINITY	PALUXY
				GLEN ROSE
				TRAVIS PEAK (HOSSTON)
			COTTON VALLEY	SCHULER
				BOSSIER
	JURASSIC	UPPER JURASSIC	LOUARK	GILMER LIMESTONE
				BUCKNER
				SMACKOVER
		MIDDLE JURASSIC	LOUANN	NORPHLET
				LOUANN SALT
		L.Jurassic		WERNER
	Upper Triassic			EAGLE MILLS
PALEOZOIC				OUCHITA

Figure 2.3—Stratigraphic column of the East Texas field.

2.3 Chapter Conclusions

This chapter reviews the potential problems of storing CO_2 in saline aquifers, factors to be considered in a sequestration modeling, and the geology of the Woodbine aquifer.

The most common method for storing CO_2 is bulk injection; however, bulk injection at large rates requires multiple injection wells and causes aquifer pressurization. This issue can be solved by creating a relief for the pore pressure increase. One solution is to produce same volume of brine as CO_2 injected.

In a given reservoir, the ultimate amount of CO_2 that can be stored depends on the storage efficiency, that is, how much volume of CO_2 is stored per reservoir volume available. The storage efficiency can be increased by operating in such a way that the gravity to viscous force ratio, N_{gv}, is minimized.

The components of the sequestered gas will inevitably contain some impurities. These impurities may lower the pH of the formation or cause formation of precipitates that will impair permeability and adversely affect injectivity.

The Woodbine aquifer was one of the final four aquifers considered for the FutureGen project. The Woodbine has good reservoir properties and has been extensively studied.

Chapter III will describe a conceptual model for mitigating aquifer pressurization and increasing storage efficiency using averaged reservoir properties of the Woodbine aquifer. Two new injection strategies will be introduced and the storage efficiencies of the strategies will be compared.

CHAPTER III

CONCEPTUAL MODEL*

In the previous chapters, it was emphasized that bulk injection causes aquifer pressurization and that a way to alleviate the effect of increased pore pressure is to produce a volume of native aquifer fluid equal to the volume of injected fluids.

In this chapter, three approaches to aquifer management are examined. Using properties of the Woodbine aquifer, a bulk-injection case is first considered, as was proposed for FutureGen, and is the most commonly proposed method for CO_2 sequestration. Subsequently, two approaches for CO_2-brine displacement using traditional waterflood injection and production well patterns are considered. The storage efficiency for each pattern is evaluated. The first approach is external disposal of produced brine in the same manner as is done with produced oilfield water. The second approach considers desalinating the produced brine and internal disposal by injecting saturated brine into the same aquifer being used for CO_2 sequestration.

3.1 Aquifer Properties

The Woodbine aquifer, one of the final four evaluated for the FutureGen demonstration project, was selected for this hypothetical study. According to the FutureGen Alliance (2006, 2007), the aquifer has an average temperature of 162^{o}F, the formation pressure is 2348 psi, and it has a pressure gradient of 0.46 psi/ft. The porosity in the aquifer ranges from 20–30% with a mean porosity of 25% whereas the reservoir permeability ranges from 10 to 3000 mD. Figure 3.1 shows a map of the Woodbine aquifer with salinity contours. Also shown are the locations of coal-fired power plants in the vicinity of the aquifer. The map of the aquifer net thickness (Figure 3.2) shows that the thick area of the aquifer is much more limited than the saline area (Bureau of Economic Geology 2010).

The rectangle overlain on Figures 3.1 and 3.2 indicates where the aquifer is both saline and thick and has dimensions 100 km (62.5 mi) by 200 km (125 mi) with average net thickness about 100 m (328 ft). The total dissolved solids

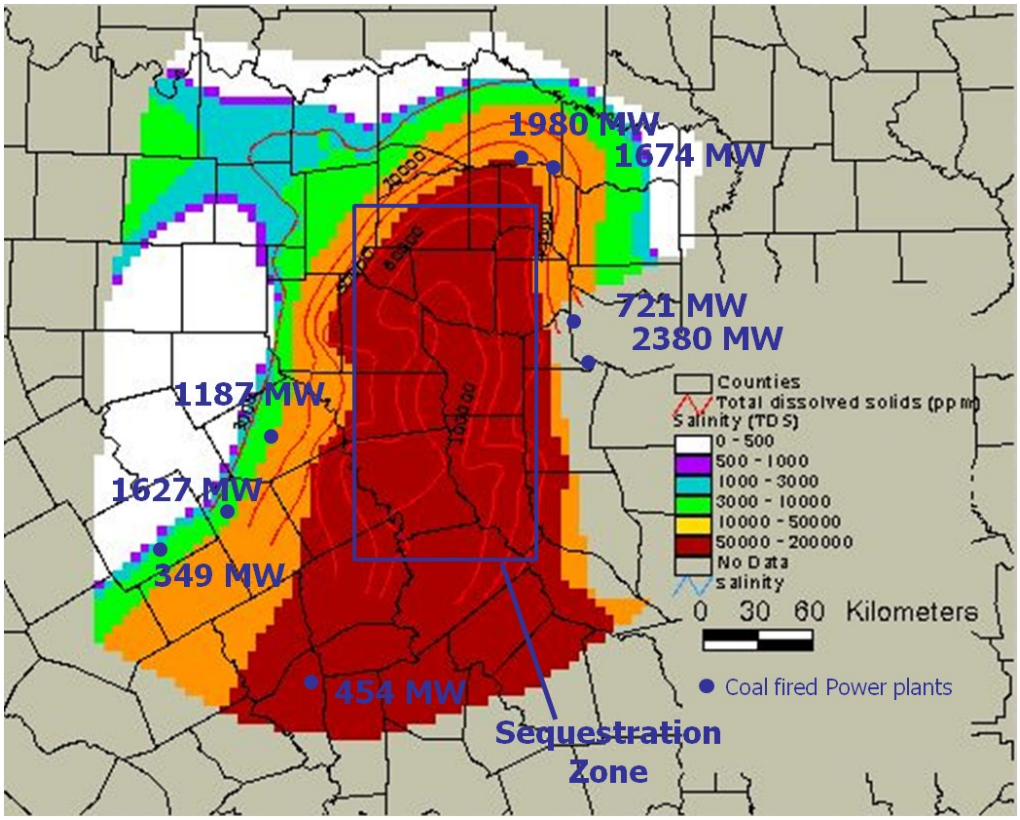

Figure 3.1—Map of the Woodbine aquifer showing salinity contours and locations of coal-fired power plants (adapted from (Bureau of Economic Geology 2010)).

(TDS) concentration of the aquifer brine is about 90,000 ppm in this region. The pore volume of this portion of the aquifer is approximately 4×10^{11} m^3 or 2,520 billion res bbl.

There are eight coal fired power plants located in the vicinity of the Woodbine aquifer with a total generating capacity of 10,372 MW. A 500-MW coal-fired power plant generates about 3 million tonnes of CO_2 per year; therefore the coal-fired power plants in the vicinity of the Woodbine aquifer will generate about 62.2 million tonnes of CO_2 per year. This is equivalent to a surface rate of about 3.2 Bscf CO_2 per day, which at an average reservoir pressure of 21 MPa and temperature of 158ºF is about 1.58 million res bbl/d using a supercritical CO_2 specific gravity (relative to water) of 0.68

This study uses a non-isothermal simulation with a CO_2 injection temperature of 145ºF. Also, the model includes the effect of water vaporization (a.k.a. the "drying out" effect) which occurs when brine is vaporized into the CO_2 phase because of the injection of dry gas is modeled.

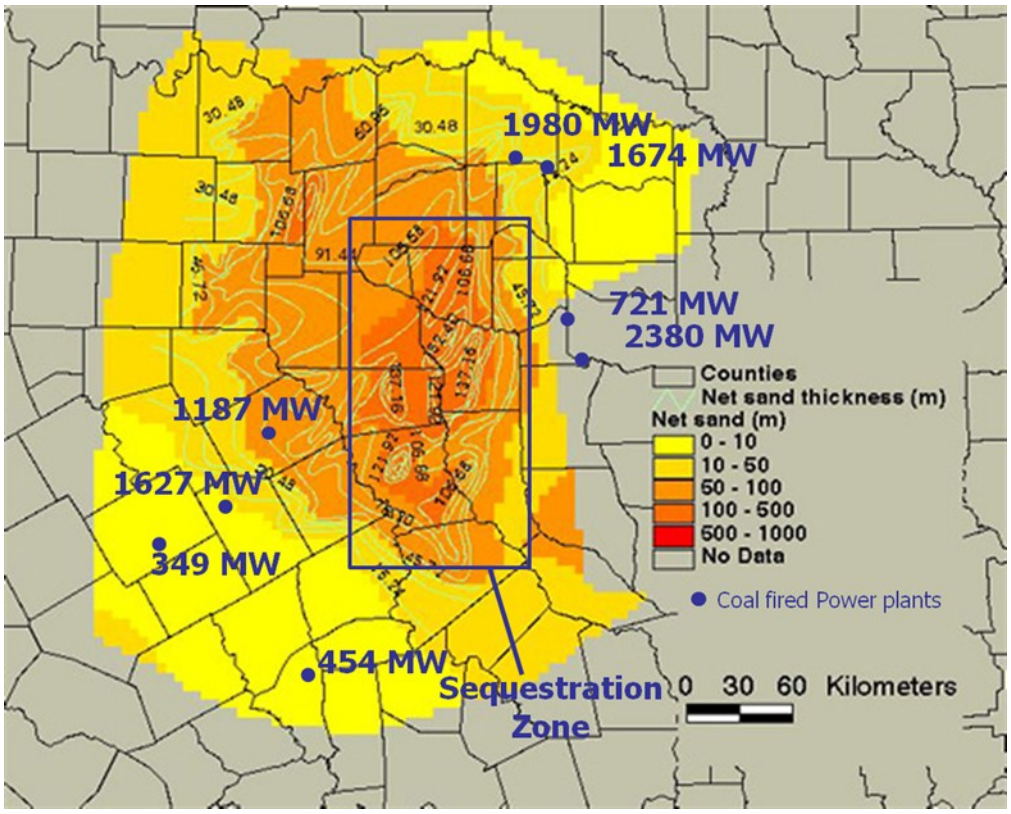

Figure 3.2—Map of the Woodbine aquifer showing net sand thickness contours (adapted from (Bureau of Economic Geology 2010)).

The measured and published relative permeability curves by (Bennion and Bachu 2005) for CO_2-brine systems was used for this study. The second core sample of the Viking formation was particularly used. It has a residual water saturation (S_{wr}) of 0.423, Corey-model parameter for brine of 1.7, Corey-model parameter for CO_2 of 2.8 and the gas relative permeability (K_{rg}) at irreducible brine saturation is 0.2638.

To eliminate the effect of dissolution, brine-saturated CO_2 and CO_2-saturated brine were used to flood the core. Therefore, the laboratory relative permeability does not account for drying because the fluids are saturated. To avoid incorrect pressure gradients in the dry region and consequently wrong estimation of injection rate and cumulative CO_2 injected, the laboratory relative permeability curve has to be corrected by extending

the endpoint of the gas relative permeability (at residual water saturation) to 1 (Kumar 2008) as shown in Figure 3.3.

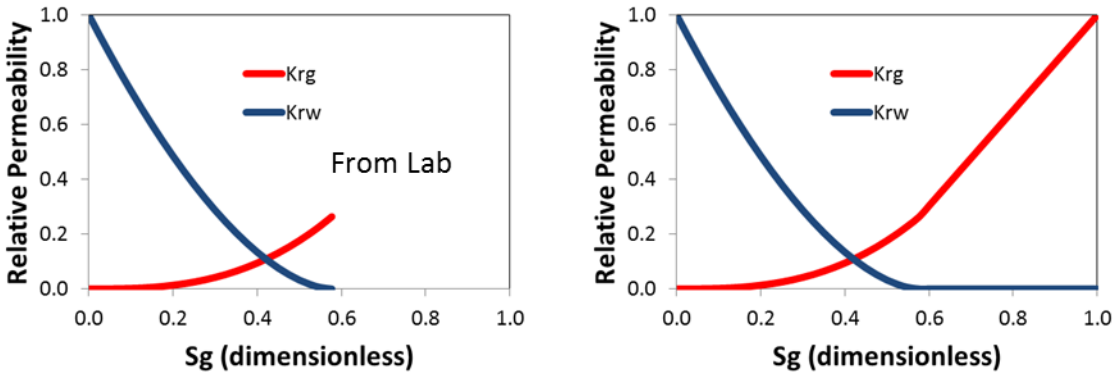

Figure 3.3—Correction of laboratory relative permeability curve to account for drying.

Relative permeability hysteresis is modeled using Land's trapping model with a maximum trapped gas saturation of 0.297. A diffusion coefficient of 2×10^{-5} cm^2/s is used to model the diffusion of CO_2 in brine. Assuming a fracture gradient of 16 kPa/m (0.71 psi/ft), the maximum allowable injection pressure is set at 21,146 kPa (3067 psi), which is 90% of the fracturing pressure at the shallowest depth of 4800 ft. Table 3.1 provides the aquifer and fluid properties used in the simulations.

Table 3.1—Aquifer and fluid properties

Thickness (ft)	528
Formation depth (ft)	4800
Permeability (mD)	600
Porosity	0.155
Rock Compressibility (psi^{-1})	5×10^{-6}
Temperature (°F)	155–162
Salinity (ppm)	90,000
Vertical to horizontal permeability ratio	0.1
Maximum injection pressure (psi)	3067
Minimum brine production pressure (psi)	1200

3.2 Aquifer Management Strategies

Three approaches to aquifer management are highlighted in this study:

- bulk CO_2 injection,
- direct CO_2-brine displacement where CO_2 is injected into the aquifer and the same volume of native brine produced, and
- CO_2-brine displacement with CO_2 and saturated brine injected into the aquifer and the native brine volume produced is equal to the sum of CO_2 and saturated brine volumes injected.

Reservoir voidage balances of injected and produced components are kept at all times in the CO_2-brine displacement strategies. A porosity value of 0.155 was used in the simulation so that the product of porosity and gross thickness (ϕh) was same as the product of the actual mean porosity (0.25) and the net thickness.

The injection patterns considered for the CO_2-displacement cases are (1) a quarter five spot pattern of CO_2 injection and native brine production in a closed boundary, (2) a CO_2 injector and brine producer pair with a large reservoir boundary, and (3) a staggered line drive of two injectors and two producers with a large reservoir boundary. For all simulations, the aquifer outer boundary is closed. For displacement simulations, the minimum brine production pressure is set at 1200 psi, and to achieve this pressure the brine must be artificially lifted (pumped) from the aquifer.

3.2.1 Bulk injection

A 3D homogeneous aquifer with dimensions of 19.4 × 19.4 mi^2 × 528 ft discretized into gridblocks of 50 × 50 × 16 was created using aquifer properties in Table 3.1. The CO_2 injection rate was 156×10^6 SCF/day injected in a vertical well located at i = 25, j = 25 and perforated at k = 14–16. The software used for the simulation is the CMG-GEM compositional simulator, 2011.

The duration of injection was set to 40 years to get as much CO_2 as possible into the aquifer. Figure 3.4 shows the saturation profile of the gas at the time when the injection rate began to decline at 23 yr. The volume of concentrated CO_2 near the well is dwarfed by the aquifer volume required to allow constant CO_2 injection for 23 years. The storage efficiency for the bulk injection case, calculated as the ratio of the cumulative CO_2 injected at constant rate at reservoir conditions (466×10^7 bbl) to the simulated reservoir pore volume, is 0.46%. This is similar to the result gotten from a model by

Ehlig-Economides and Economides (2010) which indicates the area required to support continuous injection at this rate for 30 years would be 635 mi^2, which would be a square area of 25 by 25 mi, and with storage efficiency about 0.51%. With storage efficiency of 0.46%, the volume of CO_2 that can be stored in a closed volume of 2,520 billion res bbl is 11.59 billion res bbl. Bulk injection at a rate of 1.58 million res bbl/d can continue for 7343 days or about 20 years.

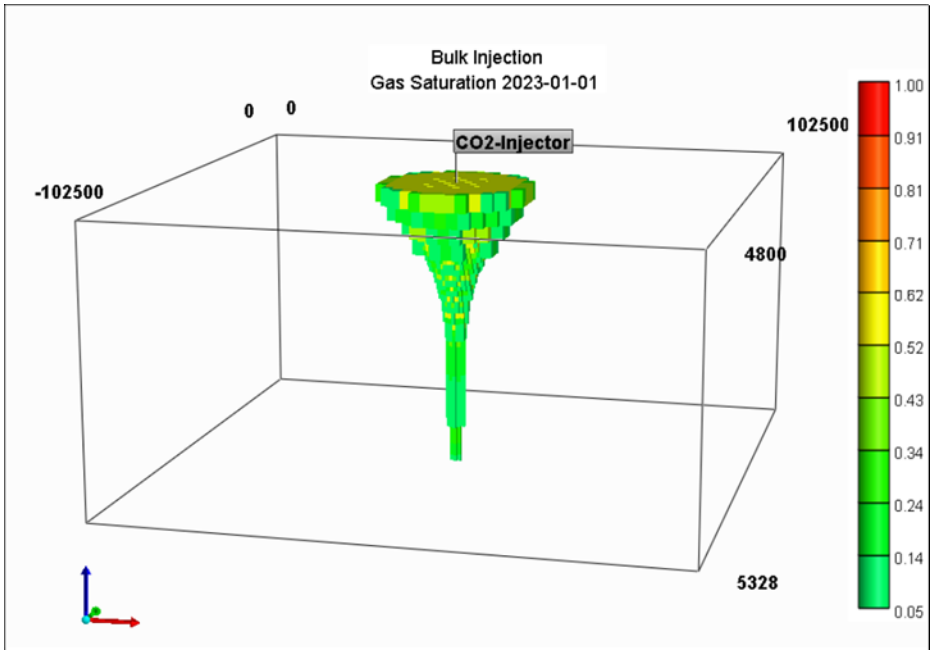

Figure 3.4—Saturation at end of CO2 injection project (bulk injection).

Noting that the saline aquifer is hydraulically communicating with up dip fresh water, some may object to this calculation. The logic would be that the rest of the aquifer would "adsorb" the pressurization resulting from continued CO_2 injection. The problem with this logic is that at the same time bulk CO_2 injection would be occurring, water would be produced for irrigation and other uses from the updip fresh water aquifer at an average rate of the same order of magnitude as what this study considers for CO_2 injection (Texas Commission on Environment Quality 2007; Texas Water Development Board 2007). Noting this aquifer has not had sufficient recharge in recent years (Texas

Water Development Board 2007), the possibility of salt water intrusion or even CO_2 intrusion cannot be ignored.

Furthermore, the proximity of the bulk CO_2 injection area to the fresh water portion of the Woodbine aquifer is daunting. From Figure 3.1, the nearest distance between the CO_2 injection and the saline/fresh interface is about 30 km or less. Considering the 20-year limit on CO_2 injection combined with the proximity of the injection area to the fresh/saline water interface, bulk CO_2 injection does not appear to be a viable option.

The plot of the CO_2 injection rate versus time is shown in Figure 3.5. It can be seen that after about 23 years, the CO_2 injection rate declines rapidly as the aquifer has become pressurized and the bottom-hole pressure has reached the maximum constraint set so that it does not exceed the formation fracture pressure.

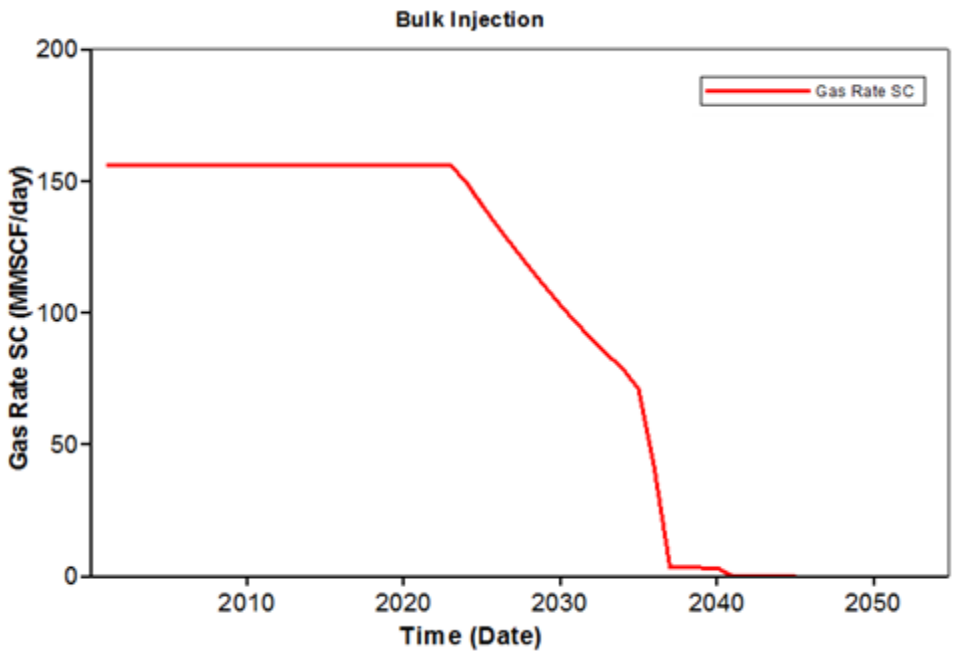

Figure 3.5—CO_2 injection rate for bulk injection with decrease in rate after maximum bottom-hole pressure is reached.

The effect of water vaporization discussed in Section 3.1 affects the injectivity of CO_2. Vaporization of the brine reduces water saturation thereby increasing the effective gas mobility. Figure 3.6 shows the effect of water vaporization on CO_2 injectivity and

thus storage efficiency. Also, an estimate of the injectivity gained by modeling vaporization effect was performed and found to be comparable to formation stimulated with a skin factor of –2.5.

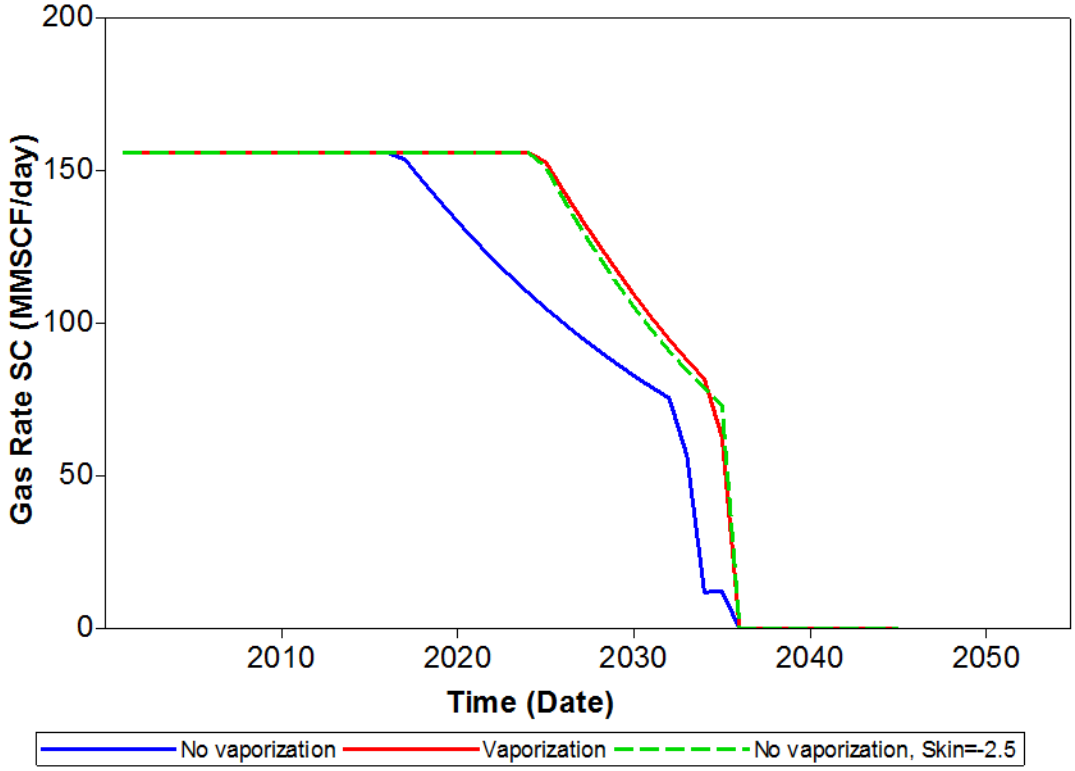

Figure 3.6—Effects of vaporization on CO_2 injection.

3.2.2 CO_2-Brine displacement with external brine disposal

This section shows simulations for CO_2 displacing brine. Produced brine is to be disposed in the same manner as produced oilfield brine. Operational cost for brine disposal will be discussed in a later chapter.

3.2.2.1 Quarter five-spot pattern

The five-spot pattern common in waterflooding surrounds each production (injection) well with four injection (production) wells. It is common practice to simulate this configuration as a quarter five-spot with the injection well on one corner and the

production well on the opposite corner. Each well in the simulation injects or produces ¼ of the actual well rate. The model boundaries are closed. This conceptual approach is justified when the pattern extends indefinitely in all directions. Because no pattern has infinite extent, this is an idealization of reality.

For this study, the quarter five-spot pattern dimensions of 16250 ft × 16250 ft × 528 ft were discretized into gridblocks of 25 × 25 × 16, and as before the simulation used aquifer properties in Table 3.1. The main objective of the simulation was to determine the storage efficiency when brine is produced under voidage displacement conditions. For this simulation, storage efficiency is computed as the cumulative reservoir volume of CO_2 injected when breakthrough occurs at the brine production well divided by the pore volume of the quarter five-spot simulation.

An effort was made to estimate the storage efficiency using an analogy to existing waterflooding models. The mobility ratio for the CO_2-brine displacement was computed as 14.52. For a five-spot with this mobility ratio, the expected displacement efficiency (Willhite 1986) would be 0.474.

For the simulated five-spot pattern, initial efforts showed that the brine productivity controlled the well rates in the displacement because brine productivity is less than CO_2 injectivity from the beginning, and the latter improves over time as the diameter of the radial zone saturated by CO_2 near the wellbore increases. To see this note that brine productivity at bottom-hole conditions is approximately

$$\frac{q_{w,r}}{\bar{p}-p_{wf}}=\frac{kh}{141.2\mu_w\left[\ln\left(d/2r_w\right)+s\right]} \tag{3.1}$$

where d is the distance between the two wells, whereas CO_2 productivity is approximately

$$\frac{q_{CO_2,r}}{p_{wi}-\bar{p}}=\frac{kh}{1412\mu_w\left[\frac{\mu_g}{k_{r,S_{CO_2}=1}}\ln\left(\frac{r_{dry}}{r_w}\right)+\left(\frac{k_{rCO_2}(S_{CO_2,avg})}{\mu_{CO_2}}+\frac{k_{rw}(S_{CO_2,avg})}{\mu_w}\right)^{-1}\ln\left(\frac{r_{BL}}{r_{dry}}\right)+\mu_w\ln\left(\frac{d}{2r_{BL}}\right)+s\right]} \tag{3.2}$$

(modified from(Burton et al., 2008)). If the mechanical skin, s for each well is zero, the ratio of the productivity to the injectivity is

$$\frac{J}{I}=\frac{\frac{\mu_g}{k_{r,S_{CO_2}=1}}\ln\left(\frac{r_{dry}}{r_w}\right)+\left(\frac{k_{rCO_2}(S_{CO_2,avg})}{\mu_{CO_2}}+\frac{k_{rw}(S_{CO_2,avg})}{\mu_w}\right)^{-1}\ln\left(\frac{r_{BL}}{r_{dry}}\right)+\mu_w\ln\left(\frac{d}{2r_{BL}}\right)}{\mu_w\ln\left(d/2r_w\right)} \tag{3.3}$$

Because the last term in the numerator of Eq.3.3 is much larger than the other two and much smaller than the denominator, it is easily seen that brine productivity limits the displacement rate. However, the displacement rate can be increased if the brine production well is pumped to a lower flowing pressure than the 1200 psi used in the simulation.

The CO_2 injection rate for the quarter five-spot was 194×10^5 SCF/day in a vertical well located at i =25, j =25 and perforated at k = 14-16. The pressure of the aquifer changes with time during injection and production operation. Therefore, to maintain voidage displacement, the brine production rate will vary with time. The CMG keyword *VRI_GROUP (Injection Group for Group Recycling/Voidage Replacement) is used to achieve this purpose. Figure 3.7 shows the cumulative CO_2 injection and the cumulative brine produced. It can be seen from Figure 3.7 that both curves overlap throughout the simulation. Figure 3.8 shows the brine production rate needed to maintain voidage replacement. It can be seen from Figure 3.8 that the brine production rate reduces with time because of pressure increase and consequently density increase. The brine was produced for a well located at i = 1, j = 1 and perforated at k = 14–16. Figure 3.9 shows a saturation profile of the gas at breakthrough.

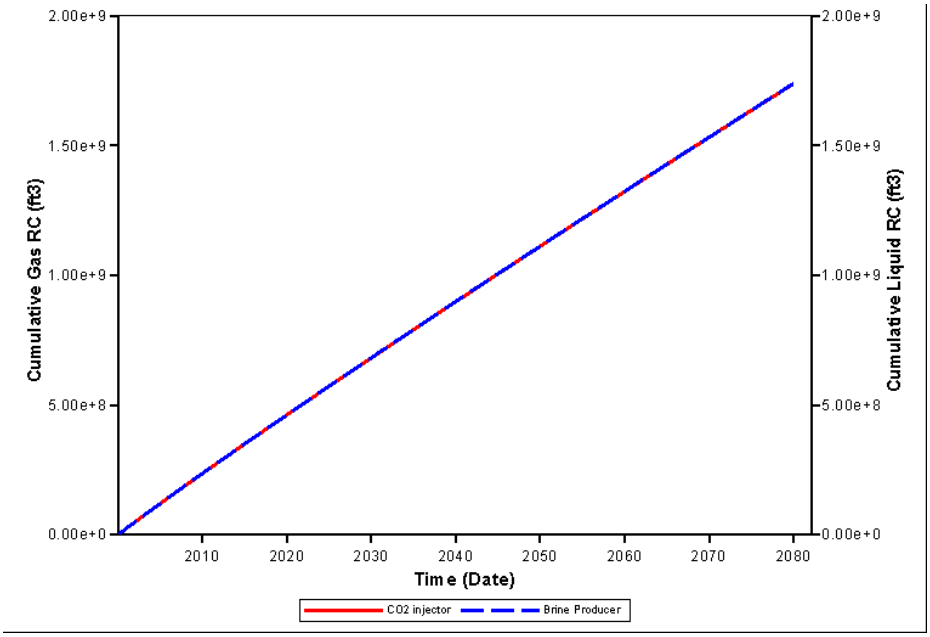

Figure 3.7—Quarter five-spot CO_2-brine displacement volume balance.

At the above well rates, CO_2 breakthrough occurred at the 75th year and the calculated storage efficiency at breakthrough is 7.49%, significantly less than what would be estimated from waterflooding models for the same mobility ratio. The reason, of course, is that when water displaces more viscous oil, the oil and water densities are much more similar than when supercritical CO_2 displaces brine. In the former case, the oil to water density ratio may be ~0.9, whereas the CO_2 to water density ratio for this study was about 0.714. The waterflood analog is not appropriate, and better insights may be found in EOR literature concerning CO_2 flooding.

Although lower than predicted by the waterflooding analog, the CO_2-brine displacement efficiency is about 12 times more than the storage efficiency of the bulk injection case. As such, for this hypothetical study, although the Woodbine aquifer can support bulk injection storage for no more than 20 years, the same aquifer could provide storage for ~240 years for the same plants under CO_2-brine displacement.

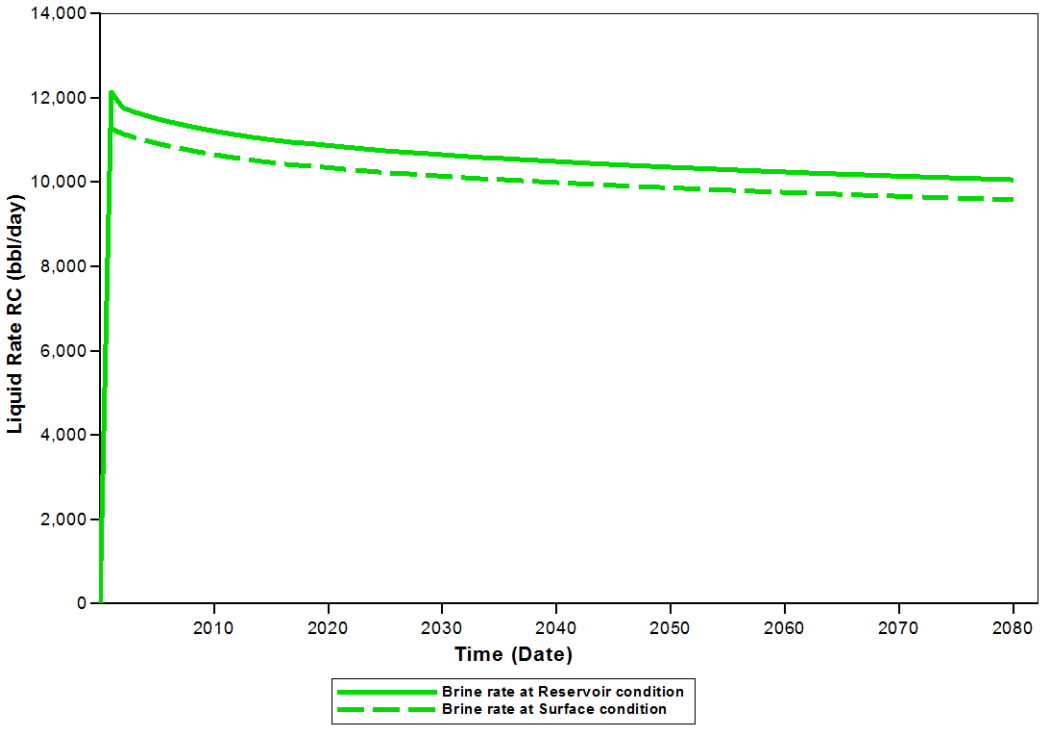

Figure 3.8—Brine production rate at surface and reservoir condition for quarter five-spot CO_2-brine displacement.

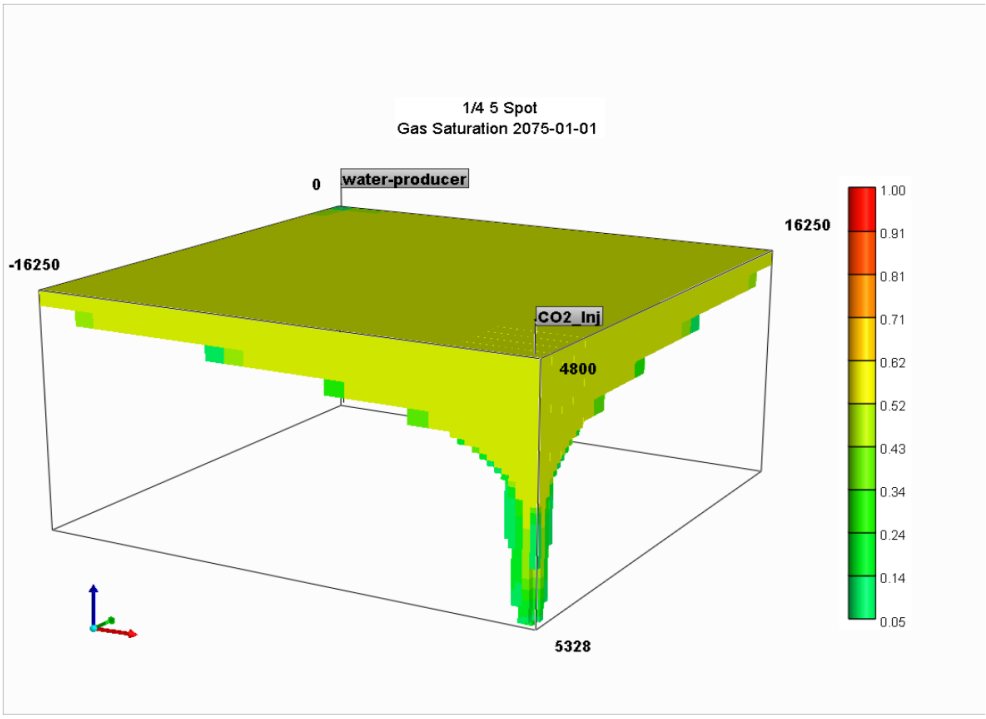

Figure 3.9—Breakthrough CO_2 saturation for quarter five-spot CO_2-brine displacement.

3.2.2.2 Injector/producer couplet pattern

The quarter five-spot simulation shown in the previous section only applies rigorously for an extensive pattern of many wells. The next case considers only two wells: one CO_2 injector, and one brine producer. A 3D homogeneous aquifer with dimensions of 43550 ft × 43550 ft × 528 ft was discretized into gridblocks of 67 × 67 × 16. In this case, the injectors and producers are not kept at the boundary of the aquifer. Instead, a large enough reservoir volume is provided between the injector/producer couplet and the aquifer boundary, which minimizes the impact of the simulation outer boundary on the behavior of the two wells.

The CO_2 injection rate is 78×10^6 SCF/day using a bottom vertical well perforated at i = 46, j = 46 and k = 14–16. The reservoir volume balance between injected fluid and produced fluid is maintained as the previous case. The brine production rate ranges between 40,000 to 44,000 bbl/day using a bottom vertical well located at i = 22, j = 22 and perforated at k = 14–16. Figure 3.10 shows a saturation profile of the gas at breakthrough.

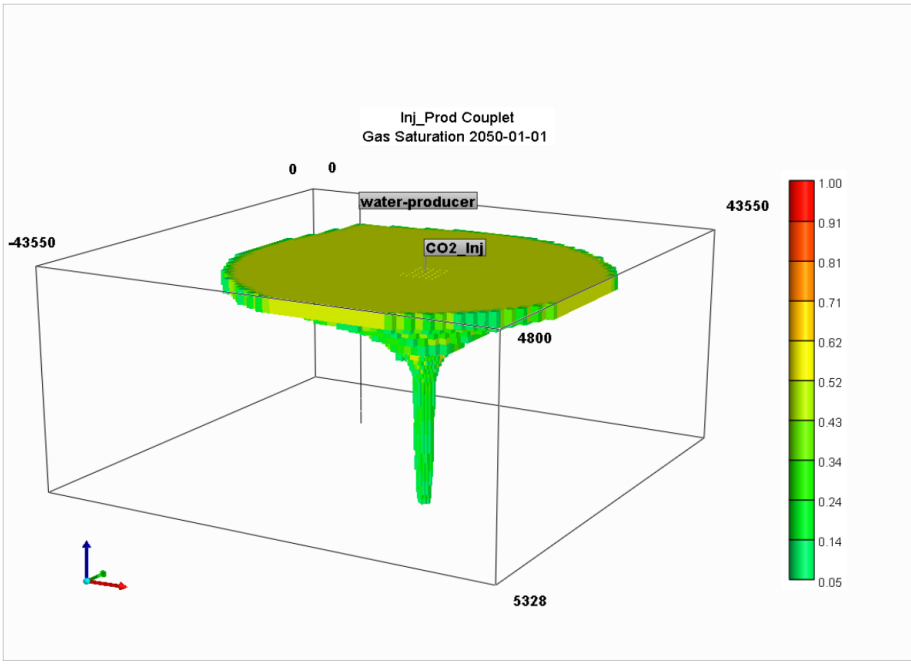

Figure 3.10—Breakthrough CO_2 saturation for injector/producer couplet CO_2-brine displacement pattern.

Using the above injection and production rates and aquifer conditions, CO_2 breakthrough occurred at the producer at the 50^{th} year. The storage efficiency calculated as the reservoir volume of the cumulative CO_2 injected up until breakthrough divided by the pore volume at or below the CO_2 plume was 6.41%.

3.2.2.3 Staggered line drive pattern

For two injection and two production wells, a staggered-line drive pattern was simulated because this is the analog to the five-spot pattern when viewed at a 45 degree angle. A 3D homogeneous aquifer with dimensions of 53950 ft × 53950 ft × 528 ft discretized into gridblocks of 83 × 83 × 16. As in the previous case, a large enough reservoir volume is provided between the injectors/producers and the aquifer boundary, which minimizes the impact of the simulation outer boundary on the behavior of the four wells. Each CO_2 well was injected at a rate of 39×10^6 SCF/day with the wells located at $i = 46, j = 46$, and $i = 22, j = 22$, and perforated at $k = 14–16$. The volume balance between injected fluid and produced fluid is maintained as in the previous case giving the brine production rate at each producer ranges from 20,250 to 22,500 bbl/day with the producing wells located at $i = 22, j = 46$, and $i = 46, j = 22$, and perforated at $k = 14–16$. Figure 3.11 shows a saturation profile of the gas at breakthrough.

Using the above injection, production rates and aquifer conditions, CO_2 breakthrough at the producer at the 46^{th} year and the calculated displacement efficiency is 5.09%, somewhat lower than either of the previous two displacements.

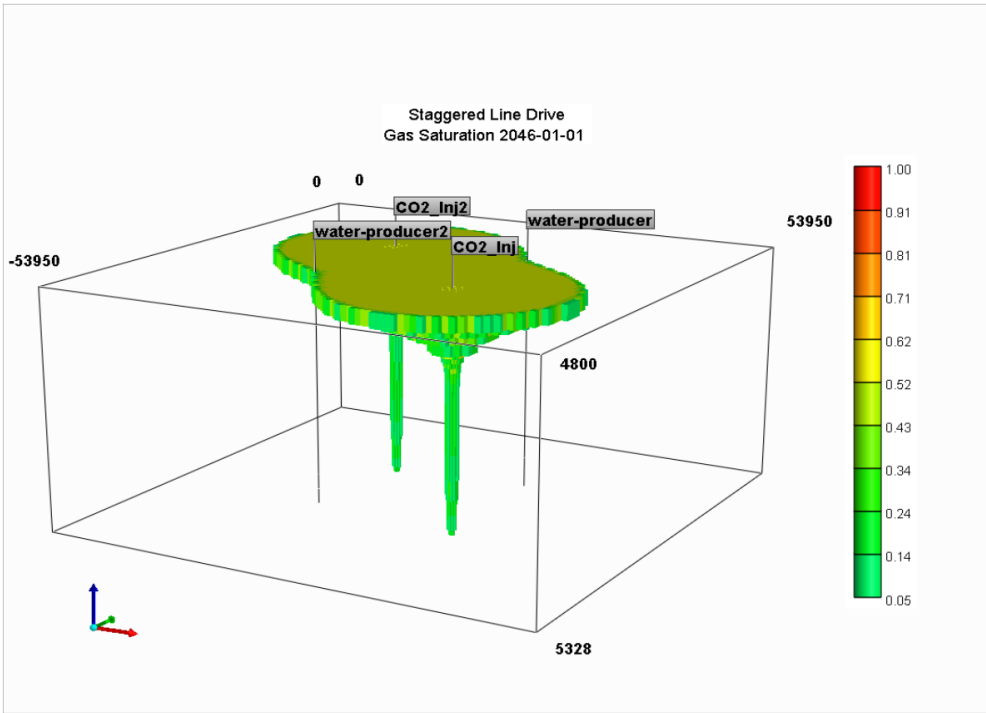

Figure 3.11—Breakthrough CO_2 saturation for staggered line drive CO_2-brine displacement pattern.

3.2.2.4 Reoriented staggered line drive pattern

The lower displacement efficiency observed for the four well staggered-line drive pattern compared to the five-spot and the two well couplet was not anticipated. However, this simulation was conducted with injection to production paths that followed the grid direction, whereas in the other two cases, the displacement progressed diagonally through the simulation grid. Therefore, the simulation was repeated with the same well spacing but with the wells oriented in the grid such that the displacement progressed diagonally. A 3D homogeneous aquifer with dimensions of 54,750 ft × 54,750 ft × 528 ft was discretized into gridblocks of 73 × 73 × 16. As before, each CO_2 well was injected at a rate of 39×10^6 SCF/day with the wells located at i = 50, j = 37, and i = 23, j = 37, and perforated at k = 14–16. Again, the brine production rate at each producer ranged from 24,900 to 24,965 bbl/day with the wells located at i = 37, j = 24, and i = 37, j = 50, and perforated at k = 14–16. Figure 3.12 shows a saturation profile of the gas at breakthrough.

Using the above injection, production rates and aquifer conditions, CO_2 breakthrough at the producer at the 50^{th} year and the calculated displacement efficiency is

5.15%, about the same as the previous simulation. Therefore, the reduction in displacement efficiency was not caused by a grid orientation effect.

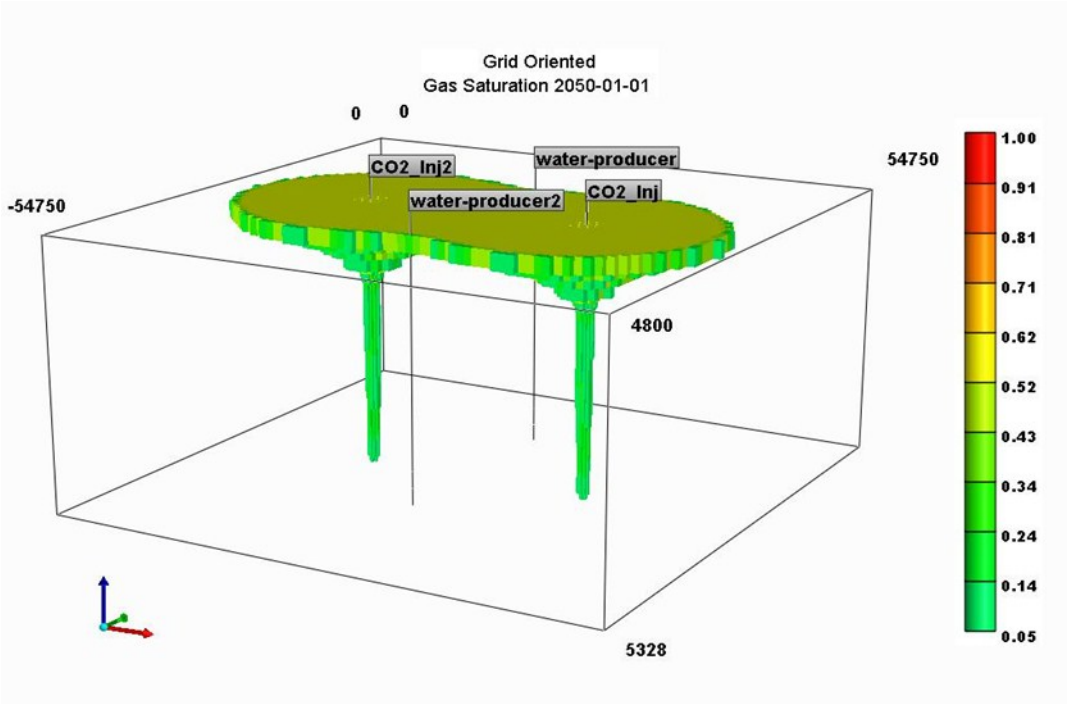

Figure 3.12—Breakthrough CO_2 saturation for reoriented staggered line drive CO_2-brine displacement pattern.

3.2.3 CO_2-Brine displacement with internal saturated brine injection

In practice, produced oilfield brine is disposed as bulk injection into an aquifer, much the same as is considered for the CO_2 in the previous section. One might wonder why there should be any concern about bulk CO_2 injection. The reason is that the volumes to be disposed dwarf what has been done in the oilfield if a high percentage of the CO_2 currently emitted to the atmosphere from coal-fired power plants is to be disposed in aquifers. Current power production from coal-fired power plants in the United States is about 340 gigawatts (United States Energy Information Agency 2008), and the CO_2 produced per year is about 2 billion tonnes per year. If all of this were to be disposed in aquifers, this would correspond to approximately 50 million barrels per day for an average aquifer depth of about 5,000 ft. Currently about 40 million barrels per day

of oilfield brine is injected in the US, but much of this water also comes from saline aquifers, and the net amount injected is much less. That being said, oilfield brine injection could be used as an analog to bulk CO_2 injection and could provide more confidence in the feasibility of this approach.

In this section, the possibility of desalinating the produced brine and injecting the saturated brine back into the same aquifer into which CO_2 will be injected was investigated. This approach is somewhat like the engineered approach to aquifer management proposed by Anchliya and Ehlig-Economides, 2009. However, in this case, the brine injection rate is governed by the brine salinity, and not by an objective to prevent the CO_2 plume from rising to the aquifer top. The latter may require a different approach to brine production and injection well rates and locations. For this preliminary evaluation, the same injection and production well geometries are used as in the previous section except that the saturated brine is injected in the same aquifer directly above the CO_2.

To maintain a volume balance, the sum of the volumes of injected CO_2 and saturated brine injected is produced as native brine at reservoir conditions. Assuming the salinity of saturated brine is S_b = 350,000 ppm, the volume of saturated brine to be injected will be $V_{sat.brine} = xV_{CO2}$ where x has a value between 0 and 1.

$$x = \left(1 - \frac{1350 - 1000\left(1 + \frac{S_b}{10^6}\right)}{350}\right) \tag{3.4}$$

where x is the ratio of saturated brine volume to CO_2 volume and S_b is the salinity of the aquifer in ppm. The volume of the native brine to be produced is

$$V_{native.brine} = (1 + x)V_{CO2} \tag{3.5}$$

The Woodbine aquifer has a salinity of 90,000 ppm in the region of the injection zone, therefore x has a value of 0.257 and the volume of produced brine will be 1.257 times the volume of CO_2 injected. Figure 3.13 shows a plot of x vs. salinity. At values of

x greater than 0.5 (180,000 ppm), this method of aquifer management could become prohibitive as the cost of desalination and saturated brine handling would exceed economic feasibility.

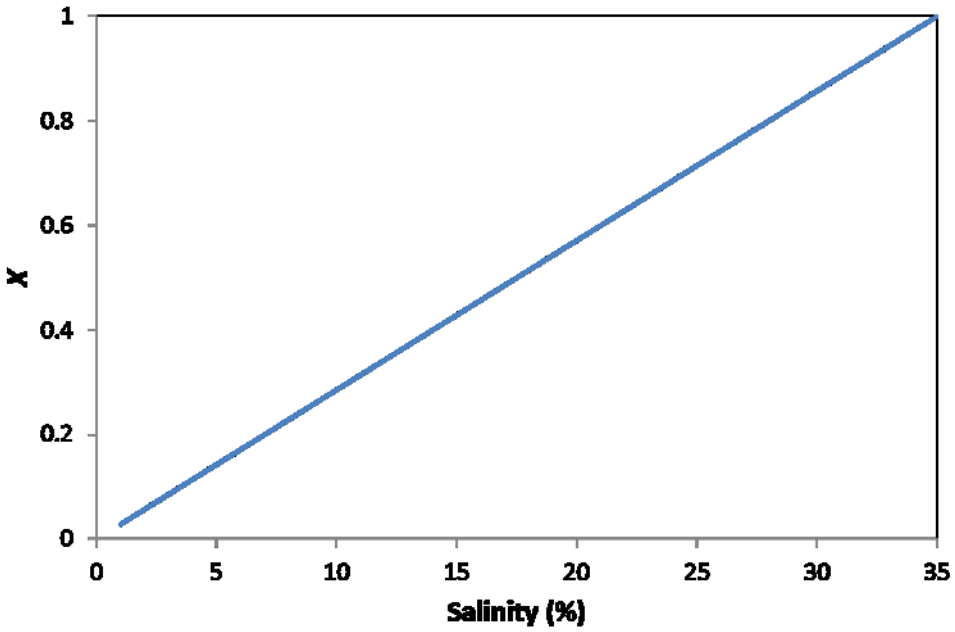

Figure 3.13—Relationship between saturated brine fraction of produced brine, x and salinity.

3.2.3.1 Quarter five-spot pattern

With the CO_2 injection and brine production wells located as before with the same CO_2 injection rate, for this case the saturated brine injector is injected at a rate of 2700 bbl/day from a well located at $i = 25$, $j = 25$ and perforated at $k = 3$–5. To keep volume balance, the brine is produced at a rate ranging from 12,200 to 13,000 bbl/day. The saturation profile of CO_2 at breakthrough is shown in Figure 3.14.

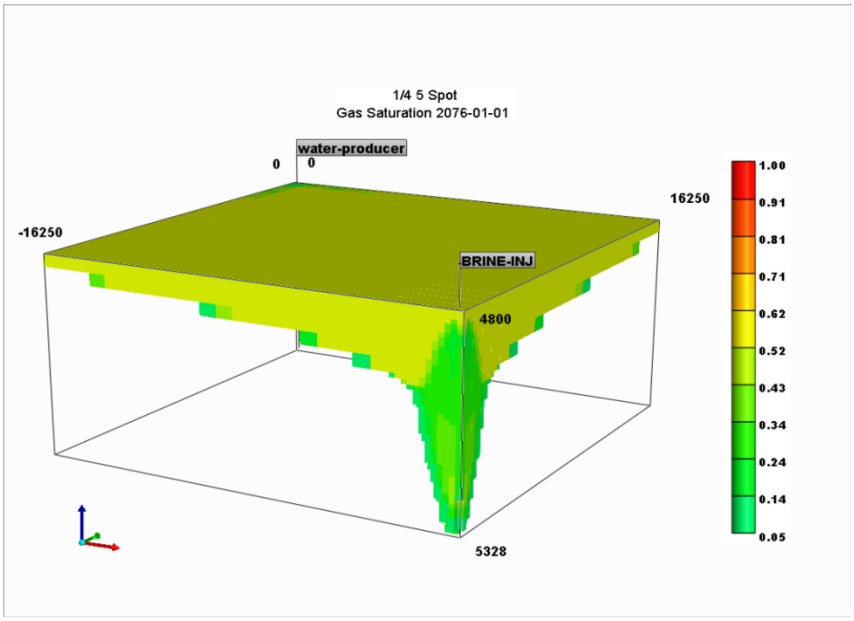

Figure 3.14—Breakthrough CO_2 saturation for quarter five-spot CO_2-brine displacement pattern (brine injection included).

The CO_2 breakthrough occurred in the 76th year for a calculated breakthrough displacement efficiency of 7.23%. For this well pattern, saturated brine injection reduced the displacement efficiency while maintaining the same breakthrough time.

3.2.3.2 Injector/producer couplet pattern

With the CO_2 injection and brine production wells located as before with the same CO_2 injection rate, for this case the saturated brine injector is injected at a rate of 10,800 bbl/day from a well located at i = 46, j = 46 and perforated at k = 3–5. To maintain reservoir volume balance, the brine is produced at a rate ranging from 50,550 to 56,475 bbl/day. The saturation profile of CO_2 at breakthrough is shown in Figure 3.15.

The CO_2 breakthrough occurred in the 45th year and the calculated storage efficiency at breakthrough is 6.07%. As for the quarter five-spot pattern, saturated brine injection reduced displacement efficiency from what was achieved previously for the same geometry, but was still about 13 times the bulk injection storage efficiency.

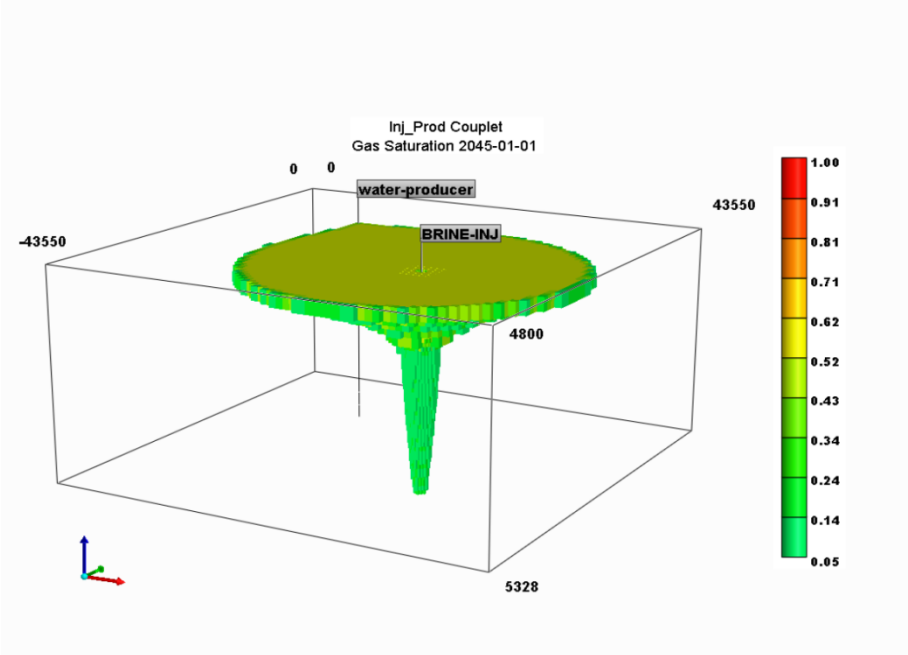

Figure 3.15—Breakthrough CO_2 saturation for injector/producer couplet CO_2-brine displacement pattern (with brine injection).

3.2.3.3 Staggered line drive pattern

With the CO_2 injection and brine production wells located as before with the same CO_2 injection rate, for this case the saturated brine injector is injected at a rate of 5400 bbl/day from a well located at i = 46, j = 46 and perforated at k = 3–5. The brine is produced at a rate ranging from 26,800 to 28,800 bbl/day per well. The saturation profile of CO_2 at breakthrough is shown in Figure 3.16.

The CO_2 breakthrough occurred in the 44th year and the calculated storage efficiency at breakthrough is 4.96%. The reoriented case was also simulated with a resulting 5.19% displacement efficiency.

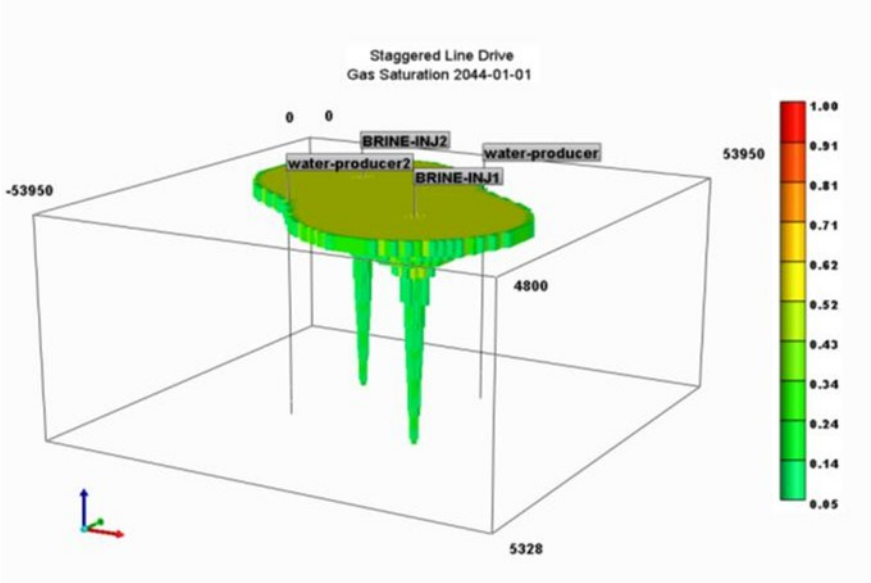

Figure 3.16—Breakthrough CO_2 saturation for staggered line drive CO_2-brine displacement pattern (with brine injection).

3.3 Chapter Conclusions

This chapter evaluates the storage capacity of the Woodbine aquifer and estimates the project life of a CO_2 sequestration project in the aquifer using three aquifer management strategies. All models used are homogeneous and are assigned average reservoir properties of the aquifer.

Preliminary result shows that the storage efficiency of bulk injection strategy is only 0.46% and CO_2-brine displacement strategies result in more than 10-fold increase to about 7.49% depending on injection pattern used. Considering the injection of a total of 62.2 million tonnes per year of CO_2 in a sequestration zone with a pore volume of 2,520 billion res bbl selected based on its high net sand thickness and salinity, aquifer pressurization limits bulk injection to only 20 years, whereas a CO_2-brine displacement method would continue about 240 years until CO_2 begins to break through in production wells.

Conceptual modeling using Woodbine aquifer properties is encouraging, but it does not address mapped heterogeneity and structural complexity. The next chapter will describe preparation of a geological model for full-field simulation study of the

Woodbine aquifer and fluid flow modeling. This work offers important insights not addressed by the conceptual modeling including the potential for salt water intrusion on fresh water and fluid migration across faults.

CHAPTER IV

GEOLOGIC MODEL AND FLUID FLOW SIMULATION OF WOODBINE AQUIFER CO_2 SEQUESTRATION

The conceptual models in Chapter III were made by assuming average reservoir properties such as porosity, permeability, and net thickness. Such homogeneous systems are typically used in showing trends that should be expected in a typical reservoir.

In this chapter, we create a geologic model by using contour maps of depth (formation tops), formation thickness (formation bottoms), net sand thickness, porosity, and permeability, as well as a fault map. Aquifer management methods proposed in the previous chapter are reproduced in the context of the more realistic field scale model and result in similar conclusions regarding pressurization under bulk CO_2 injection and greater storage efficiency from CO_2-brine displacement mechanisms. However, the model also enables evaluation of a potential risk of salt water intrusion or CO_2 contamination into the fresh water aquifer updip from the saline aquifer region into which CO_2 is injected.

4.1 Geologic Model

A geological model requires the integration of geological, petrophysical, and reservoir engineering data. The goal of reservoir modeling is to convert the geological model into a flow model or simulation model. Petrophysical data used to develop the geological model for this study is found on the Bureau of Economic Geology (BEG) website. The U.S. Geological Survey digital elevation model for the Woodbine aquifer provided input data to delineate the structure top in the geological model.

In this study, CMG Builder was used to create a 3D geologic model. First a contour plot of the formation top map and the fault map was imported into CMG. The structural maps were used to create non-orthogonal corner point grids. The outer boundary of the reservoir was mapped by selecting appropriate locations on the contour map to specify control points along the boundary. Next, internal vertical and horizontal

control lines were used to indicate faults within the area defined by the outer boundary lines. A single zone 10-layer reservoir model with 95 × 98 gridblocks was used to model the reservoir.

To create the reservoir structure, the CMG Builder interpolates input maps of the grid top and grid thickness using the parent block values to determine the values in other parts of the grid. When grid points are either too far from the map or surrounded by faults, non-interpolated values are calculated using an inverse distance weighted average based on nearby gridblocks.

Because up to now they have not offered any economic value, typically subsurface properties of brine formations are scarce and generally not compiled in easy-to-access format. Realistic and quantitative data about the characteristics of the subsurface is needed to estimate the storage potential of a formation.

Geologic data for some reservoir parameters of the Woodbine aquifer were provided by the Brine-Formation database on the Bureau of Economic Geology (BEG) website. The geologic attributes provided by the database include depths, thickness, net sand thickness, and sand-body continuity maps. The database also contains properties that have been determined from previous deep-well injection studies and oil and gas data sets by researchers who have worked on parts of the formation. . The BEG database map files are in the shape format (.shp) and can be accessed using ESRI ArcView, although the reservoir simulation of choice, CMG, does not accept the shape format. Therefore, mapped data were first imported into Neuramap, reprocessed, and the format changed into a ZMAP CNTR format that could be used in CMG.

4.1.1 Structural properties

The structural properties of a formation are modeled by defining its structural top and the set of faults that runs through it. In most cases, the structural top is defined on the basis of the geophysical interpretation of a 2D or 3D map. The structure on top of the Woodbine had been digitized by Core Labs (1972), and its depth below land surface was calculated using the U.S Geological Survey digital elevation model.

The Woodbine dips gently from its outcrop in the northwest of the East Texas Basin to the Gulf of Mexico in the south of the basin. The depth of the Woodbine ranges

from 500 ft above sea level in the outcrop region to 11,000 ft below sea level at its down-dip region in the South. Figure 4.1 shows a map of the formation top in the Woodbine. A negative value indicates that the depth is above sea level.

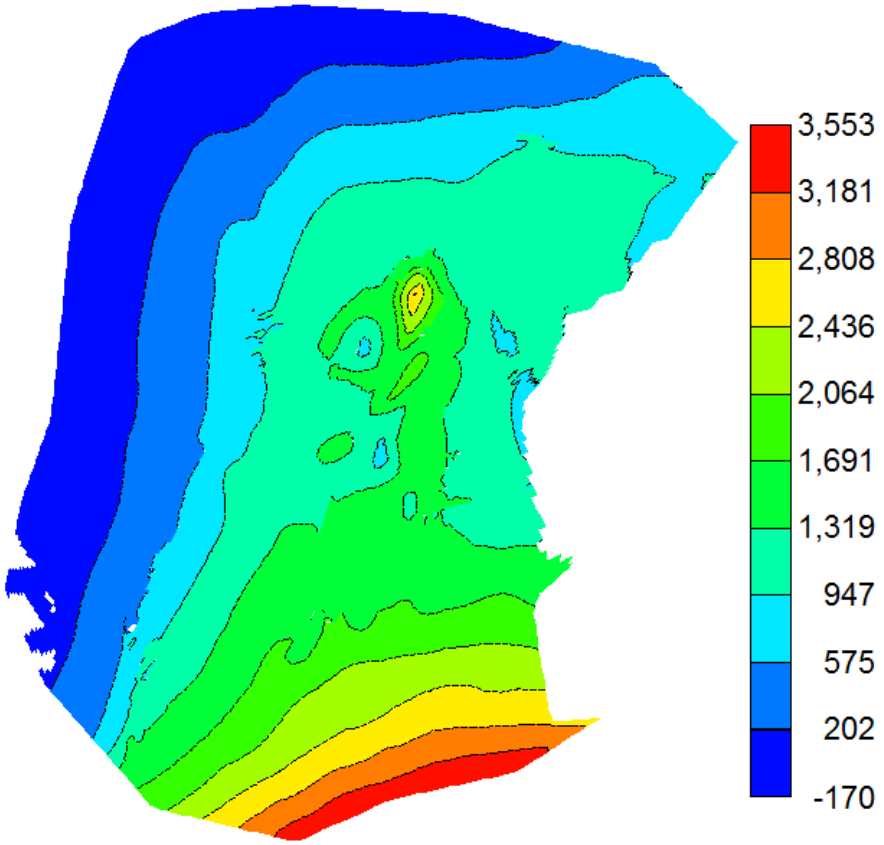

Figure 4.1—Woodbine formation top contour plot (m).

The thickness of the Woodbine varies from about a 100 to 1100 ft. It is thickest at the center of the East Texas Basin. Figure 4.2 shows the thickness contour map of the Woodbine.

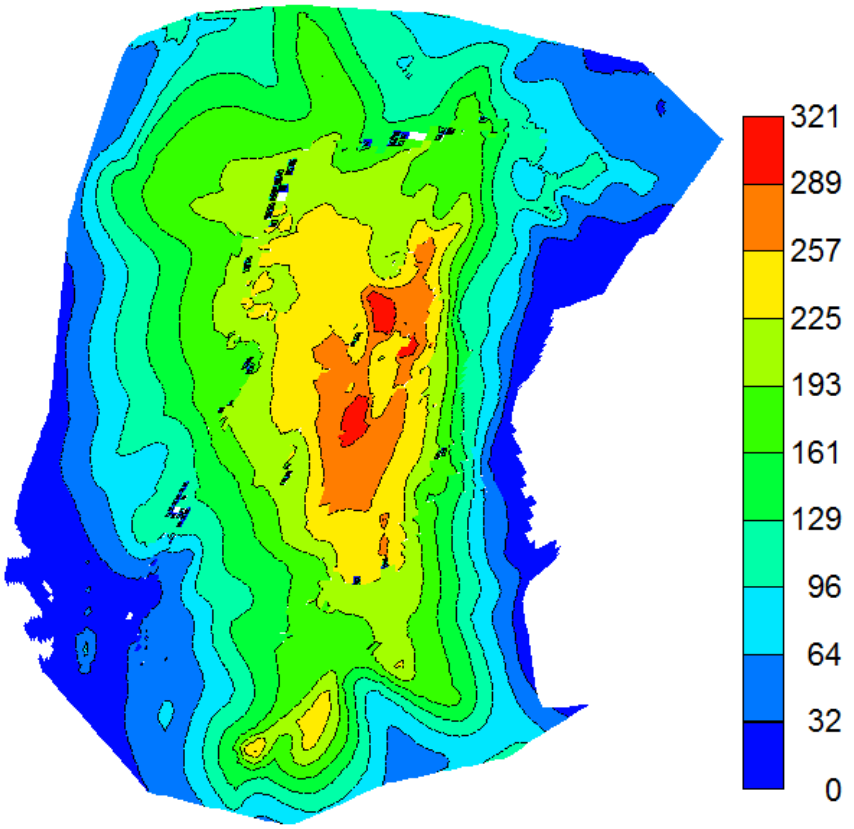

Figure 4.2—Woodbine formation thickness map contour plot (m).

The net sand thickness of the Woodbine formation ranges from about 50 to 500 ft. Figure 4.3 shows the net sand thickness contour map of the Woodbine.

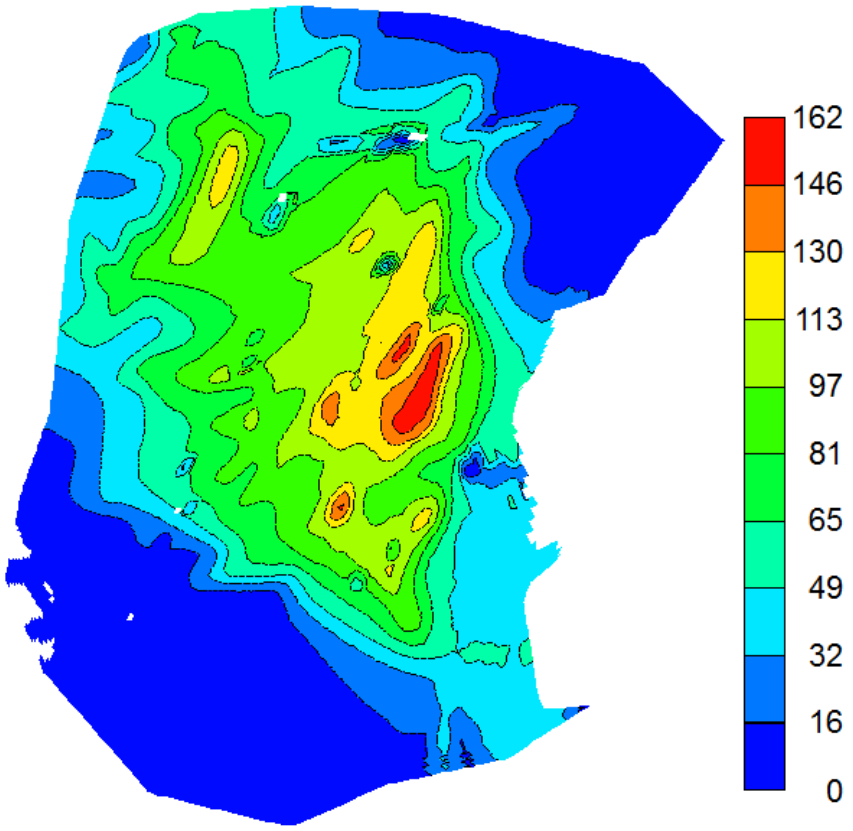

Figure 4.3—Woodbine formation net thickness map contour plot.

The Woodbine has a complex structure with two major fault systems: the Mexia-Talco fault system in the west and north of the East Texas Basin and the Mount Enterprise fault zones on the southern flank of the East Texas Basin. All faults not in these zones are called central basin faults. A fault map of the Woodbine is shown in Figure 4.4.

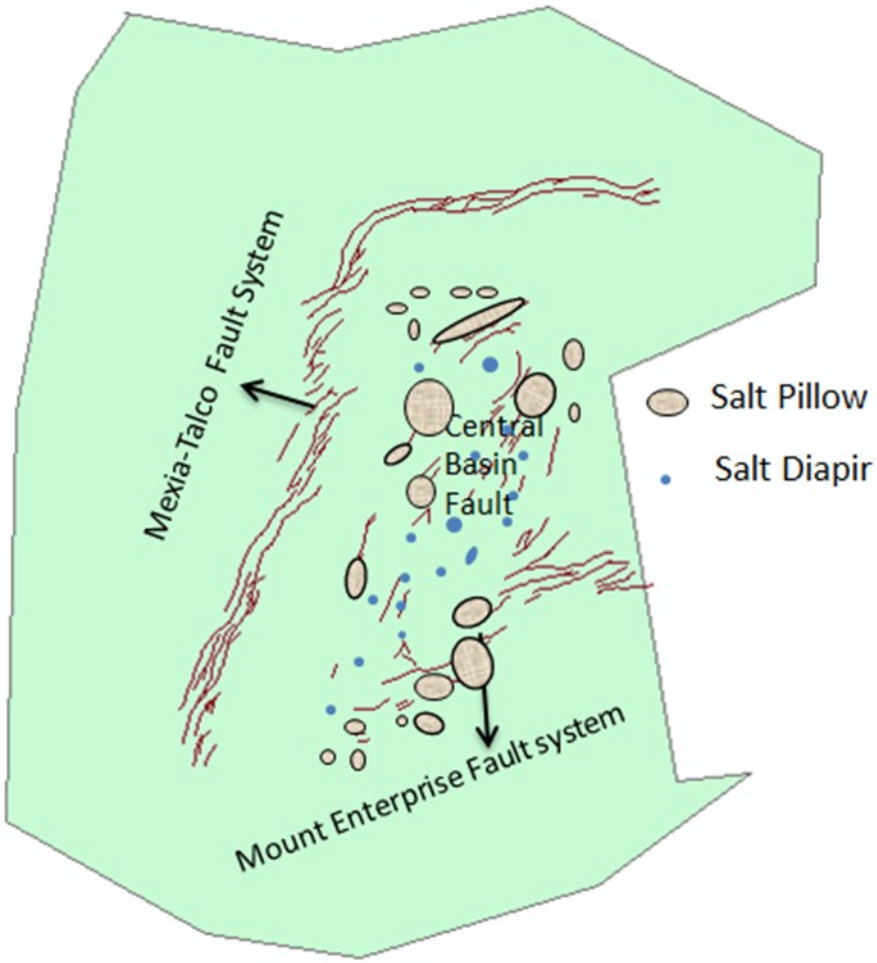

Figure 4.4—Woodbine formation fault map.

4.1.2 Petrophysical properties

The typical value of the porosity of the lower Woodbine sandstone is about 25%, with permeability values range from ~ 100 to 1200 mD. The more sorted upper Woodbine sandstones have porosity values ranging from 25% to 30% with permeability values of greater than 3000 mD (FutureGen Alliance 2007).

According to Wang et al. (2008), the major producing lithofacies of the Woodbine, have high-quality fluvial and distributary channel sandstones with average porosity and permeability of 25.2% and 2098 mD, respectively. A study of the core porosity and permeability from 30 wells across the formation gives a trend that can be expressed as

$$k = 10^{0.2667(\phi - 15)} \tag{4.1}$$

where k is the permeability in mD and ϕ is the porosity (%).

Reported porosity and permeability values in the Woodbine are shown in Figures 4.5 and 4.6. Raw data were extracted from the Railroad Commission of Texas well files (Holtz, 1997), which provides an overview of the properties of the Woodbine producing interval.

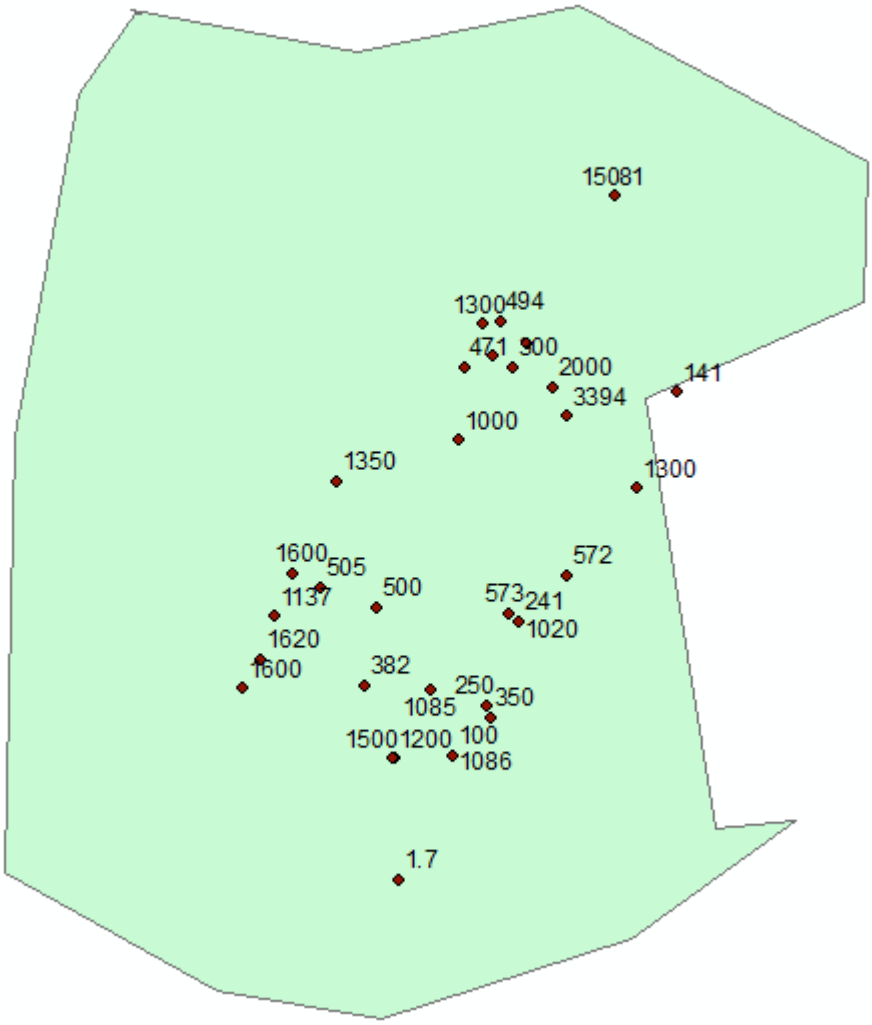

Figure 4.5—Permeability data in the Woodbine aquifer (mD).

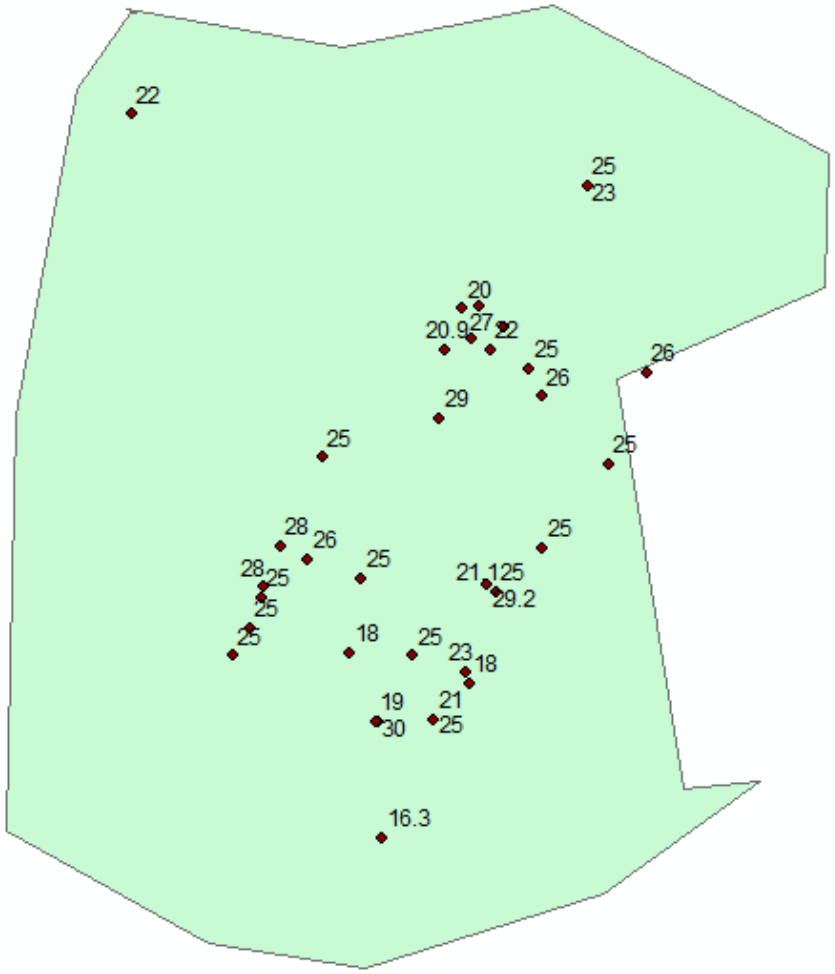

Figure 4.6—Porosity data in the Woodbine aquifer (%).

Populating a 3D geological model with petrophysical properties can be challenging. One of the challenges of constructing a 3D geological model of the Woodbine is the paucity of data. Petrophysical data needed for reservoir simulation frequently are obtained from core plugs, well logs, and well-test analysis. Generally, the available information is insufficient compared to the size of the reservoir. Also, the data collected are at different scales with various degrees of reliability. The information available along the well logs must be honored (Beucher and Renard 2009). Geostatistics can be used to successfully analyze and integrate different types of data, provide meaningful results for model building, and quantitatively assess uncertainty for risk management (Yarus and Chambers 2006).

The common geostatistical technique consists of generating information known at only a few conditioning samples by linearly combining these data onto a large number of grid cells. The geostatistical technique used in this study is the Sequential Gaussian Simulation (SGS) method. This is a suitable choice for the depositional geology described in Chapter II. A realization of the porosity and permeability field is shown in Figure 4.7.

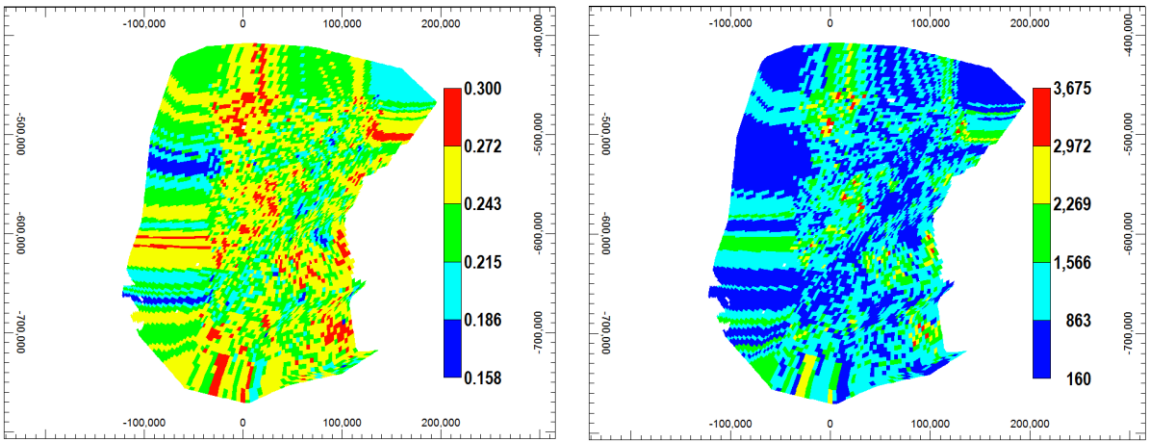

Figure 4.7—Geological model showing porosity and permeability distribution.

4.2 Aquifer Management Strategies

The aquifer management strategies proposed in Chapter III (bulk injection and CO_2 brine displacement) were simulated using the geological model. For this study, the Woodbine aquifer is subdivided into three regions: (1) an outcrop region towards the northwest, (2) the fresh water region, and (3) the saline water region. The proposed injection site for CO_2 sequestration is in the saline region. The saline and fresh regions of the aquifer are separated by a fault system that may or may not be fully sealing. As such, when CO_2 is injected, there is a possibility that brine will be displaced from the saline part of the aquifer up dip into the fresh water region through partially transmissive faults. In turn, fresh water may ultimately escape through the aquifer outcrop. A map of the Woodbine aquifer delineating the three regions is shown in Figure 4.8. The model locates a gas-water contact at the boundary between the fresh water and outcrop regions. The

outcrop region is meant to represent water escaping at the outcrop location either as spring water or through vaporization and acts like a boundary at atmospheric pressure.

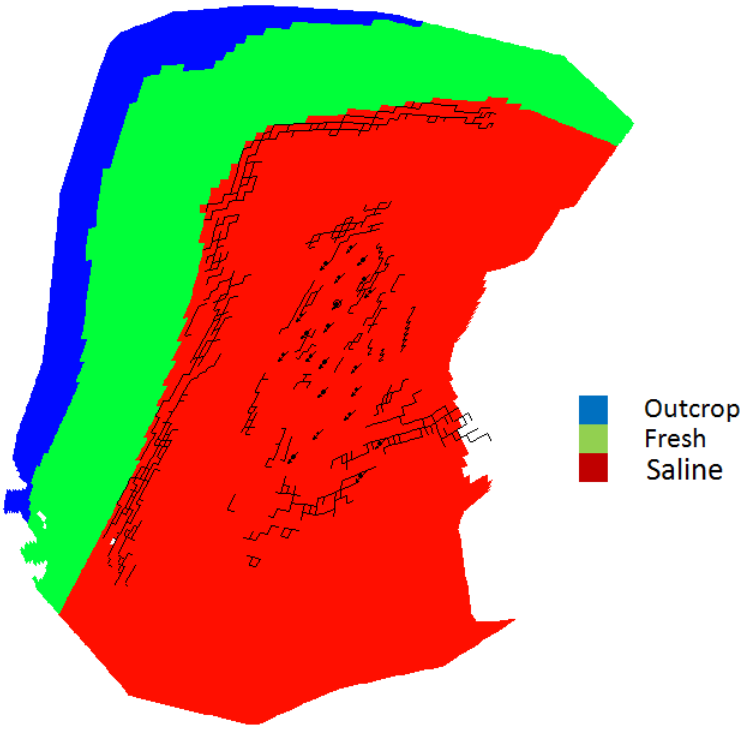

Figure 4.8—Map of the Woodbine aquifer showing the three different regions.

4.2.1 Injection well locations

The portion of the woodbine aquifer proposed in this study for CO_2 sequestration is the part east of the Mexia-Talco fault system where the aquifer is both saline and thick. From our analysis in Chapter III, this portion is an area with approximate dimensions of 100 km (62.5 mi) by 200 km (125 mi). The total dissolved solids concentration of the aquifer brine in this region varies from 50,000 ppm to 200,000 ppm.

The important parameters to be considered in selecting injection well locations are transmissibility ($T = kh$), distance to a fault, and inter-well distance. Transmissibility is the product of the effective permeability k and net thickness h of the aquifer. The higher the transmissibility of the aquifer, the easier it is for fluids to be injected into the aquifer. Injectivity is lower when a well is close to a fault or another injection well. The

fault acts as a no-flow boundary and limits the active storage area of the well, whereas a virtual no-flow boundary is formed midway between any two injection wells. The CO_2 injectors are vertical wells that are perforated from the 5th to the 10th gridblock layer to improve injectivity.

In the injection well model used, the reservoir flow rate is a function of the injectivity index, the wellbore pressure, and the pressure at grid center point using the relationship (CMG, 2010):

$$Q_j = \sum_l WI_{j,l}\lambda_{T,l}\left(P_{bh} - P_{o,i}\right) \quad j = g, w \tag{4.2}$$

$$WI = 2\pi ffkh\frac{w_f}{ln\left(r_e/r_w\right)+s} \qquad j = g, w \tag{4.3}$$

where

Q_j = flowrate of Phase j ($j = g, w$) at reservoir conditions (m^3/day)

P_{bh} = bottom-hole pressure (kPa)

$P_{o,i}$ = pressure at i-th gridblock containing the well (kPa)

$WI_{j,l}$ = well injectivity index for Phase j ($j = g, w$) to Layer l

l = layer

w_f = well flowing fraction

k = effective permeability in the plane perpendicular to the well direction (mD)

h = gridblock thickness in the well direction (m)

$\lambda_{T,l}$ = total mobility of fluid in the well block

r_e = effective radius for well cell

r_w = wellbore radius (m)

s = skin

ff = fraction of completion of the well in the gridblock.

g = gas

w = water

The number of injection well n required for bulk injection is given by the equation

$$n = \frac{\text{power plant } CO_2 \text{ output } \left(\frac{\text{MMSCF}}{\text{D}}\right)}{CO_2 \text{ injected by each well } \left(\frac{\text{MMSCF}}{\text{D}}\right)} \tag{4.4}$$

From our initial studies in Chapter III, the total CO_2 produced by the eight coal-fired power plants in the vicinity of the Woodbine aquifer with a total generating capacity of 10.4 GW is 3.2 BSCF/day. The injection rate in each well is set to 156 MMSCF/day based on the estimated amount of CO_2 emitted from a 500-MW power plant. The simulation assumes that 100% of the CO_2 produced by the power plants is captured. Therefore from Eq. 4.4, the bulk injection case will require 21 CO_2 injectors. A fracture gradient of 0.71 psi/ft (16.06 kPa/m) was assumed, and the maximum allowable injection pressure is set to 95% of the fracturing pressure at the top of the gridblock that the well is placed. Figure 4.9 shows locations of the CO_2 injectors and coal-fired power plants in the area.

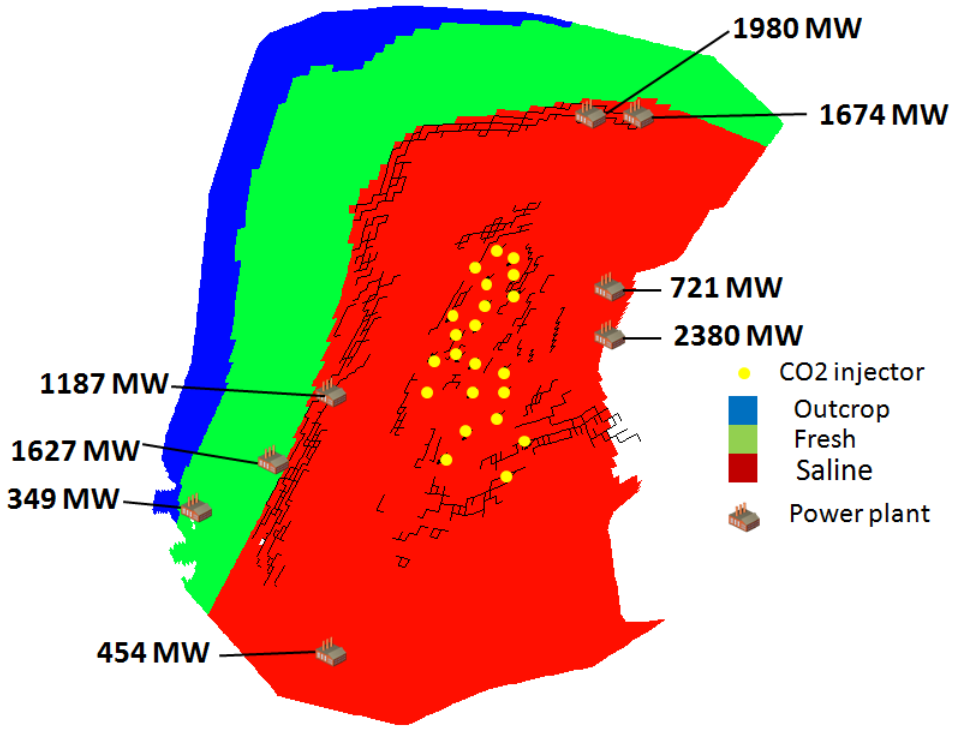

Figure 4.9—Map of Woodbine aquifer showing location of CO_2 injectors.

The duration of injection was set to 20 years. Because of numerical convergence issues, the effect of water vaporization could not be modeled directly. Consequently, the vaporization effect was approximated using a skin of –2.5 in each CO_2 injector based on the conceptual model results discussed in Section 3.2. During the initial constant CO_2 injection simulation runs, it was observed that wells that were located in gridblocks with the same transmissibility range at a greater depth had more injectivity than shallower wells. The reason for this is that deeper wells have a higher maximum allowable bottom-hole pressure which compensates more for injectivity compared to gas viscosity that increases with depth that tends to lower injectivity. Wells that could not inject CO_2 continuously for 20 years because they were close to a fault or close to another CO_2 injector were relocated until all 21 wells were able to achieve the 20-year injection period.

The resulting range in distance between any two wells was from 4.5 to 6 mi, and the closest distance from a well to a mapped fault was 1.3 mi.

4.2.2 Bulk injection

Figures 4.10 and 4.11 show the CO_2 saturation and pressure profiles for 20 years of injection and after 1000 years of monitoring for the base case that assumes all faults are completely sealing. Sensitivity to fault transmissibility will be investigated in Section 4.3.

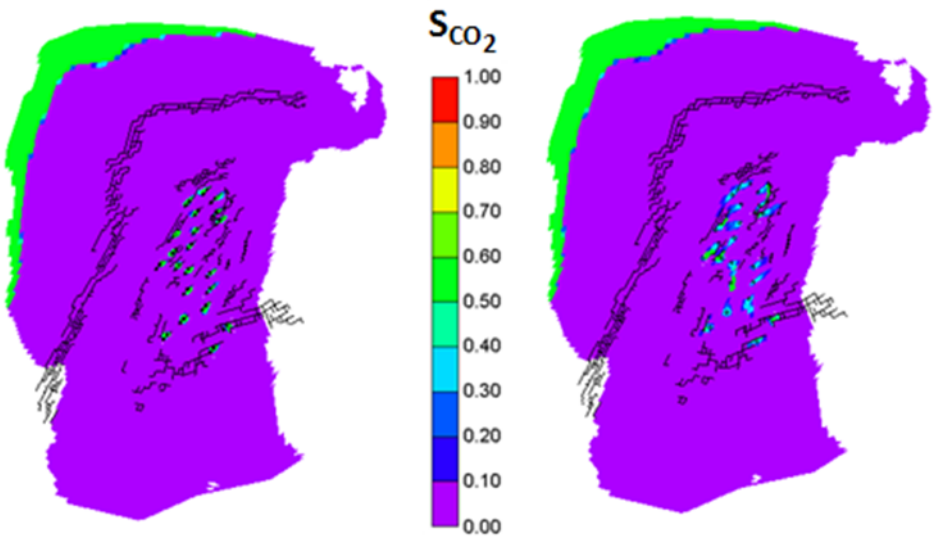

Figure 4.10—CO_2 saturation at the end of 20 years of bulk injection (left) and 1000 years of monitoring.

Figure 4.10 shows that the volume of concentrated CO_2 is dwarfed by the aquifer volume and the CO_2 fronts are close to the injectors. However, Fig. 4.11 shows that the pressure front has propagated to the fault boundaries in the west and north of the injection site. All of the CO_2 injectors were able to inject CO_2 at a constant rate of 4.4×10^6 m^3/day for 20 years and they were able to reach the target injection rate immediately.

After 1000 years of monitoring, the CO_2 front spreads a little further, but does not reach the Mexia-Talco fault system boundary between the fresh and saline aquifers. The CO_2-saturated areas shrink over time because CO_2 in contact with the formation brine is gradually dissolved. Anchliya and Ehlig-Economides (2009) describe a convection current that continually contacts the CO_2 with fresh brine as CO_2 saturated brine sinks due to its slightly greater density. The pressure remains elevated even after 1000 years.

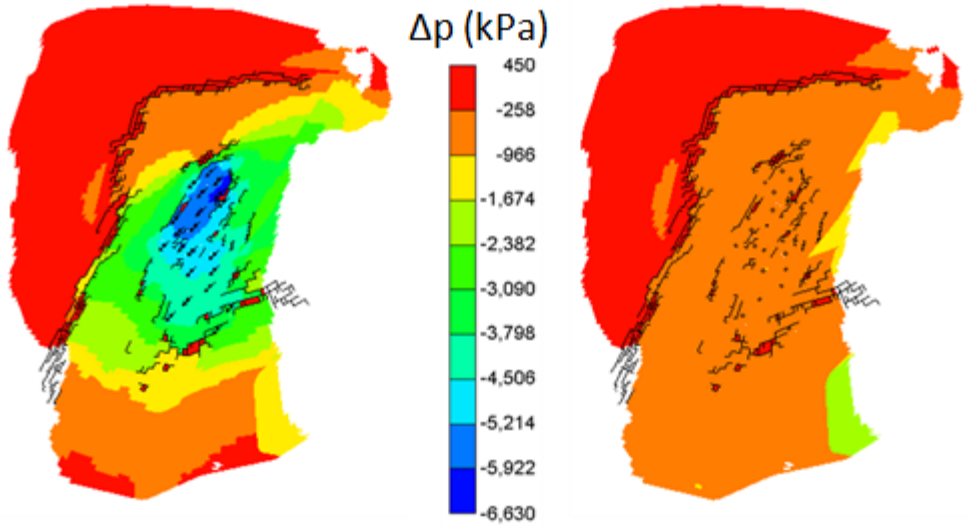

Figure 4.11—CO_2 pressure map at the end of 20 years of bulk injection and 1000 years of monitoring.

4.2.3 CO_2-Brine displacement with external brine disposal

The previous section confirms that bulk CO_2 injection strategy pressurizes the aquifer and therefore limits the amount of CO_2 that can be injected into it. To solve the aquifer pressurization problem, brine can be produced from the aquifer at the same volume at which CO_2 is injected into it.

For this case the well locations for the CO_2 injectors were the same as those of the bulk injection strategy and the brine producers were placed around the injectors in a peripheral pattern. Figure 4.12 shows the locations of the brine producers.

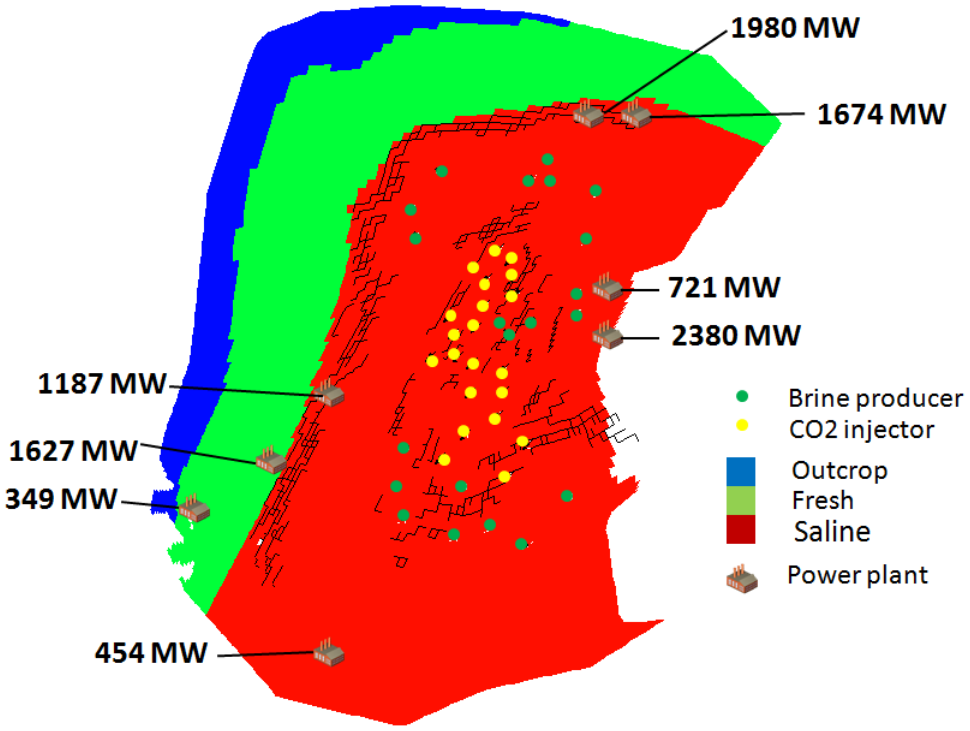

Figure 4.12—Map of Woodbine aquifer showing location of brine producers.

For this aquifer management strategy, there are a total of 42 wells (21 CO_2 injection wells and 21 brine production wells). Each CO_2 injector operates at a constant rate of 4.4×10^6 m^3/day (1.56×10^8 scf/day) using vertical wells perforated at the bottom from the 5^{th} to the 10^{th} layer. The reservoir volume balance between the injected fluid and produced fluid is maintained as in Chapter III. Each brine producer is set to operate at a maximum rate of 14,500 m^3/day (91,200 bbl/day) using a vertical well perforated at the bottom from the 8^{th} to the 10^{th} layer. The distance between an injector and a producer is at least 5 miles.

Using estimates of storage efficiency and breakthrough time calculated in Chapter III, the CO_2 injectors and brine producers are operated 240 years after which breakthrough of CO_2 is expected in the brine production wells. The simulation is continued for another 1000 years to monitor the flow of CO_2 in the aquifer. Figures 4.13 and 4.14 show the CO_2 saturation and pressure profiles after 240 years of injection and after 1000 years of monitoring, respectively.

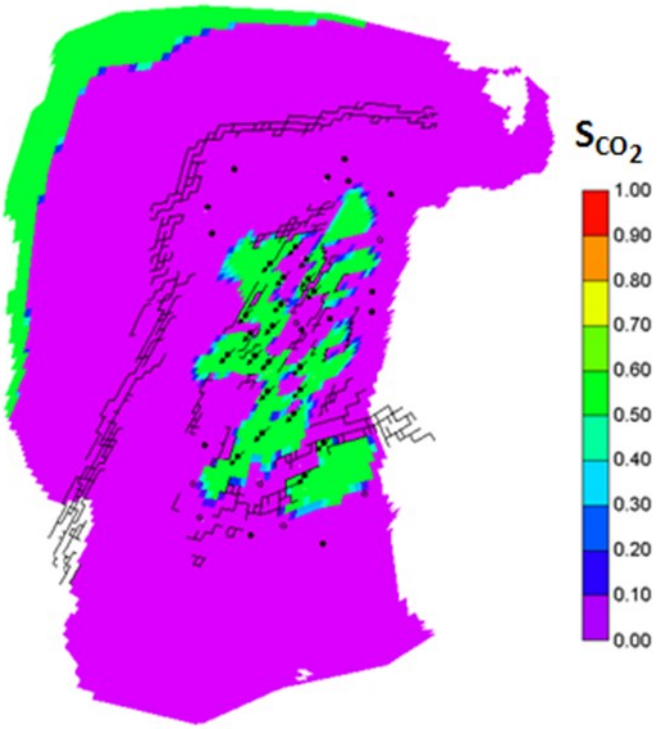

Figure 4.13— CO_2 saturation at the end of 240 years for CO_2-brine displacement with external brine disposal.

With brine production, all of the injection wells can inject CO_2 indefinitely, and the duration of CO_2 injection in the CO_2-brine displacement case is determined by the time of CO_2 breakthrough. In practice, a cutoff for CO_2 breakthrough should be set, e.g., a thousandth of the injection rate. The CO_2-brine displacement with external brine disposal strategy enabled constant rate CO_2 injection at 4.4×10^6 m^3/day for 240 years, which is about 12 times longer than the bulk injection strategy. Figure 4.15 shows the plot of CO_2 breakthrough at producing wells. Trace amounts of CO_2 is seen at some of the producers after 100 years. The maximum production in any well is about 730 m^3/day of CO_2 after 240 years, which is less than one thousandth of the CO_2 injection rate per well. Meanwhile, Figure 4.13 shows that the CO_2 has not reached the Mexia-Talco fault system in the west and north of the injection site after 240 years of CO_2-brine displacement.

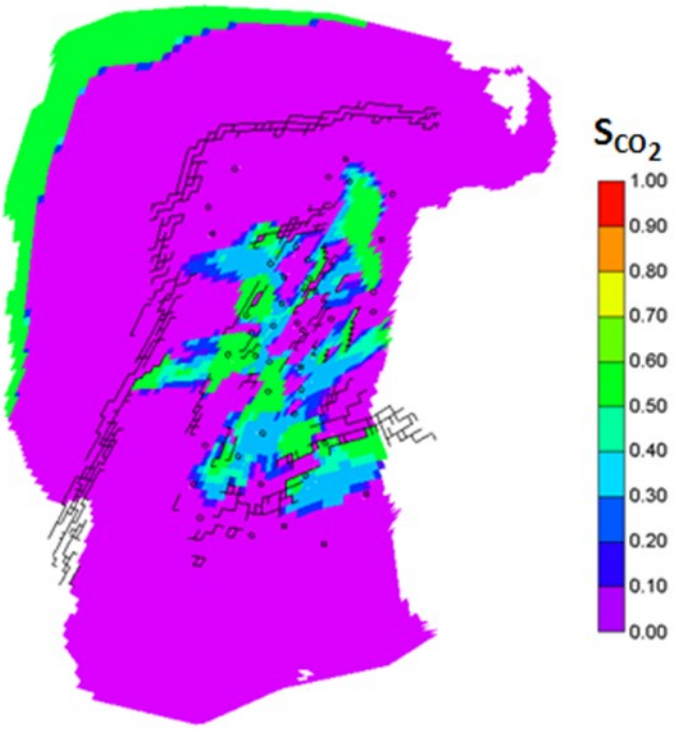

Figure 4.14—CO_2 saturation after 240 years injection and 1000 years monitoring for CO_2-brine displacement with external brine disposal.

After 1000 years of monitoring, the CO_2 plume migrates updip of the aquifer to the west (towards the Mexia-Talco fault zone) and to the eastern boundary of the aquifer. The free CO_2 volume decreases over time because CO_2 dissolves in unsaturated brine circulated by convection currents as in the bulk injection case. The CO_2 volume tends to increase in places where it is structurally trapped by a fault.

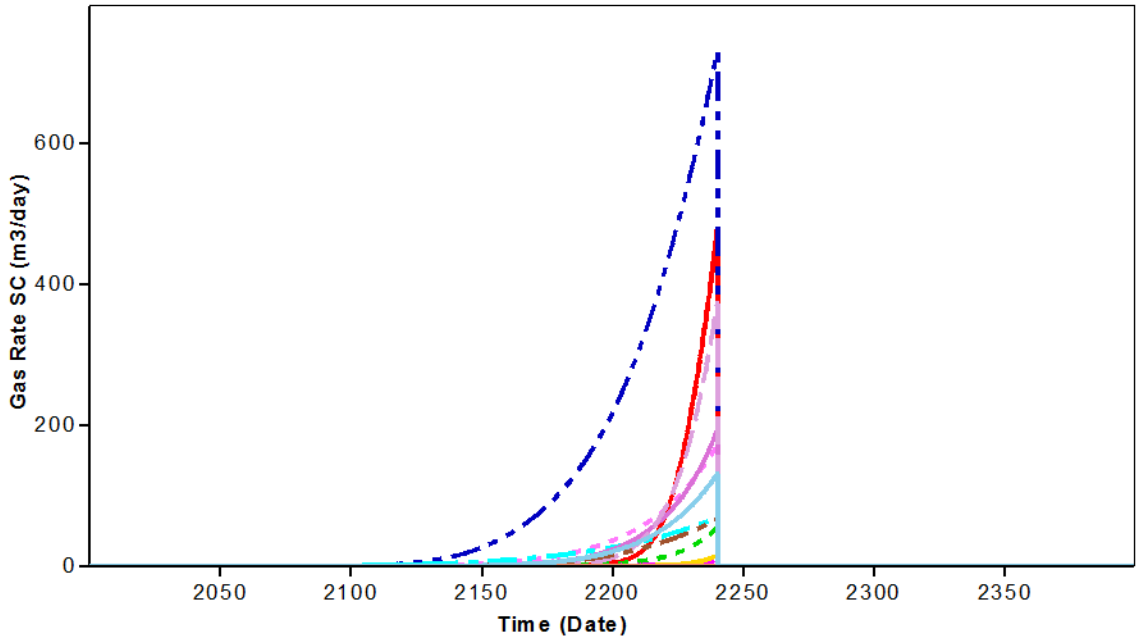

Figure 4.15—Plot of CO_2 breakthrough in brine producers for CO_2-brine displacement with external brine disposal (each color is for a different well).

4.2.4 CO_2-Brine displacement with internal brine injection

As mentioned in Chapter III, the CO_2-brine displacement with external brine disposal turns an aquifer pressurization problem into a brine disposal problem. In the last section, the produced brine might be treated like waste oilfield water to be disposed in deep injection wells. This will increase the project cost as the produced brine has to be stored, transported, and injected into a deep well. It should be noted that the quantity of brine produced dwarfs that commonly to be disposed in oil field operations.

Another way to mitigate aquifer pressurization because of bulk injection is to desalinate the brine produced from the aquifer and re-inject the remaining saturated brine into the same aquifer while maintaining volume balance between injected and produced fluids.

The well locations for the CO_2 injectors and brine producers were the same as those of the external brine disposal strategy. As with CO_2 injectors, formation transmissibility (*kh*) plays an important role on the injectivity of the brine into the formation. Therefore, the brine injectors were placed in regions with high permeability

and net sand thickness, and mostly between CO_2-injectors and brine producers. Figure 4.16 shows the location of the saturated brine injectors.

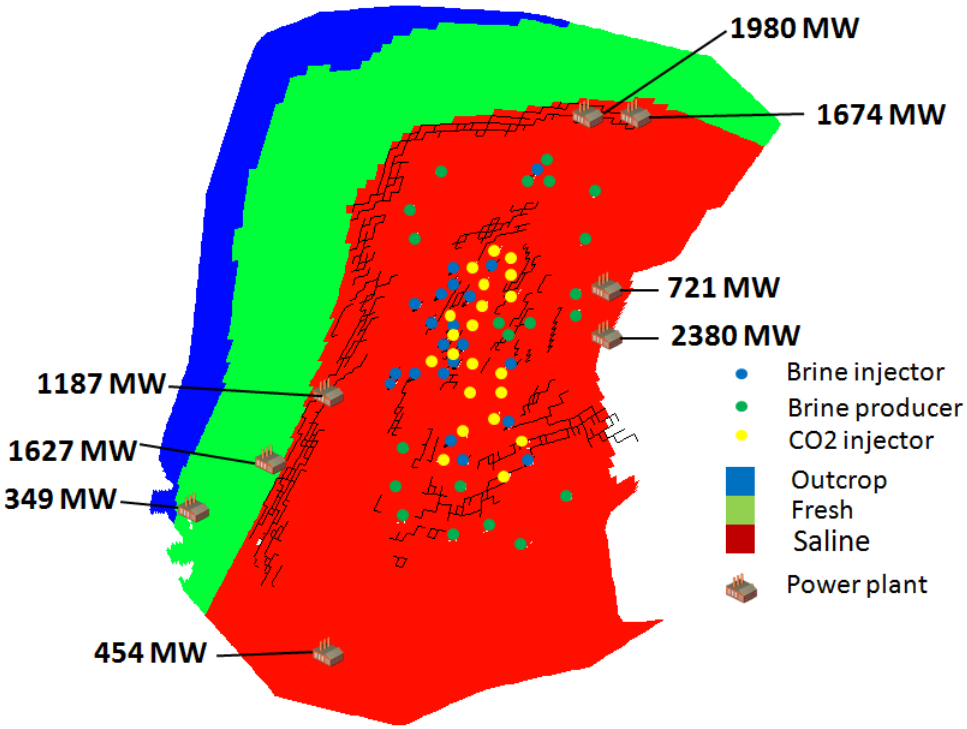

Figure 4.16—Map of Woodbine aquifer showing location of brine injectors.

The injectors and producers are operated for 230 years after which they are shut-in and the simulation is continued for another 1000 years to monitor the behavior of CO_2 in the aquifer.

For this aquifer management strategy, a total of 63 wells were used (21 CO_2 injection wells, 21 brine production wells, and 21 brine injection wells). Each CO_2 injector operates at a constant rate of 4.4×10^6 m^3/day (1.56×10^8 scf/day) using vertical wells perforated at the bottom from the 5^{th} to the 10^{th} layer. Each brine producer is set to operate at a maximum rate of 19,000 m^3/day (120,000 bbl/day) using vertical wells perforated at the bottom from the 8^{th} to the 10^{th} layer. The saturated brine injectors are set to operate at a constant rate of 2575 m^3/day (16,200 bbl/day) using a vertical well perforated at the bottom from the 8^{th} to the 10^{th} layer.

Figures 4.17 and 4.18 shows the CO_2 saturation and pressure profiles after 230 years of injection and after 1000 years of monitoring respectively, whereas Figure 4.19 shows the plot of CO_2 breakthrough at the producers.

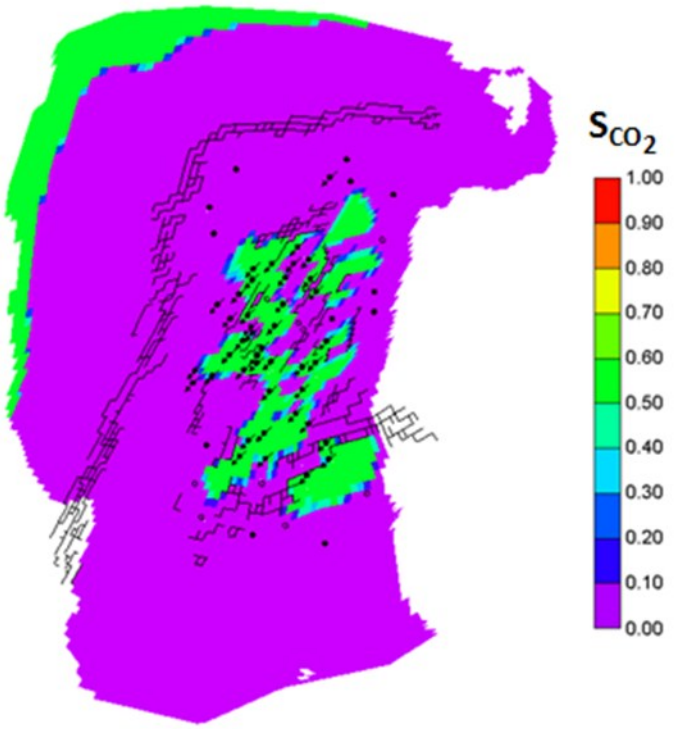

Figure 4.17—CO_2 saturation at the end of 230 years for CO_2-brine displacement with internal brine injection.

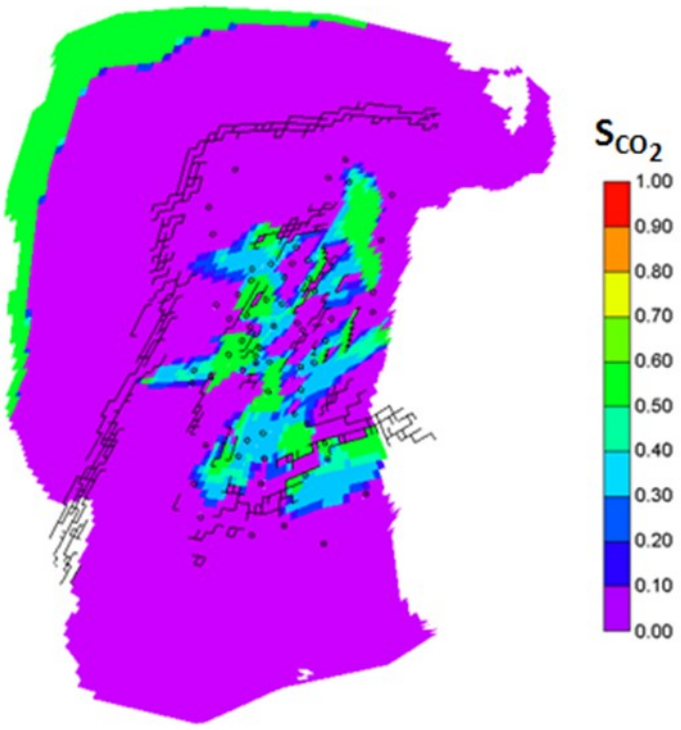

Figure 4.18—CO_2 saturation after 230 years injection and 1000 years monitoring for CO_2-brine displacement with external brine disposal.

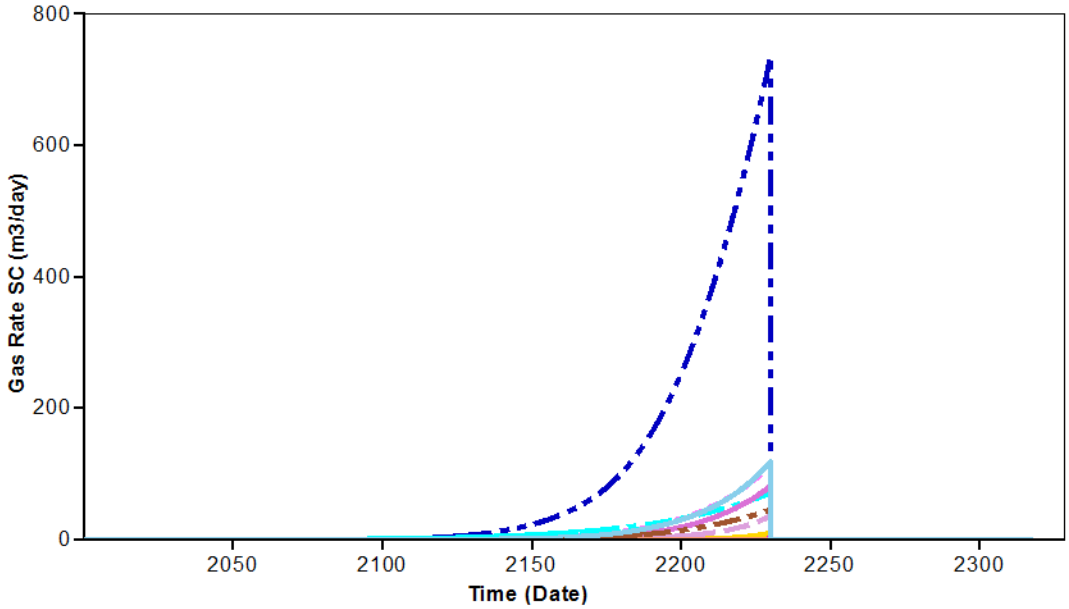

Figure 4.19—Plot of CO_2 breakthrough in brine producers for CO_2-brine displacement with internal brine injection (each color is for a different well).

4.3 Impact of Fault Transmissibility

In this section, the possibility that native brine from the more saline region (in the injection site) may flow into the less saline region updip across the Mexia-Talco fault system is investigated.

The major faults in the Mexia-Talco fault system frequently exhibit hundreds of feet of displacement, effectively juxtaposing vertically distinct hydrostatic units. The relative insolubility of Woodbine sediments leads to a smearing of materials in the fault zone, and prevents significant dissolution of fault-zone materials. Therefore, little or no vertical or horizontal flow is expected (R.W. Harden & Associates Inc. 2004), and the fault system likely forms an effective seal between the fresh and saline water regions that could explain the observed salinity contrast between them.

In this study, a rather simplistic approach of varying the transmissibility across the fault to investigate the flux across the fault at varying transmissibility is adopted. Using this method, an upper and lower bound on the potential for flow of brine into the fresh water part of the aquifer as a result of a CO_2 storage project is achieved. Following are sensitivity analyses for each for each of the aquifer management systems considered.

4.3.1 Bulk injection

Figure 4.20 shows a normalized plot of the water volume leaving from the highly saline part of the aquifer into the less saline part of the aquifer with transmissibility varying from 0 to 1 for the bulk injection case. This plot is generated by calculating the cumulative native brine leaving the sector at reservoir conditions and dividing it by the cumulative CO_2 injected at reservoir conditions.

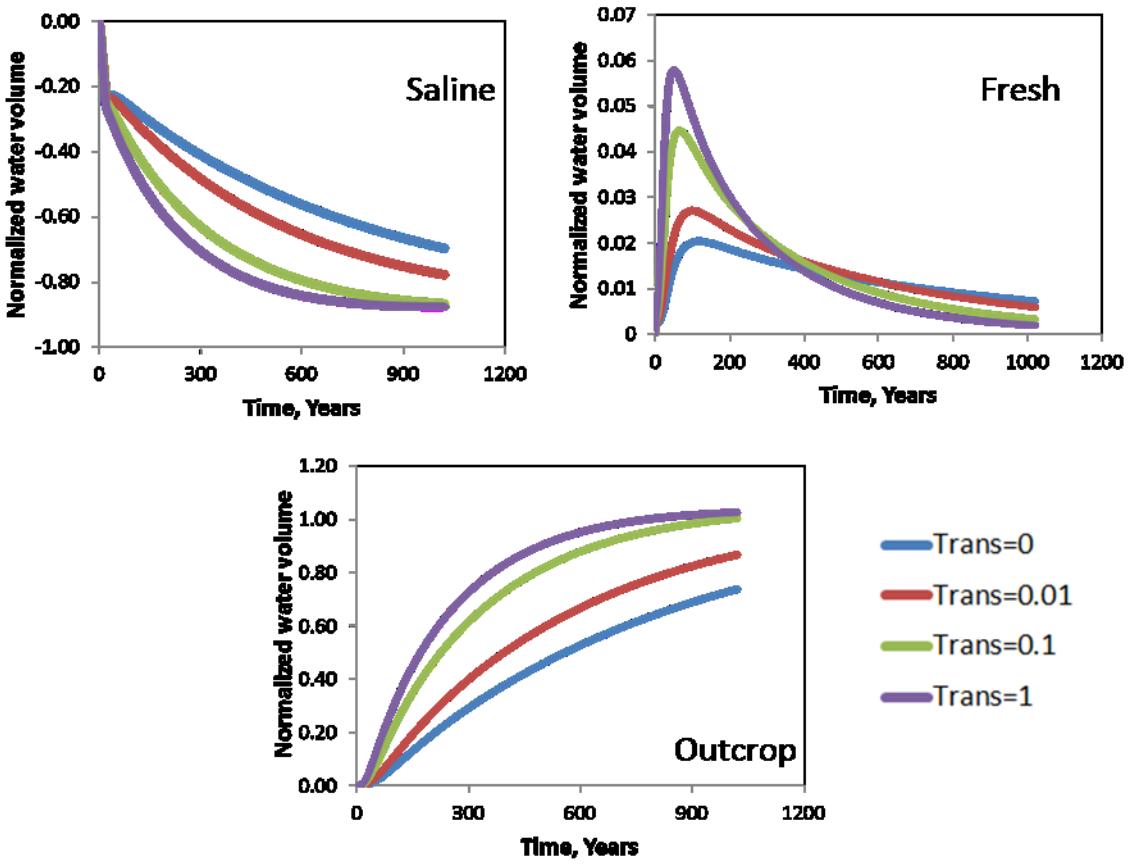

Figure 4.20—CO_2 bulk injection normalized water volume plot for three sectors showing the effect of varying fault transmissibility.

As mentioned earlier in this chapter, when CO_2 is injected in the downdip portion of the saline region it displaces brine towards the updip portion of the fresh region. To estimate the volumes of fluids moving across leaky faults, the transmissibility of the geologic faults are varied from 0 to 1.

From Figure 4.20 it can be seen that for the case of a system of sealing faults (*Trans* = 0) the volume of native brine displaced out of the brine region is about 22% of the total injected CO_2 volume during the 20 years of injection and 65% after 1000 years of monitoring.

Varying the fault transmissibility from 0.01 to 1 increases the brine displacement. Figure 4.20 shows that the change in normalized water volume in the saline region is greater when transmissibility is varied between 0 and 0.01. This means that a brine volume equal to most of the total injected CO_2 volume will move up-dip through the

geologic fault at low transmissibility values and even more brine will leave the region at higher transmissibility values.

In the fresh water regions, Fig. 4.20 shows that there is an initial increase in brine volume of up to 6% of its initial volume as CO_2 displaces brine to the fresh water region. This is followed by a reduction in brine volume, after 45 years for sealing fault and after 100 years for completely leaky fault, as brine is further being displaced to the outcrop. At the end of 1000 years monitoring, more water is displaced from the fresh water region for a completely leaky fault (*Trans* = 1).

In the outcrop, Fig. 4.20 shows that ultimately, CO_2 displaces brine to the outcrop. After 1000 years of monitoring, about 65% of the CO_2 injected has been displaced as brine for a sealing fault while 100% of the CO_2 injected has been displaced as brine for a leaky fault. This indicates that perfect displacement is realized in the case of a leaky fault.

Figures depicting the changes in CO_2 saturation and pressure changes before injection, after injectors are shut-in, and after 1000 years of monitoring are shown in Appendix A and reviewed next.

The outcrop region shows gas saturation that actually represents air, not CO_2.

The CO_2 injectors are shut after a period of 20 years of CO_2 injection and it can be seen from Figure A-1.2 that in all cases that the CO_2 plumes are close to the CO_2 injectors and the effective CO_2 saturation is local and does not spread out. It can be seen from Figure A-1.3 and A-1.4 that relatively little spread in CO_2 saturation occurs during and after the monitoring period. The CO_2-saturated area of the aquifer shrinks with time because of dissolution of CO_2 in formation brine.

The pressure change maps in Appendix A2 show the changes from the initial pressure and the pressure at another time. A negative pressure change indicates that the system is being pressurized whereas a positive pressure change indicates depressurization. Looking at the time slice in pressure changes in the system, Figure A-2.2 shows that although the CO_2 saturation effect is only local to the wells after 20 years of injection, the aquifer has effectively pressurized toward the boundary between the saline and fresh water regions. The extent of change in the pressure scale depends on the transmissibility of the fault. The case with fault transmissibility of zero pressurized more than cases with nonzero fault transmissibility because the aquifer volume is effectively

limited to the saline aquifer region when brine cannot flow across the fault. During the monitoring period, it is evident that the aquifer is equilibrating and the pressure is reducing back to its original value. The rate at which the aquifer equilibrates depends on the fault transmissibility. Higher fault transmissibility means faster pressure equilibration.

The average pressure plots in Fig. 4.21 show increases in average pressure for all the three aquifer regions during the CO_2 injection period. Once the CO_2 injectors are shut, the average pressure begins to decline. Looking at the average pressure plot for the Saline sector, the system that pressurizes the most during CO_2 injection and monitoring is that with completely sealing faults.

For the Fresh and Outcrop region, the average pressure of the completely leaky fault increases the most and also equilibrates fastest during the monitoring period. It should be noted that there is a lag in the peak average pressure amongst the three regions. This results because of the time taken for the fresh and outcrop region to respond to the effect of the displaced brine.

Pressure equilibration in the outcrop region corresponds to fresh water production either through springs or as water vapor.

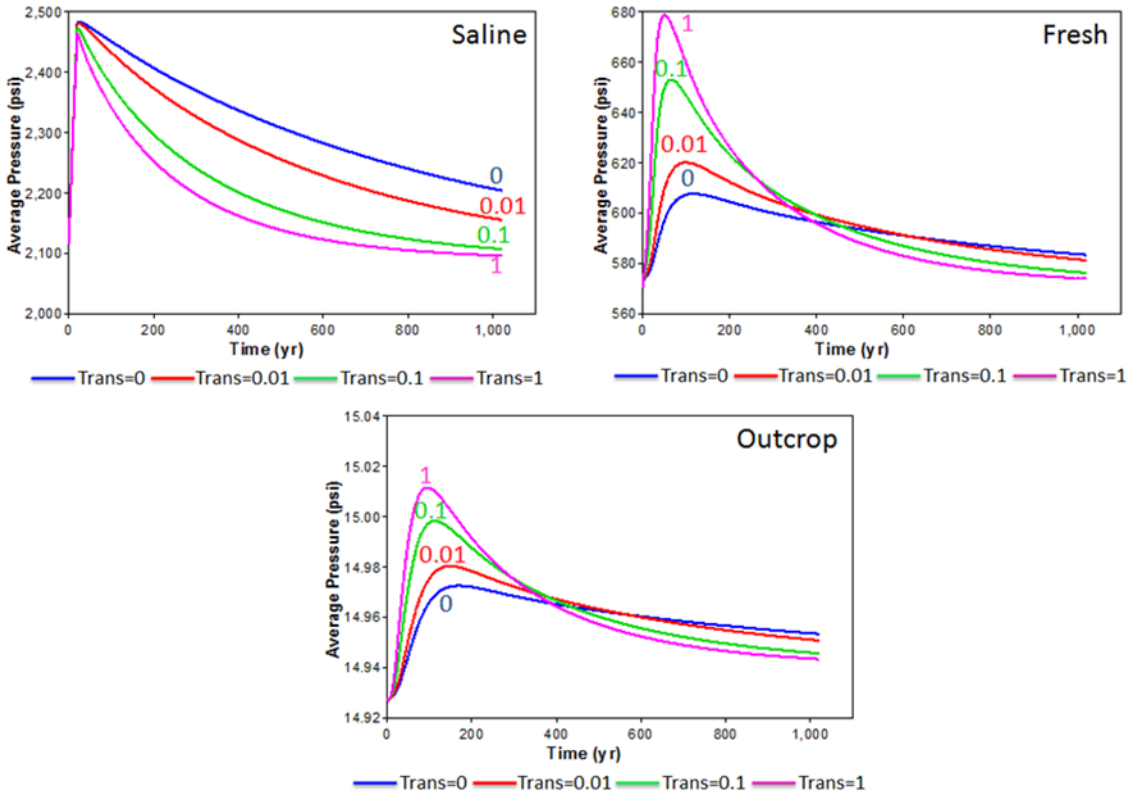

Figure 4.21—Average pressure plots for CO_2 bulk injection for three sectors showing the effect of varying fault transmissibility.

4.3.2 CO_2-Brine displacement

The CO_2-brine displacement strategies can continue for up to 240 years. There is a considerable spread in CO_2 saturation after the end of CO_2 injection and brine production. The CO_2 saturation maps at the end of CO_2 injection and brine production shows little difference in CO_2 saturation fronts for varying fault transmissibility (Figures A-3.2 and A-5.2). This is because the flow part of fluids is altered by varying the transmissibility of the fault. CO_2 saturation gets to the boundary of the major fault system after a monitoring period of 800 years (Figures A-3.3 and A-5.3).

The case with fault transmissibility of 0.1 and 1 indicate that CO_2 is leaking into the fresh water region after 1000 years of monitoring for the external brine disposal strategy as seen in Figure A-3.4. However, CO_2 leaks into the fresh water region after

1000 years of monitoring for only case with fault transmissibility of 1 for the internal saturated brine injection strategy (Figure A-5.4).

The initial pressure changes in the system at the beginning of the project for the external brine disposal case (Figure A-4.1). There is regional pressurization close to the CO_2 injectors and depressurization close to the brine producers before the injectors and producers are shut-in. Regional pressurization is mostly pronounced for the case of fault transmissibility equal zero. After 240 years of operation, there is limited pressure changes in the fresh and outcrop region (to the left of the Mexia-Talco fault system) for all fault transmissibilities. This is as a result of the brine producers dissipating a similar magnitude of pressure generated by CO_2 injection. The system is shut-in after 240 years and it starts to equilibrate. Very much like the bulk injection strategy, the aquifer pressure equilibrates fastest for the case of fault transmissibility equal one after 500 years and 1000 years of monitoring as seen in Figures A-4.3 and A-4.4, respectively.

The pressure change at the beginning of the project for the internal saturated brine injection case is shown in Figure A-6.1. Similar to the external brine disposal case, there is regional pressurization close to the CO_2 and brine injectors, and depressurization close to the brine producers before the injectors and producers are shut-in. However, there are some pressure changes to the left of the Mexia-Talco fault system after 230 years (shut-in time). This pressure changes are more evident for fault transmissibility of 0.1 and 1 as seen in Figure A-6.2. The system starts to equilibrate once it is shut-in. Similar to the previously mentioned aquifer management strategies, the aquifer pressure equilibrates fastest for the case of fault transmissibility equal one after 500 years and 1000 years of monitoring as seen in Figures A-6.3 and A-6.4, respectively.

There is a sudden rise in average pressure immediately after the injectors and producers are shut-in, then the aquifer starts to equilibrate as seen in Figures 4.22 and 4.23. According to Bob Brugman, 'the injected gaseous CO_2 migrates to the structurally higher parts of the reservoir whereas brine with CO_2 dissolved in it (and therefore heavier) moves to the structurally lower parts of the reservoir. After the injectors are shut-in, the pressure gradient around the injectors are reversed causing the distribution of fluids in such a way that an increase in the average (pore volume weighted) reservoir

pressure was noticed. In other words, the effect of convective currents caused by movement of fluids with varying densities is observed.'[1]

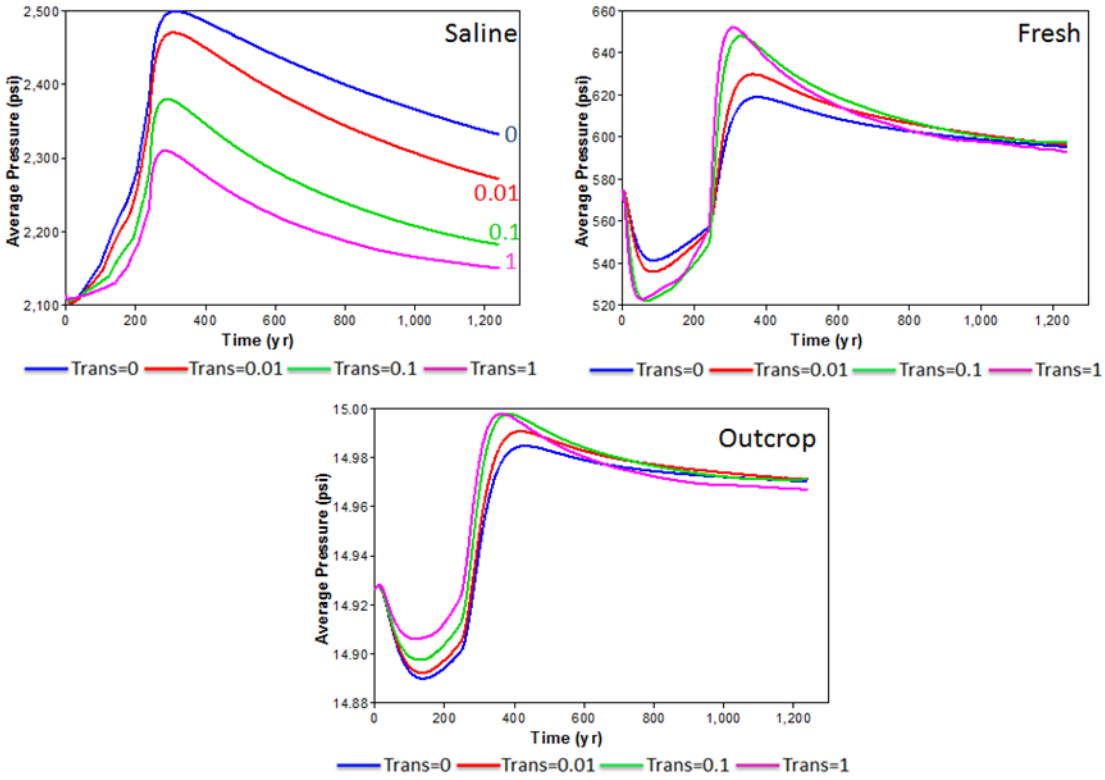

Figure 4.22—Average pressure plot for CO_2-brine displacement with external brine disposal for three sectors showing varying fault transmissibility.

There is an increase in pressure during fluid injection and brine production in the saline region as seen in Figures 4.22 and 4.23. This is partly caused by the differences in compressibilities of the injected and produced fluids and also results because some brine producers were shut down before actual shut-in time because they had produced a maximum limit of 800 m^3/day of CO_2. The initial reduction in pressure in the fresh and outcrop region is most likely due to the placement of the brine producers closer to these regions. Therefore, the fresh and outcrop regions encounters the effect of pressure reduction because of brine production before they encounter the effect of pressure increase from the CO_2 injectors placed farther away.

[1]Bob Brugman, 25 May 2012, Personal Communication (email)

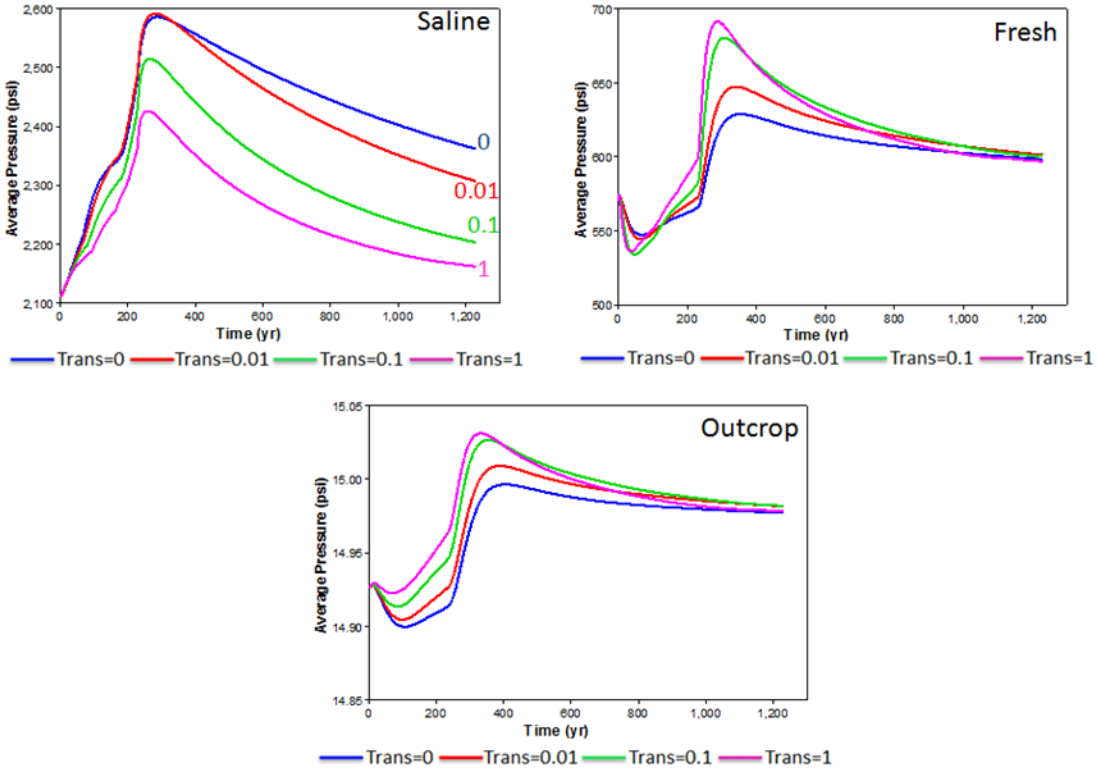

Figure 4.23—Average pressure plot for CO_2-brine displacement with internal saturated brine reinjection for three sectors showing varying fault transmissibility.

The normalized volume of CO_2 displaced as brine for the external brine disposal case and saturated brine injection case are shown in Figures 4.24 and 4.25, respectively. In both cases, it can be seen that about 85% of the injected CO_2 has been produced as brine from the saline region before the system is shut-in. Furthermore, another 10% of the injected CO_2 volume has migrated in the form of brine from the saline region to the fresh region and ultimately to the outcrop.

The dip in normalized water volume in the fresh region for case of fault transmissibility of 0.1 and 1 for the external brine disposal strategy (Figure 4.24) and case of fault transmissibility of 1 for the internal saturated brine injection strategy (Figure 4.25) is caused by the leakage of CO_2 into the fresh region in these cases.

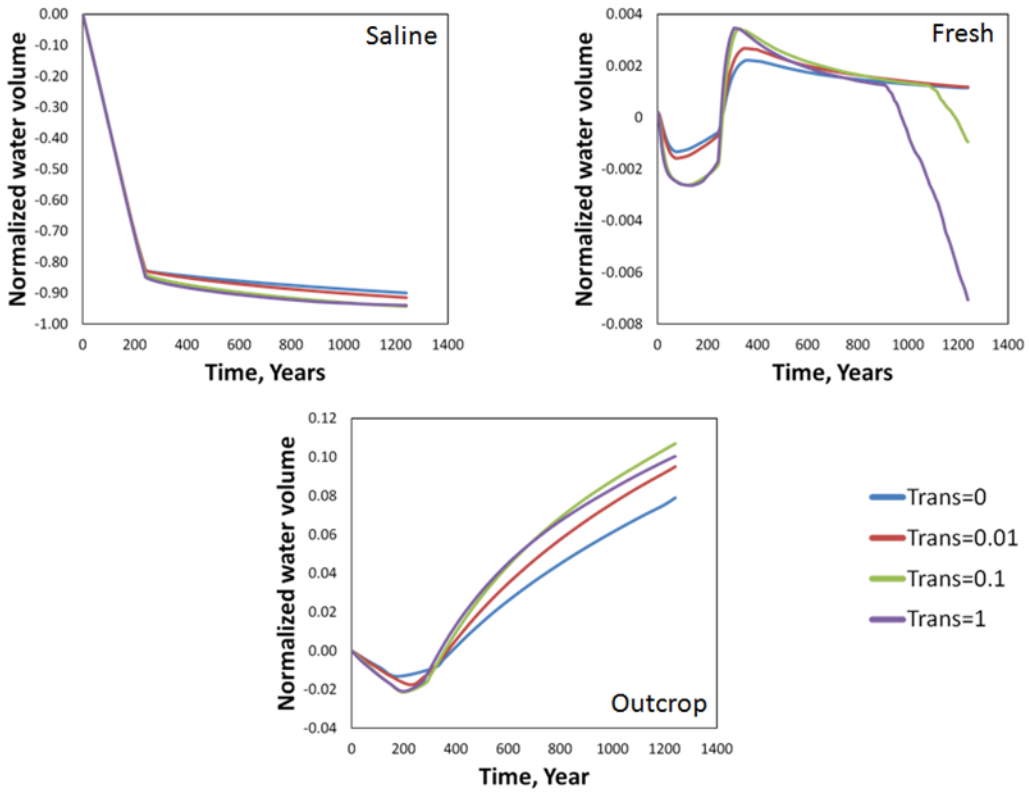

Figure 4.24—CO_2-brine displacement with external brine disposal normalized water volume plot for three sectors showing varying fault transmissibility.

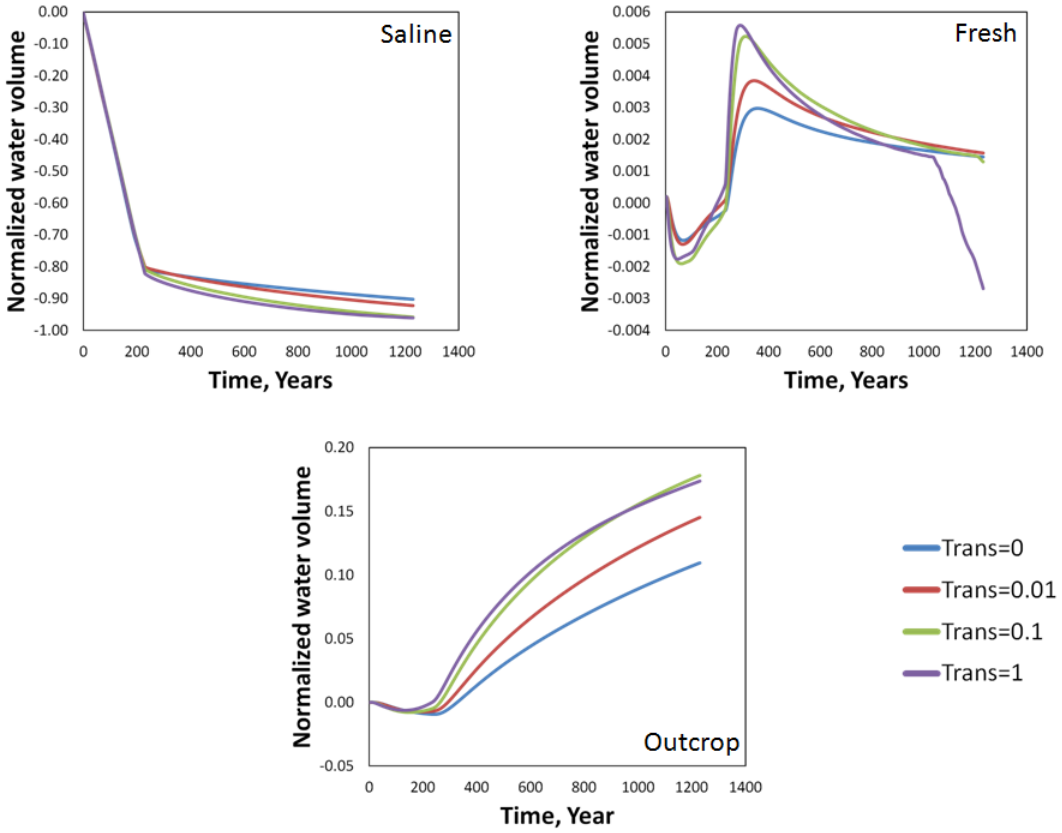

Figure 4.25—CO_2-Brine displacement with internal saturated brine reinjection normalized water volume plot for three sectors showing varying fault transmissibility.

4.4 Effect of Geochemical Reactions

When CO_2 is injected into an aquifer, a weak acid is formed which will readily dissociate:

$$H_2CO_3 \xrightarrow{\text{yields}} H^+ + HCO_3^-$$

This causes acidification and carbonation of the native brine. Also, the changes in aqueous composition can cause dissolution and precipitation of minerals. In this subsection, a sub model of the geological model shown in Figure 4.26 was used to study the effect of geochemical reactions in the Woodbine aquifer.

Possible chemical reactions include those between mineral and aqueous components and those between components in the aqueous phase. The components in the aqueous phase contain gaseous components that are soluble in the aqueous phase as well

as components that exist only in the aqueous phase. The rate of reaction for mineral dissolution and precipitation reaction is (Nghiem et al):

$$r_\beta = k_\beta \hat{A}_\beta \left(1 - \frac{Q_\beta}{K_{eq,\beta}}\right) \tag{4.5}$$

and the rate constants follow an Arrhenius dependence on temperature:

$$k_\beta = {k_\beta}^0 \exp\left[-\frac{E_{a\beta}}{R}\left(\frac{1}{T} - \frac{1}{T_0}\right)\right] \tag{4.6}$$

Figure 4.26—A sub model of the Woodbine aquifer (bulk injection).

Minerals found in the Woodbine aquifer are quartz, kaolinite, K-feldspar, and chamosite. The geochemical reactions for the Woodbine are shown in Table 4.1 and the values of the mineral reaction parameters are shown in Table 4.2.

For this simulation study, bulk injection of 3 million tonnes per year of CO_2 is injected into a portion of the woodbine aquifer for a period of 30 years and monitored for 1000 years. The most common mineral found in the Woodbine is quartz whereas the least common is K-feldspar. Therefore, the initial volume fraction assumed for this simulation is shown in Table 4.3.

Table 4.1—Geochemical reactions

Aqueous Reactions
1. $CO_{2(aq)} + H_2O \leftrightarrow H^+ + HCO_3^-$
2. $HCO_3^- + H^+ \leftrightarrow 2H^+ + CO_3^{2-}$
3. $H_2O \leftrightarrow H^+ + OH^-$
Mineral dissolution/precipitation reactions
4. $\text{Chamosite} + 10H^+ \leftrightarrow 2Fe^{2+} + SiO_{2(aq)} + 2Al^{2+} + 7H_2O$
5. $\text{K} - \text{Feldspar} + 4H^+ \leftrightarrow 2H_2O + K^+ + Al^{3+} + 3SiO_{2(aq)}$
6. $\text{Kaolinite} + 6H^+ \leftrightarrow 5H_2O + 2Al^{3+} + 2SiO_{2(aq)}$
7. $\text{Quartz} \leftrightarrow SiO_{2(aq)}$

Table 4.2—Mineral reactions

Mineral	$\log_{10}K_\beta$ (mol/m^{2}s)	A_β (m^2/m^3)	$E_{a\beta}$ (J/mol)	Initial volume fraction
Chamosite	–11.0	88	60,000	0.0088
K-feldspar	–12.1	11	26,400	0.0011
Kaolinite	–13.0	88	62,760	0.0088
Quartz	–13.0	792	74,500	0.0792

Figure 4.27 shows that there is precipitation of kaolinite from the beginning of CO_2 injection while K-feldspar is being dissolved. Quartz is initially being dissolved, but starts to precipitate after 288 years. Chamosite dissolves for 22 years after which it starts to gradually precipitate. There is a sharp increase in chamosite precipitation after 200

years. Mineral precipitation might lead to pore clogging followed by loss of injectivity, whereas mineral dissolution can lead to increase in porosity and subsequently increase in injectivity. During the 30-year injection period considered, the amount of dissolved CO_2 is higher for simulation with geochemistry compared to simulation without geochemistry.

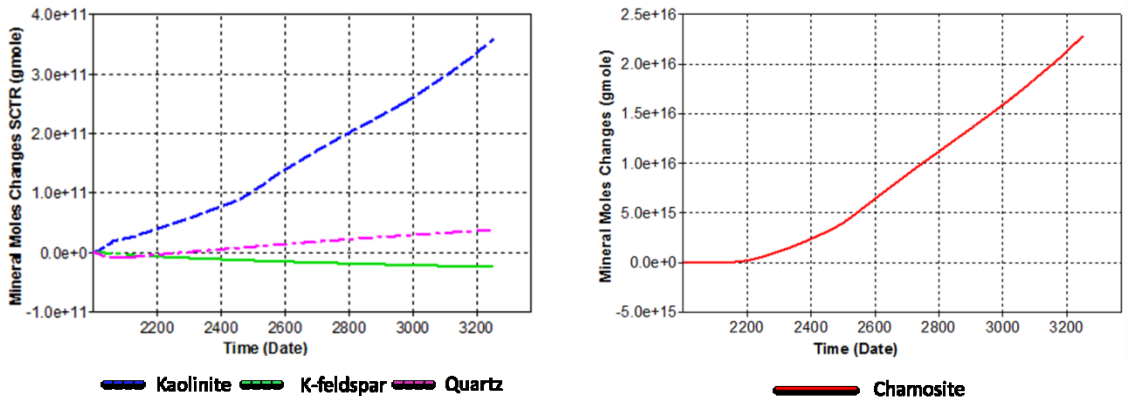

Figure 4.27—Changes in mineral moles without calcite.

Table 4.3: Initial concentration of aqueous components for geochemical case

Aqueous Species	Concentration (mol/kg H_2O)
H^+	1.00×10^{-7}
Fe^{2+}	3.22×10^{-11}
$SiO_2(aq)$	2.34×10^{-8}
Al^{3+}	2.32×10^{-11}
K^+	9.12×10^{-5}
OH^-	1.41×10^{-6}
HCO_3^-	1.00×10^{-3}
CO_3^{2-}	6.98×10^{-7}

Another simulation was performed to see the effect of adding calcite to the list of minerals found in the Woodbine aquifer. The reaction and data used for calcite are as follows:

$$\text{Calcite} + (H^+) = Ca^{2+} + HCO_3^-$$

A_β= 44 m^2/m^3; E_A=41,870 J/mol; initial volume fraction = 0.0044

The result of the simulation shown in Figures 4.28 and 4.29 shows that calcite and K-Feldspar are being dissolved throughout the injection and monitoring period, whereas quartz is initially being dissolved, but starts to precipitate after 315 years. There is a precipitation of kaolinite and chamosite from the beginning of CO_2 injection. Figure 4.29 shows that there is a sharp increase in chamosite precipitation after 70 years. It can be concluded that the presence of calcite in the formation would slightly reduce chamosite precipitation and increase the precipitation of kaolinite.

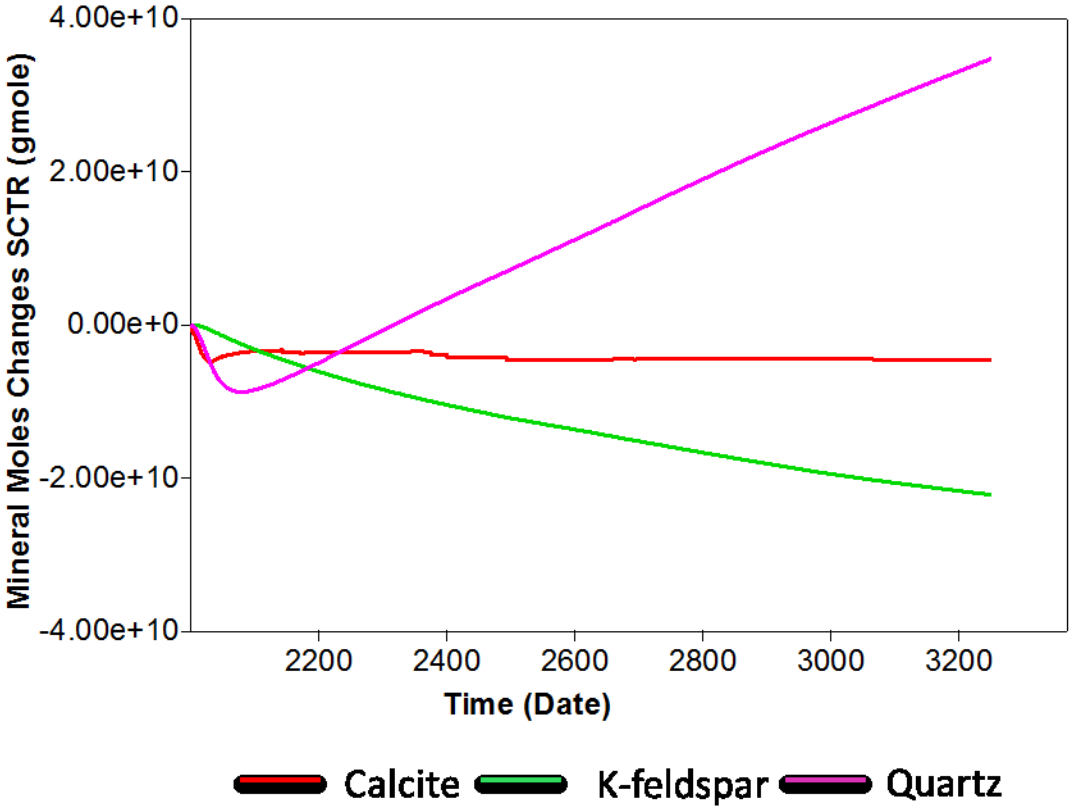

Figure 4.28—Changes in mineral moles for calcite, K-feldspar, and quartz.

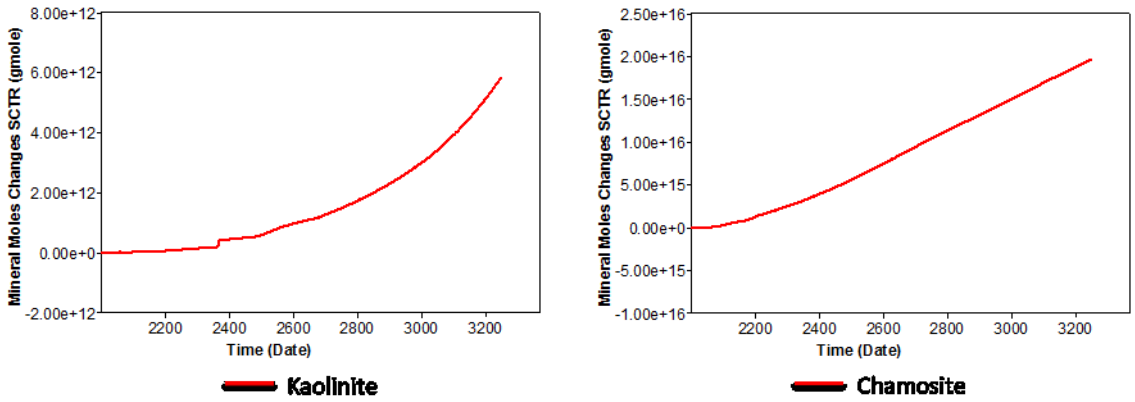

Figure 4.29—Changes in mineral moles for kaolinite and chamosite.

4.5 Effect of Impurities in the CO_2-rich Stream

Inevitably, there will be some impurities in the CO_2-rich stream after it has been separated. The purpose of this subsection is to analyze the effect of these impurities on CO_2 sequestration.

The likely composition of the impurities is listed in Table 2.3. The reactions caused by the presence of these impurities are shown in Table 4.4 whereas the initial concentration of aqueous components used in the simulation is shown in Table 4.5.

Table 4.4—Reactions due to presence of impurities

1. $CO_{2(aq)} + H_2O \leftrightarrow H^+ + HCO_3^-$
2. $CO_3^{2-} + H^+ \leftrightarrow HCO_3^-$
3. $HSO_4^- \leftrightarrow SO_4^- + H^+$
4. $H^+ + OH^- \leftrightarrow H_2O$
5. $H_2SO_4 \leftrightarrow 2H^+ + SO_4^{2-}$
6. $HNO_3 \leftrightarrow H^+ + NO_3^-$

Table 4.5—Initial concentration of aqueous component for impurity case

Aqueous Species	Concentration (mol/kg H_2O)
H^+	1.00×10^{-7}
SO_4^{2-}	9.12×10^{-7}
NO_3^-	5.00×10^{-8}
HCO_3^-	5.00×10^{-4}
CO_3^{2-}	3.36×10^{-7}
OH^-	1.30×10^{-6}
HSO_4^-	3.28×10^{-11}

Similar to the geochemical case, a sub model of the Woodbine aquifer is used for this analysis. Bulk injection of 3 million tonnes per year of rich CO_2 with impurities is injected into the Woodbine aquifer for a period of 30 years and monitored for 100 years. Figure 4.30 shows the pH in a cross section of the model after 30 years injection and after 100 years.

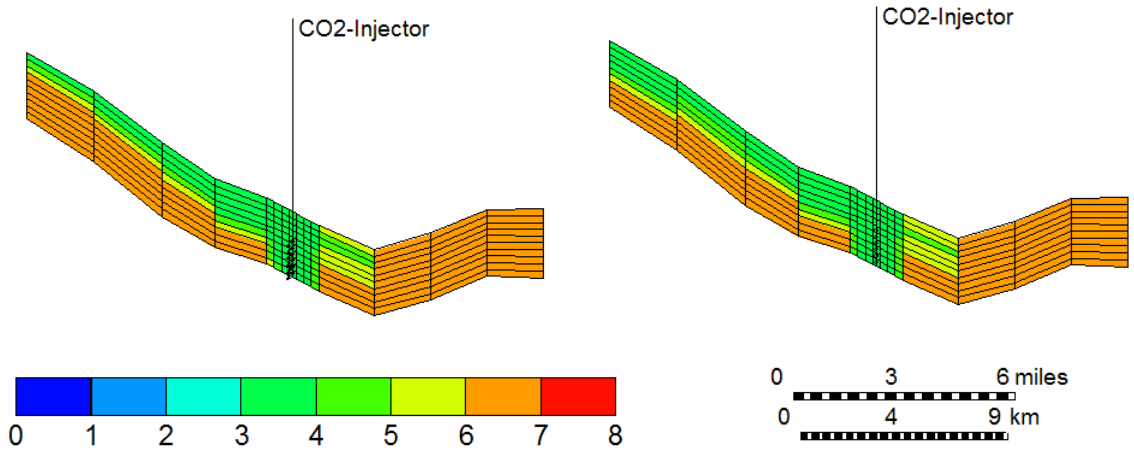

Figure 4.30—pH of Woodbine aquifer after 30 years (left) and 100 years (right) of bulk injection (impure case).

As the CO_2-rich gas is injected into the formation, the pH of the formation changes from the initial value of 7 to as low as 3.3. Grid blocks with higher CO_2 saturation, close to the injector and the top of the formation, have a lower pH. When a pure CO_2 stream is injected into the formation, the pH of the formation changes from 7 to

as low as 4.8 as shown in Figure 4.31. Therefore, the presence of impurities in the CO_2-rich gas lowers the pH of the formation from about 4.8 to 3.3.

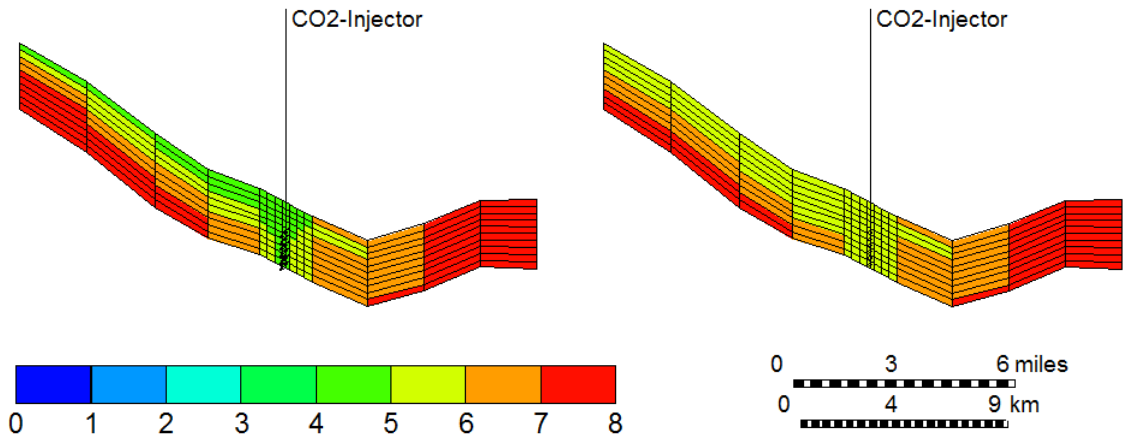

Figure 4.31—pH of Woodbine aquifer after 30 years (left) and 100 years (right) of bulk injection (pure case).

The percentage changes in the aqueous components are shown in Table 4.6

Table 4.6—Percentage change in aqueous specie concentration for impurity case

Aqueous Species	Percentage change (%)		
	Initial (0 year)	30 years	100 years
H^+	0	8400	10,296
SO_4^{2-}	0	3.4	4.1
NO_3^-	0	–0.4	–0.6
HCO_3^-	0	1.6	2
CO_3^{2-}	0	–12.5	–14.3
OH^-	0	–5.38	–7.69
HSO_4^-	0	6790	8345

There is significant increase in aqueous concentration of H^+ and HSO_4^-after 30 years of injection and 100 years of monitoring. These increase causes brine acidification, which could affect the integrity of the production lines. Production tubing made of carbon

steel is susceptible to corrosion and more expensive tubing made with chromium alloy will be needed.

4.6 Chapter Conclusions

This chapter describes the creation of a geological model used for the full-field simulation and fluid modeling of CO_2 sequestration in the Woodbine aquifer.

The structural properties were created by using contour maps such as depth map (formation tops), formation thickness map (formation bottoms), net sand thickness map, and a fault map. The petrophysical properties were populated using Sequential Gaussian Simulation conditioned by sparse permeability and porosity data.

The geologic model depicts the complexities found in the Woodbine aquifer showing numerous structural highs and lows caused by the presence of salt domes in the formation. The model is divided into three regions: (1) the outcrop which is up dip to the northwest and is above the sea-level, (2) the fresh water region, and (3) the saline region which is down dip to the southeast and is the sequestration zone.

The claim made in Chapter III is validated, i.e., the Woodbine aquifer can only inject CO_2 for 20 years using bulk injection strategy due to aquifer pressurization and that a CO_2-brine displacement strategy would store CO_2 for up to 240 years.

Results show that CO_2 would leak into the fresh water aquifer during the monitoring period of 1000 years for cases if fault transmissibility is not zero. For high fault transmissibility, there is the possibility of CO_2 leaking into the fresh water aquifer. Because fault displacements are typically more than 700 ft, and because there is a sharp contrast in salinity across the Mexia-Talco fault system, the likelihood of nonzero fault transmissibility may be low and may remain low provided that neither increased nor decreased pressure across the fault system from CO_2 and saturated brine injection or brine production alter the fault transmissibility over time.

The presence of impurities in the CO_2 stream reduces the pH of the formation during CO_2 injection to 3.3, compared to 4.8 with a pure CO_2 stream. Reduction in pH would cause brine to be more corrosive and render carbon steel production tubing inappropriate. More expensive tubing made of chromium alloy will be needed.

Including the effects of geochemical reactions results in the mineral precipitation of kaolinite, quartz, and chamosite, and the dissolution of K-feldspar. Similarly, the addition of calcite as a mineral present in the formation leads to a mineral precipitation of kaolinite, quartz, and chamosite, and a dissolution of K-feldspar and calcite.

The storage of a large amount of CO_2 in geological formation will have huge imprints in terms of surface and pipeline facilities required and the increase in storage efficiency in the CO_2-brine displacement strategy compared to the bulk injection strategy comes at an increased project cost. The next chapter will estimate the energy requirements and environmental impacts that such a project could have by considering pressure losses during CO_2 transport in the surface and subsurface.

CHAPTER V

ENERGY REQUIREMENTS AND ENVIRONMENTAL IMPACTS

The aquifer management strategies proposed in Chapter III have been applied to the geological model created in Chapter IV. Result shows that for the Woodbine aquifer, a CO_2-brine displacement strategy increases project life from 20 years to more than 200 years when compared with bulk injection. However, this will come with an increase in project cost.

This chapter considers the surface CO_2 transport and estimates what percentage of power plant energy capacity is needed to inject CO_2 in the Woodbine aquifer using the aquifer management strategies described. Also, a comparison is made between the operational costs of external brine disposal compared to brine desalination with internal saturated brine injection. The potential environmental impact of such a project on the East Texas region is highlighted.

5.1 Environmental Impacts of the Wells and Surface Pipelines

This section addresses the number of injection and production wells, the pipeline length, the surface land use, the cost and the energy required to inject the 3.2 BSCF/day CO_2 into the Woodbine aquifer. A suitable injection site for storing the CO_2 produced by the coal-fired power plants in the vicinity of the Woodbine aquifer has been shown in the rectangle marked in Figure 3.2. The site was selected based on its higher salinity and net thickness compared to other areas in the region.

The most economical way to transport CO_2 by land over long distances is by pipelines. Pipeline companies are allowed to construct and maintain pipeline right-of-way across privately owned property after there has been written agreements, or easements, between landowners and pipeline companies. According to Wilson and Figueiredo (2006), there is a fundamental ambiguity pertaining to the determination of property rights for a saline formation with respect to geologic sequestration because of the lack of case law on this point.

There are different classes of injection wells regulated by the Railroad Commission of Texas. Injection wells due to salt-mining and brine injection wells are Class III whereas wells injecting wastes due to oil and gas processes are Class II. An operator must get a permit in accordance to the Texas Railroad Commission's Underground Injection Control (UIC) program before injecting fluids into a formation.

After it has been separated from other flue gases and captured, the initial pressure of CO_2 is about atmospheric pressure. Transporting CO_2 at atmospheric pressure is inefficient because of the low density of CO_2 and relatively high pressure drop per unit length of pipeline (McCoy and Rubin 2008). To efficiently transport CO_2 via a pipeline, it should be compressed from an initial pressure of about 0.1 MPa (14.5 psi) to above a critical pressure of 7.38 MPa (1070 psi) at which CO_2 is in its supercritical state. Furthermore, a pump will be required to boost CO_2 from 7.38 MPa (1070 psi) to the injection bottom-hole pressure.

The high-pressure CO_2 pipeline connecting these power plants to the wellheads would pass through several counties and landmarks. Some of the counties in the vicinity of the Woodbine aquifer that could be affected if the simulated project were ever implemented are Rains, Wood, Van Zandt, Henderson, Anderson, Houston, Cherokee, Smith, Upshur, Franklin, Titus, Navarro, Brazos, and Leon. Some of the major highways on the route that the pipeline should go through are SH 276, SH 37, SH 175, SH 79, I 20, I 30, I 45 and the national protected areas in these counties are (1) Little Sandy National Wildlife Refuge, (2) Neeches River National Wildlife Refuge, and (3) Davy Crockett National Forest.

5.1.1 Bulk injection

The widely proposed method of CO_2 storage in deep saline aquifer is by bulk injection. This study reveals not only that the pipeline footprint for storing the 3.2 BSCF/day of CO_2 in the designated injection site in the Woodbine aquifer is enormous but also, that high-pressure CO_2 pipelines must pass through several counties.

From Equation 4.4, it could be seen that storing the total CO_2 produced by the power plants in the vicinity of the Woodbine aquifer by bulk injection strategy will require 21 injection wells with an inter-well distance between 4.5 and 6 miles and an

injection rate of 156 MMSCF/day for each well. At the previously determined storage efficiency of 0.46%, this network supports continuous CO_2 injection for 20 years. Possible locations of the injection wells were shown in Fig. 4.9 and a simplified wellhead network is shown in Figure 5.1.

The length of the pipeline required for bulk injection depends on the distance of the power plant to the injection site, the terrain through which the pipeline would pass to the injection site, and the amount of CO_2 produced by each power plant. Based on the selected injection sites, the estimated pipeline length required for bulk injection is about 875 km. A possible pipeline network connecting power plants to the injection wells is diagrammed in Figure 5.1.

The calculation of the pipeline diameter is an iterative process (McCollum and Ogden 2006) where an initial diameter is assumed and an actual diameter is calculated. The iteration continues until a set tolerance (maximum error) is met. The process also requires the knowledge of CO_2 pressure and temperature in the pipeline. The pressure in the pipeline is indicated by the pipeline inlet and outlet pressure P_1 and P_2. The pipeline average pressure can be calculated as (McCollum and Ogden 2006; McCoy and Rubin 2008)

$$P_{ave} = \frac{P_1 + P_2}{2} \text{ or } P_{ave} = \frac{2}{3}\left(P_2 + P_1 - \frac{P_2 P_1}{P_2 + P_1} \right) \tag{5.1}$$

The average temperature in the pipeline is assumed constant at ground temperature. An estimate of CO_2 density and viscosity in the pipeline approximated at average pressure and temperature conditions is also required.

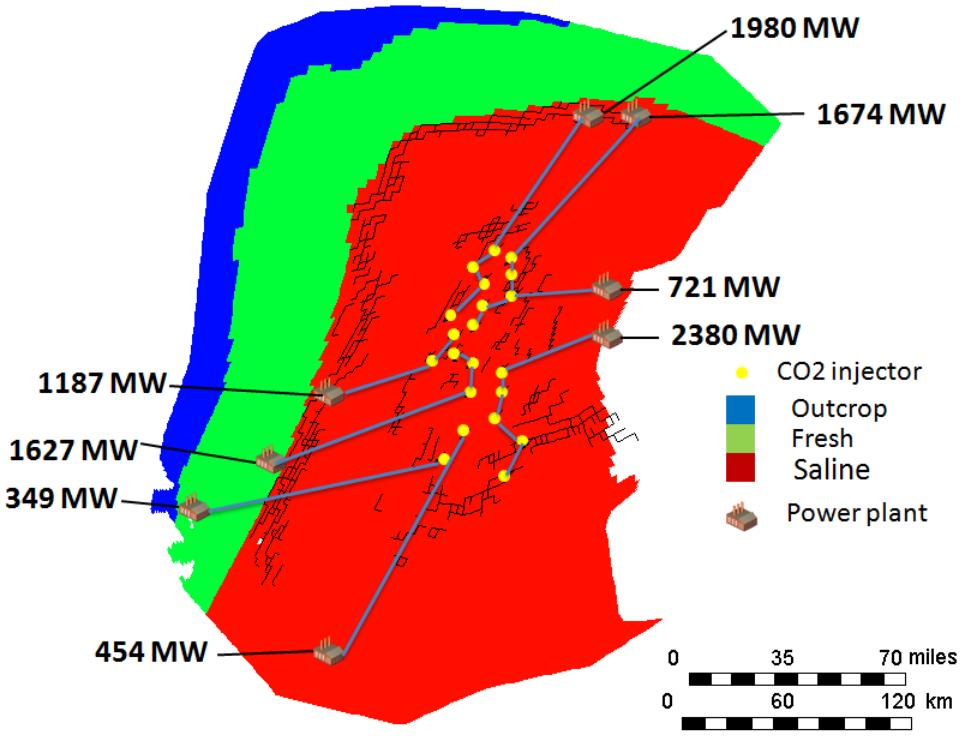

Figure 5.1—High pressure CO_2 pipeline network connecting power plants to injection wells (bulk injection case).

To calculate the diameter of the pipeline, it is first necessary to calculate the Reynolds number, the fanning friction factor, and finally use Equation 5.4 (McCollum and Ogden 2006) to calculate the pipeline diameter. The Reynolds number (Re) and Fanning friction factor (F_f) are calculated using Equations 5.2 and 5.3.

$$\mathrm{Re} = \left(\frac{4(1000)}{(24)(3600)(0.0254)}\right)\frac{\mathrm{m}}{\pi\mu \mathrm{D}} \tag{5.2}$$

$$F_f = 1/4\left[-1.8\mathrm{Log}_{10}\left\{\frac{6.91}{\mathrm{Re}} + \left(\frac{12(\varepsilon/D)}{3.7}\right)^{1.11}\right\}^2\right] \tag{5.3}$$

$$D = \left(\frac{1}{0.0254}\right)\left[\frac{32F_f m^2\left(\frac{1000}{(24)(3600)}\right)^2}{1000\pi^2\rho\frac{\Delta p}{L}}\right]^{1/5} \tag{5.4}$$

The roughness of the pipe ε is assumed to be 0.00015 ft.

With this approach, the pressure drop in the pipeline ΔP is fixed as an input value, and the required diameter is calculated. Another approach is to fix the diameter and calculate the corresponding pressure drop, all other parameter staying the same. This study uses an approach in which the diameter of the pipeline is fixed to 20 inches and the pressure loss along the length of the pipeline is calculated.

The pressure drop along the length of a pipeline is:

$$\Delta P = \frac{42.87\, f_f m^2 L}{\pi^2 \rho D^5} \tag{5.5}$$

where D (m); ρ (kg/m^3); m (kg/day); L (km); ΔP (MPa)

Because power plants do not have the same capacity and thus would emit varying amounts (tonnes/day) of CO_2, it is expected that the pipeline diameter might vary from plant to plant to minimize pressure drop. A literature review of CO_2 pipeline diameter shows that there is no standard for the maximum diameter of a high-pressure CO_2 pipeline. Two existing projects seen in literature are (1) 210 miles of 20-inch high pressure CO_2 pipeline capable of transporting 7.3 million tonnes CO_2/year from the Bravo Dome formation to the Permian Basin at supercritical conditions and (2) SACROC CO_2 pipeline system consisting of 40 miles of 12-inch pipeline and 180 miles of 16-inch pipeline capable of transporting 4.4 million tonnes CO_2/year (Babcock Eagleton Inc 2010). The pipeline lengths in both of these examples are small compared to the 620 mi of high-pressure pipeline required for this hypothetical project. The estimated rates required for this project range between 2.1 to 14.3 million tonnes CO_2/year depending on the size of the power plant.

Using the power plants in this preliminary study as an example, the smallest power plant in this vicinity has a capacity of 349 MW (5740 tonnes/day), a distance of 122 km to the injection site and a calculated diameter of 16.5 inches whereas the biggest power plant has a capacity of 2380 MW (39,123 tonnes/day), a distance of 197 km to the injection site and a calculated diameter of 35.3 inches.

There are pressure losses from friction in the injection tubing when injecting CO_2 from the well head to the injection zone. The frictional pressure loss in the injection

tubing is found by first calculating the Reynolds number, the Fanning friction factor, the velocity of CO_2 in the tubing, and finally the pressure loss is calculated (McCollum and Ogden 2006). Similar to calculating the pipeline diameter, Equations 5.2 and 5.3 are used to calculate the Reynolds number and Fanning friction factor. The CO_2 velocity is calculated using Equation 5.6 wheras the pressure drop along the length of the injection tubing is calculated using Equation 5.7.

$$V_{pipe} = \left(\frac{\frac{1000m}{(24)(3600)}}{\rho\pi\left(D_{pipe}/2\right)^2} \right) \tag{5.6}$$

$$\Delta P_{pipe} = \left(\frac{\rho F_f H V_{pipe}^2}{2D_{pipe} \times 10^6} \right) \tag{5.7}$$

The following assumptions are used for wellbore transport: ρ = 840 kg/m^3; m = 8213.5 tonnes/day (the equivalent for 500-MW coal-fired power plant) and D_{pipe} = 0.2 m. The pressure drop for each injector would vary depending on the depth at which the CO_2 is injected (i.e., the length of the tubing). The pressure loss for each CO_2 injector is shown in Table B-1 in Appendix B.

5.1.2 CO_2-Brine displacement with external brine disposal

In addition to surface requirements for the bulk injection strategy, the CO_2-brine displacement storage strategy would require production wells, production pumps, and brine disposal system. Injection wells are used to produce same reservoir volume of brine as CO_2 injected. Additional surface equipment will be needed for the disposal of the produced brine.

The number of injection and production wells required depends on the volume of CO_2 and brine injected and produced respectively in each well. For this injection strategy, 21 injection wells with same location as those of the bulk injection case and 21 production wells were used. The inter-well distances between injectors or producers are not constant. The producers are set in a peripheral pattern. Figure 5.2 shows the location of the injectors and producers used for the displacement case with external brine disposal.

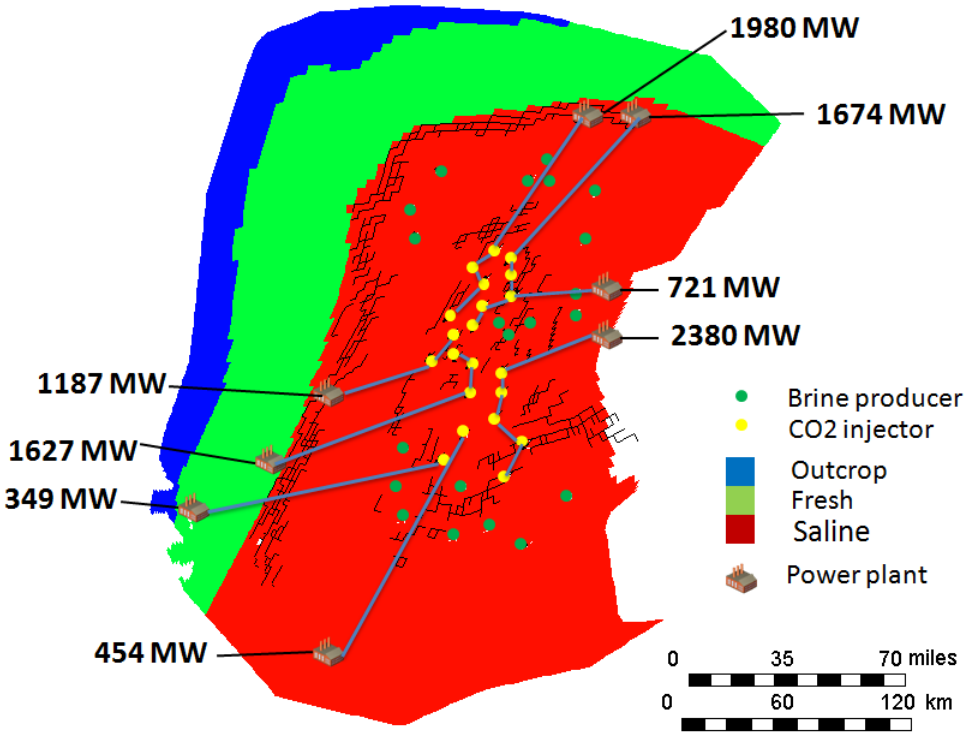

Figure 5.2—CO_2 pipeline network for CO_2-brine displacement strategy.

The location of the CO_2 injectors are fixed and do not vary with different strategies for the geological case. Therefore, the pipeline length required for the brine displacement case is the same as that required for the bulk injection case. However, additional surface facilities will be required to manage brine production.

A way to handle the produced brine is to treat it like oil-field waste and inject it in deep wells. However, the difference is that these are at very high rates compared to the norm of the oil industry and there is no need to pass it through chemical treatments to remove organic components before injecting it into deep wells. Brine could be disposed from individual brine production well sites or a unified approach could be taken to pipeline produced brine to a centralized site for disposal.

A 0.2-m-diameter production tubing is used for each brine producer. The pressure drop in the brine production line is calculated similarly to the pressure drop in the CO_2 production line. The frictional pressure drop due in each brine producer is shown in Table B-2 in Appendix B.

5.1.3 CO_2-Brine displacement with internal saturated brine injection

This management strategy proposes desalination of the produced brine and subsequent injection of the saturated brine into the same aquifer. The amount of saturated brine injected will depend on the salinity of the produced brine. This study assumes a salinity of 90,000 ppm for native brine and 350,000 ppm for saturated brine. This section considers additional surface transport needed for brine desalination and injection.

The number and location of injection and production wells are similar to that of the CO_2-brine displacement with brine disposal. However, additional 21 injection wells are needed for the brine injection.

Brine injection wells should be placed at a distance away from CO_2 injectors to avoid increasing the bottomhole pressure and also placed away from brine producers to avoid saturated brine breakthrough.

The number of desalination unit used is an economic decision. A centralized desalination unit would be a logical choice. Figure 5.3 show the pipeline network for the saturated brine injection case with a centralized brine desalination unit.

The additional length of pipeline required for this injection strategy compared to the bulk injection case will be that required to transport native brine to the desalination plant and pipeline to transport saturated brine from the desalination plant to the brine injectors.

The pressure drop due to producing 11,730 m^3/d brine and injecting 3460 m^3/d saturated brine for each saturated brine injector and brine producer is shown in Table B-3 and B-4 in Appendix B.

Injection of the saturated brine into the Woodbine aquifer will be a small additional energy requirement.

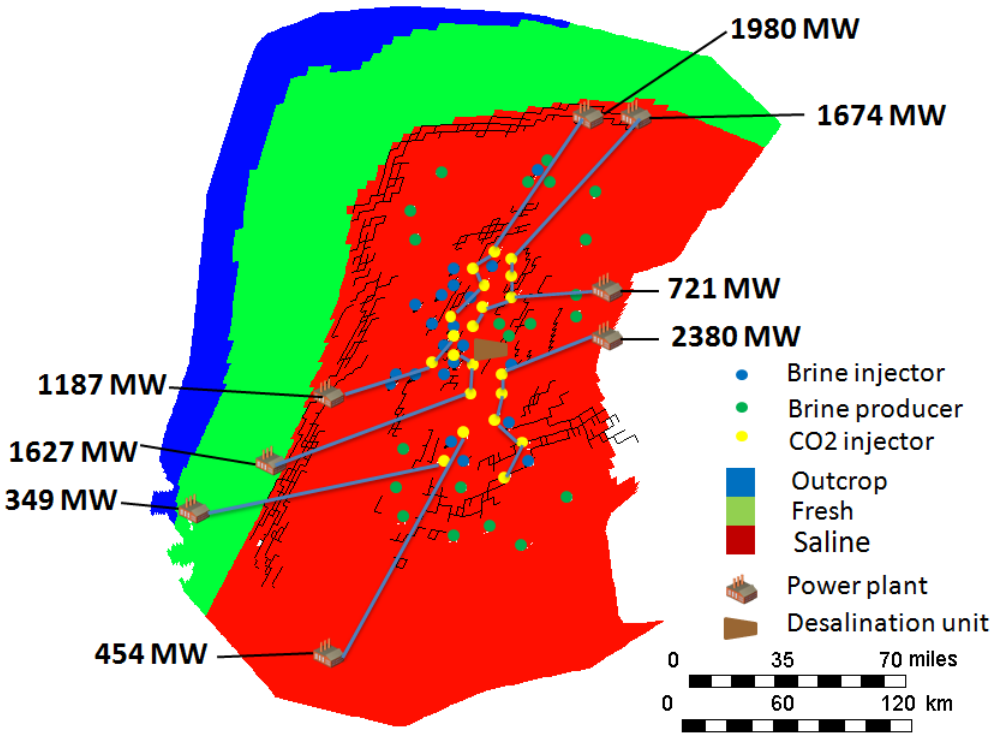

Figure 5.3—CO_2 pipeline network for internal saturated brine injection case.

5.2 Energy Requirements

This section deals with the energy required for the CO_2 storage operation. Most of the energy is required for CO_2 injection. The additional energy required for brine production and disposal or reinjection is comparatively less.

5.2.1 CO_2 injection

This subsection deals with the energy required to (1) compress CO_2 from its gaseous phase at atmospheric pressure ($P_{initial}$ = 0.1 MPa) to its supercritical (dense) phase (P_{cutoff} = 7.38 MPa and T = 31.1ºC) where it is suitable for pipeline transport and (2) use booster pumps to further pressurize the CO_2 to its final injection pressure P_{final} which depends on the bottom hole pressure (BHP) set for the well.

Compressing CO_2 from atmospheric pressure to the cutoff pressure is performed in stages. The compression power requirement for each stage is given by the following equation (McCollum and Ogden 2006):

$$W_{s,i} = \left(\frac{1000}{24 * 3600}\right)\left(\frac{mZ_s RT_{in}}{M\eta_{is}}\right)\left(\frac{k_s}{k_s - 1}\right)\left[(CR)^{\left(\frac{k_s}{k_s - 1}\right)} - 1\right] \quad (5.8)$$

$$CR = \left(\frac{P_{cut-off}}{P_{initial}}\right)^{\left(\frac{1}{N_{stage}}\right)} \quad (5.9)$$

Assuming a 500-MW power plant, an average CO_2 compressibility for each individual stage Z_s of 0.995, a gas constant R = 8.314 kJ/(kmol·K) , a CO_2 gas inlet temperature at the compressor T_{in}= 313.15 K, an isentropic efficiency of compressor η_{is} = 0.75, and five stages, following the steps enumerated by (McCollum and Ogden, 2006) the compression power requirement for each stage is $W_{s,1}$ = 7061 kW, $W_{s,2}$ = 7007 kW, W_{s3} = 6942 kW, $W_{s,4}$ = 6808 kW, $W_{s,5}$ = 6550 kW and the total power requirement of the compressor is 34,369 kW. The maximum size of one compressor train is 40,000 kW, therefore the number of trains required is one.

The pumping power requirement for boosting the CO_2 pressure from 7.38 to 21.15 MPa is calculated using the following equation(McCollum and Ogden 2006):

$$W_p = \left(\frac{1000 * 10}{24 * 36}\right)\left[\frac{m\left(P_{final} - P_{cut-off}\right)}{\rho\eta_p}\right] \quad (5.10)$$

where m is the CO_2 mass flow rate (tonnes/day) and the following values are assumed η_p = 0.75, ρ = 630 kg/m^3. The calculated pumping power requirement is 2768 kW. Table 5.5 shows the compression power requirement, the number of trains required, and the pumping power requirement for the power plants in the vicinity of the Woodbine aquifer. It can be seen from Table 5.5 that about 7% of the power plant capacity would be used for CO_2 compression whereas 0.6% is used to pump CO_2.

5. 2.2 Brine production and transport

In addition to the energy required to compress and transport CO_2, the energy required to pump brine from the reservoir to the surface is given as

$$P_h = q\rho gh \quad (5.11)$$

where P_h is the power (W), q is the flow rate (m^3/s), g is the acceleration due to gravity (m/s^2), and h is the depth of the well (m).

Table 5.5—CO_2 compression and pumping energy requirements for coal-fired power plants near Woodbine aquifer

Plant capacity (MW)								
	454	349	1627	1187	1980	1674	721	2380
Compression power requirement (kW)								
Stage 1	6412	4929	22,977	16,763	27,962	23,640	10,182	33,611
Stage 2	6363	4891	22,801	16,635	27,748	23,460	10,104	33,354
Stage 3	6304	4846	22,591	16,481	27,492	22,796	9818	33,046
Stage 4	6182	4752	22,155	16,164	26,962	22,796	9818	32,409
Stage 5	5947	4572	21,313	15,549	25,937	21,928	9445	31,176
Total compression power (kW)	31,207	23,989	111,837	81,592	136,101	115,068	49,560	163,597
Number of compression trains	1	1	3	3	4	3	2	5
Pumping power requirement (kW)								
	2514	1932	9008	6572	10,963	9268	3992	13,177

Using the injector/producer couplet pattern as an example, the energy required to pump 41,865 bbl/day of brine with a density of 1046 kg/m^3 through a depth of 1615 m is 960 kW. The power required to pump the displaced brine using the injector/producer couplet pattern will be 40 MW. The actual pump power required will depend on the efficiency of the pump.

5.2.3 Brine desalination and internal saturated brine injection

The two major methods of desalination are membrane separation and thermal separation processes. Membrane separation like reverse osmosis (RO) are typically used for water with salinity up to 45,000 ppm. Depending on the use of the water, a second RO pass maybe needed to reduce the salinity to an acceptable level (Ettouney 2002). Thermal separation processes can desalinate brine with salinity much greater than seawater (35,000 ppm). However, the higher the salinity the higher the separation cost.

The most widely used thermal desalination processes are multistage flash desalination (MSF), multiple-effect evaporation (MEE), and mechanical vapor compression (MVC). In the MVC system, the saline water is evaporated by the application of heat delivered by the condensing compressed vapor. The MSF and MEE have a higher energy requirement compared to the MVC. The specific power consumption of the MVC varies over a range of 6–10 kWh/m^3 (Ettouney and El-

Dessouky 2002). The unit product cost is affected by variables such as salinity and quality of feed water, plant capacity, energy cost, plant life, and amortization.

The heat requirements for MSF is about 40–120 kWh/m^3 while that for MEE is about 30–120 kWh/m^3. The electrical energy (pumping) required for MSF is 2.5–5 kWh_e/m^3 whereas that for MEE is about 2–2.5 kWh_e/m^3. The combined desalination energy demand is about 21–58 kWh_e/m^3 for MSF, 15–58 kWh_e/m^3 for MEE (Semiat 2008) and 6–10 kWh/m^3 for MVC.

Using an advanced MVC system, the compressor electricity requirement for desalinating brine to an outlet concentration of 350,000 ppm is between 4–9 kWh/m^3 depending on the temperature difference between the latent heat exchanger as shown in Figure 5.4. The calculation steps in obtaining Figure 5.4 are shown in Appendix C.

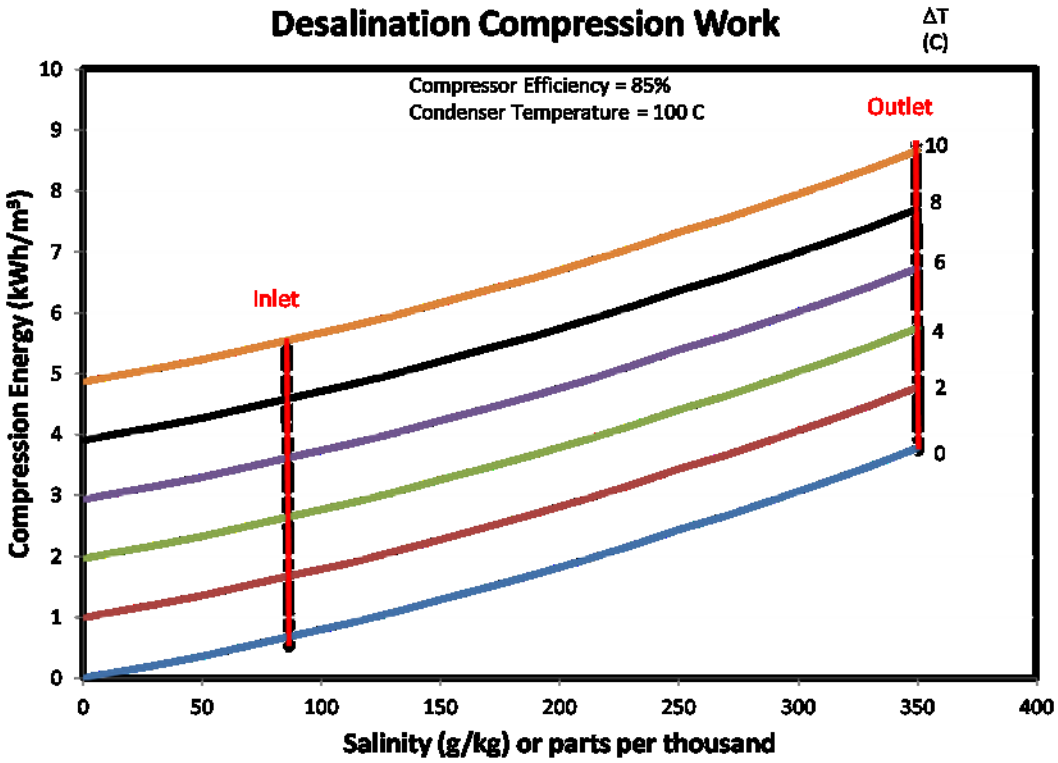

Figure 5.4—Compression electricity requirement for mechanical vapor compression.

The amount of fresh water after desalination is about 1.5 million bbl/day. This is the same as the volume of CO_2 injected. Injection of CO_2 and saturated brine effectively displaces the native brine from the aquifer.

In addition to energy required to transport CO_2, produce native brine, and inject the saturated brine, there is the energy required for brine desalination. No reference addressing the energy required to desalinate brine with salinity greater than seawater was found in the literature. Again assuming the energy required to desalinate 90,000 ppm saline water is twice that required desalinating seawater, and using a MEE MVC desalination system, the desalination energy demand will be 12–20 kWh/ m^3. Therefore, the daily desalination energy required will be 3.36–5.59 GWh, which is a maximum of about 2.3% of the total capacity of the power plants. The compression electricity requirement for an advanced MVC system assuming a temperature difference of 2ºC between the compressor inlet and outlet is 4 kWh/m^3 from Figure 5.4. The daily compression electricity required to desalinate 1.71 million bbl/day will be 1.1 GWh which is about 0.44% of the total capacity of the power plant.

The key energy requirements for the CO_2 sequestration operations are summarized in Table 5.6. Although the energy for desalination of the brine may or may not be generated by the neighboring power plants, it is instructive to consider this as part of the operating cost to sequester CO_2. The table shows that the overall energy cost ranges from 7.43–10.2% of the total energy generated by the power plants, a not insignificant portion.

Table 5.6—Key energy requirements for the CO_2 sequestration operations considered in this study

Plant Capacity (MW)								
	454	349	1627	1187	1980	1674	721	2380
Bulk Injection								
CO_2 compression power (kW)	31,207	23,989	111,837	81,592	136,101	115,068	49,560	163,597
CO_2 pumping power (kW)	2514	1932	9008	6572	10,963	9268	3992	13,177
Total power requirement (kW)	33,721	25,921	120,845	88,164	147,064	124,336	53,552	176,774
Percent of plant power	**7.43**							
CO_2-brine displacement with external brine disposal								
CO_2 compression power (kW)	31,207	23,989	111,837	81,592	136,101	115,068	49,560	163,597
CO_2 pumping power (kW)	2514	1932	9008	6572	10,963	9268	3992	13,177
Brine production power (kW)	2161	1661	7745	5650	9425	7968	3432	11,329
Total power requirement (kW)	35,882	27,582	128,590	93,814	156,489	132,304	56,984	188,103
Percent of plant power	**7.9**							
CO_2-brine displacement with internal saturated brine injection								
CO_2 compression power (kW)	31,207	23,989	111,837	81,592	136,101	115,068	49,560	163,597
CO_2 pumping power (kW)	2514	1932	9008	6572	10,963	9268	3992	13,177
Brine production power (kW)	2716	2088	9735	7102	11,847	10,016	4314	14,240
Brine desalination power (kW)	10,442	8027	37,421	27,301	45,540	38,502	16,583	54,740
Total power requirement (kW)	46,879	36,036	168,001	122,567	204,451	172,854	59,519	245,754
Percent of plant power	**10.2**							

5.3 Estimates for Capital Expenditures for Wells, Pipelines, and Desalination Plant

This section deals with the estimated cost of the CO_2 storage operation. This study focuses on capital expenditure for pipelines, wells, and desalination plant.

5.3.1 Cost of pipeline network

The installed cost of a pipeline depends on four major factors: material, labor, right-of-way (ROW) and miscellaneous expenses (Essandoh-Yeddu and Gulen 2008). Different pipeline cost models exists for example MIT model by Heddle et al. (2003), IEA GHG (2005), McCollum and Ogden (2006) and, McCoy and Rubin (2008). However, because detailed construction data for actual CO_2 pipeline costs are uncommon and largely outdated, most of them used historical natural gas pipeline costs to develop the cost equations for their cost model.

Essandoh and Gullen (2008) created a cost model based on modifications to the MIT and IEA model because they used historical cost data for natural gas pipeline construction in the United States, and it was possible to get a unified common factor from their model equations. The modified cost model accounts for an escalation factor λ for the total CO_2 pipeline capital cost as

$$\lambda = \frac{3\eta(\gamma\alpha\beta)}{\gamma + \alpha + \beta} \quad (\gamma, \alpha, \beta > 0) \tag{5.12}$$

where η is labor escalation cost factor, γ is material escalation cost factor, α is miscellaneous escalation cost factor, and β is ROW escalation cost factor.

The escalation factor is used to normalize the cost for different years. The labor escalation cost factor is calculated as

$$\eta = \frac{\text{average cost of labor in current year}}{\text{average cost of labor in base year}} \tag{5.13}$$

γ,α, β are calculated similar to η. For year *n*, the modified MIT model equation is

$$\lambda_n = \left(\frac{\eta_n \gamma_n \alpha_n \beta_n}{\gamma_n + \alpha_n + \beta_n}\right) * \$62{,}967/\text{in/km} \tag{5.14}$$

The modified IEA GHG model equation is

$$\lambda_n = \left(\frac{\eta_n \gamma_n \alpha_n \beta_n}{\gamma_n + \alpha_n + \beta_n}\right) * \$77{,}667/\text{in/km} \tag{5.15}$$

In the various pipeline cost models that exist in the literature, the IEA GHG model provides the highest and the MIT model provides the lowest cost estimates. Assuming an escalation factor of 1.1, the pipeline cost model for the MIT and IEA GHG are \$69,263/(in·km) and \$85,434/(in·km), respectively. Therefore, the cost range of transporting CO_2 from the coal-fired power plants in the vicinity of the Woodbine aquifer, through a pipeline network of 20-inch diameter and 875-km length is between \$1.21 and \$1.5 billion.

5.3.2 CO_2 compression and pumping cost

Transporting CO_2 efficiently from the power plant to the injection well requires CO_2 to be compressed from an initial pressure ($P_{initial}$) to a suitable pressure where it can be pumped ($P_{cut\text{-}off}$), and then CO_2 is pumped from $P_{cut\text{-}off}$ to the desired injection pressure (P_{final}). McColum and Ogden (2006) provided a capital cost model for CO_2 compression and pumping. The capital cost of the compressor is calculated as

$$C_{comp} = m_{train} N_{train} \left[0.13 \times 10^6 \times (m_{train})^{-0.71} + 1.4 \times 10^6 \times (m_{train})^{-0.6} \ln\left(\frac{P_{cut-off}}{P_{initial}}\right)\right] \tag{5.16}$$

where

m_{train} = CO_2 mass flowrate through each compressor train (kg/s)

C_{comp} = capital cost of compression (\$)

N_{train} = number of parallel compressor trains

The capital cost of the pump is calculated as

$$C_{pump} = 1110 W_p + 0.07 \times 10^6 \tag{5.17}$$

where

C_{pump} = capital cost of pump (\$)

W_p = pumping power requirement (kW)

From Equations 5.16 and 5.17, the capital cost of compressing and pumping CO_2 from the power plants nearby the Woodbine aquifer is \$900 million and \$64 million, respectively.

5.3.3 Production and injection well cost

The capital expenditure for production and injection wells varies from region to region and the well depth. The EIA (2010) report was used to estimate the capital expenditure for production and injection wells in this study. The current data in the report was for year 2009. Expenditure for producing equipment includes cost of tubing, rods and pumps, pumping equipment, flowlines, and manifold. The additional expenditure for injection equipment includes cost of supply wells, distribution lines, and electrical source.

The average capital cost for an onshore 8000-ft production well is $2,612,000 per well whereas that of an injection well is $4,455,100 per well. The bulk injection strategy requires 21 injection wells and will cost $93.56 million. For the CO_2-brine displacement cases, the external brine disposal strategy has 21 injection wells and 21 production wells and will cost $148.4 million whereas the internal saturated brine injection strategy has 42 injection wells and 21 production wells and would cost $242 million. The cost of drilling is not included in the estimated well cost.

5.3.4 Brine disposal cost

In his report, Veil (2007) showed tables that provide cost data for disposing three categories of wastes: (1) solid and oily waste; (2) produced water, rain water, and other types of dirty-water wastes; and (3) water-based drilling wastes. Disposal costs just for injection of produced water in Texas ranges between $0.23–$0.35/bbl.

The average brine production rate is 10,245 m^3/day multiplied by 21 production wells which is about 215,135 m^3/day. Assuming a disposal cost of $2.2/$m^3$, the overall brine disposal cost will be $473,297/day.

5.3.5 Desalination cost

Research performed by (Ettouney 2002) using seawater as the basis shows that the unit product cost of a 20,000 m^3/day MVC system is $0.46/$m^3$, that of a 45,460 m^3/day MSF system is between $1.498 and $1.61/$m^3$,whereas that of a 37,850 m^3/day MEE system is $1.08/$m^3$. The MVC system is the best in terms of product cost, but it may be limited in terms of plant capacity. A detailed search of the literature for

references addressing the cost of desalinating brine with salinity greater than seawater was conducted, but none was found. Assuming the unit product cost for desalinating 90,000-ppm brine is twice that of seawater, it is interesting to note that at $\$2.16/m^3$ for the MEE system, the cost per day to desalinate 1.71 million bbls (271,945 m^3) per day of produced brine is $587,400 per day, which is more than the estimated cost to dispose of the brine ($473,297 per day) neglecting the capital cost of the saturated brine injection wells.

5.3.6 Energy cost of CO_2 injection

This section estimates the cost ($/kWh) of CO_2 injection into the Woodbine aquifer using the three management strategies previously described. CO_2 injection cost is calculated by adding the transport cost; i.e., pipeline cost, compressor cost, and pump cost; the well cost; and the disposal or desalination cost for the case of the CO2-brine displacement strategies. Assumptions made include: a 10% interest rate on capital cost, fresh water is sold at $\$0.5/m^3$, and a 5% point margin of error.

The estimated CO_2 injection cost is $0.00132–$0.00146/kWh for the bulk injection, $0.00191–$0.00211/kWh for the external brine disposal case, and $0.0019–$0.00209/kWh for the internal saturated brine injection case.

5.4 Chapter Conclusions

This chapter reviews the environmental impacts and estimates the energy required as a percentage of the power plant capacity to perform a CO_2 sequestration project using any one of the three aquifer management strategies considered in this study.

The environmental impact such a project could have on the East Texas region include high-pressure CO_2 passing through several counties and possibly landmarks, surface land use for injection and production operation and brine disposal, and the possibility of CO_2 leak to the environment.

Most of energy is required for any of the three aquifer management strategies involves compressing CO_2 from atmospheric pressure to its critical pressure before it is pumped to its final injection pressure. Frictional pressure losses in transport pipelines CO_2 and wells are small by comparison. For CO_2-brine displacement strategies there are

additional pipeline and well losses related to CO_2-brine injection and production, and additional facilities required for brine disposal or desalination.

Energy required for compression and desalination is about 6.8% and 2.3%, respectively, of the power plant capacity. Altogether, the energy requirements for bulk injection, CO_2-brine displacement with external brine disposal, and CO_2-brine displacement with internal saturated brine reinjection are estimated at 7.4%, 7.9% and 10.2%, respectively, of the power plant capacity.

The capital cost of the 20-inch diameter, 875-km-long pipeline network for transporting CO_2 from the coal-fired power plants to the injection site ranges between \$1.21 and \$1.5 billion. The compressor and pump cost is \$900 million and \$64 million, respectively. The well cost of the bulk injection strategy is \$54.85 million, whereas those of the CO_2-brine displacement strategies are \$148.4 million and \$242 million for the brine disposal case and internal saturated brine injection case, respectively. For the CO_2-brine injection with external brine disposal strategy, an average of 1.35 million bbl/day brine is produced and the brine disposal costs is \$473,297/day assuming a disposal cost of \$2.2/m^3. Similarly, assuming a desalination cost of \$2.16/m^3, it will cost \$587,400/day to desalinate 1.71 million bbl per day of produced brine. The overall cost of the bulk injection strategy is \$0.00132–\$0.00146/kWh, whereas those of the CO_2-brine displacement strategies are \$0.00191–\$0.00211/kWh and \$0.0019–\$0.00209/kWh for the brine disposal case and internal saturated brine injection case, respectively.

CHAPTER VI

CONCLUSIONS AND RECOMMENDATIONS

6.1 Conclusions

This study has considered a conceptual approach to increasing the storage efficiency of CO_2 injection in saline formations and investigated what an actual CO_2 storage project might entail using field data for the Woodbine aquifer in East Texas. Initially, a conceptual model with homogeneous and average reservoir properties was used to estimate CO_2 storage capacity using three aquifer management strategies. Subsequently, a full-field simulation model was used to validate the results of the conceptual model and evaluate the potential risk of salt water intrusion or CO_2 contamination into the fresh water aquifer updip from the saline aquifer region into which CO_2 is injected.

The main contributions and conclusions from this study are summarized as follows:

The conceptual model reveals that bulk injection of CO_2 pressurizes the aquifer, has a storage efficiency of 0.46% and can only last for 20 years without risk of fracturing the CO_2 injection wells.

A CO_2-brine displacement strategy can continue injecting CO_2 for as long as 240 years until CO_2 begins to break through in the production wells. This is 12 times more than the bulk injection strategy.

A full-field simulation with geological model validates the claims made by the conceptual model. Results from the geological model shows that CO_2 would not leak into the fresh water region of the aquifer after 1000 years of monitoring if the transmissibility of the Mexia-Talco fault system is 0. However, CO_2 would leak into the fresh water aquifer for fault transmissibilities of 0.1 and 1 for the CO_2-brine displacement strategy.

Under CO_2 injection, the formation geochemistry results in the mineral precipitation of kaolinite, quartz and chamosite, and the dissolution of K-feldspar.

Impurities in the injected CO_2 could lower the pH of the formation from 4.8 for a pure CO_2 stream to 3.3.

High-pressure pipelines and/or wells would impact as many as 15 counties stretching as long as 875 km from the power plants serving as sources for the CO_2 to be sequestered.

Evaluation of the energy requirements for CO_2 storage indicates that desalination of produced brine would not be a deal breaker. As a fraction of the power plant energy capacity, the energy required for CO_2 compression and brine desalination is about 6.8% and 2.3%, respectively. The estimated well cost (CAPEX) for the bulk injection strategy is $54.85 million. For the CO_2-brine displacement strategies, the brine disposal case has an estimated well cost of $148.4 million and a disposal cost of $473,297/day whereas the internal saturated brine case has an estimated well cost of $242 million and a desalination cost of $587,400/day. The overall cost of the bulk injection strategy is $0.00132–$0.00146/kWh, whereas those of the CO_2-brine displacement strategies are $0.00191–$0.00211/kWh and $0.0019–$0.00209/kWh for the brine disposal case and internal saturated brine injection case, respectively.

6.2 Recommendations

This project encountered the following limitations in the commercial simulator used for the flow modeling:

The sudden increase in average pressure after shut-in of CO_2 injectors and brine producers was not expected and not fully understood. Future work should be performed to examine this phenomenon.

The simulation model should be improved upon to rigorously capture the effect of water vaporization.

REFERENCES

Akinnikawe, O.A., Chaudhary, A.S., Vasquez, O.E. et al. 2010. Increasing CO2-Storage Efficiency Through a CO2 Brine-Displacement Approach. Paper SPE 139467 presented at the SPE International Conference on CO2 Capture, Storage, and Utilization, New Orleans, Louisiana, USA. 10–12 November 2010. DOI: 10.2118/139467-MS.

Ambrose, W.A., Hentz, T.F., Bonnaffe, F. et al. 2009. Sequence-stratigraphic controls on complex reservoir architecture of highstand fluvial-dominated deltaic and lowstand valley-fill deposits in the Upper Cretaceous (Cenomanian) Woodbine Group, East Texas field: Regional and local perspectives. *AAPG* **93** (2): 38.

Anchliya, A. and Ehlig-Economides, C.A. 2009. Aquifer Management To Accelerate CO2 Dissolution and Trapping. Paper SPE 126688 presented at the SPE International Conference on CO2 Capture, Storage, and Utilization, San Diego, California, USA. 2–4 November 2009. DOI: 10.2118/139467-MS.

Babcock Eagleton Inc. Representative carbon dioxide projects. http://www.eagletoninc.com/node/13. Accessed 15 September 2010.

Baroni, A., Estublier, E., Deflandre, J.P. et al. 2011. Modelling Surface Displacements Associated With CO_2 Re-injection At Krechba. Paper ARMA 11-227 presented at the 45th U.S. Rock Mechanics / Geomechanics Symposium, San Francisco, California. 26–29 June 2011.

Bennion, B. and Bachu, S. 2005. Relative Permeability Characteristics for Supercritical CO_2 Displacing Water in a Variety of Potential Sequestration Zones in the Western Canada Sedimentary Basin. Paper SPE 95547 presented at the SPE Annual Technical Conference and Exhibition, Dallas, Texas. 9–12 October 2005. DOI: 10.2118/95547-MS.

Beucher, H. and Renard, D. 2009. *Filling with petrophysical properties*. Paris: Ecole de Mines de Paris.

Brian, R.E., Lauren, E.C., and Catherine, A.P. 2010. Limitations for brine acidification due to SO_2 co-injection in geologic carbon sequestration. *International Journal of Greenhouse Gas Control* **4** (3): 575-582.

Brook, E.J. 2005. Tiny Bubbles Tell All. *Science* **310** (5752): 1285-1287. DOI: 10.1126/science.1121535.

Bureau of Economic Geology. Woodbine Formation—East Texas Basin. http://www.beg.utexas.edu/environqlty/co2seq/co2data/6woodbine.htm. Accessed 17 September 2010.

Burton, M., Kumar, N., and Bryant, S.L. 2008. Time-Dependent Injectivity During CO2 Storage in Aquifers. Paper SPE 113937 presented at the SPE/DOE Symposium on Improved Oil Recovery, Tulsa, Oklahoma, USA. 20-23 April 2008. DOI: 10.2118/113937-MS.

Chiaramonte, L. 2008. Geomechanical Characterization and Reservoir Simulation of a CO_2 Sequestration project in a mature oilfield, Teapot Dome, WY. Ph.D. dissertation, Stanford University, Palo Alto, California.

Core Labs. 1972. *A survey of the subsurface saline water of Texas*, Texas Water Development Board. Austin,TX.

Davis, E.J. 2011. Interpretation of CO_2 Sequestration-Induced Surface Deformation over KB-502 at Krechba, Algeria. Paper SPE 147444 presented at the SPE Annual Technical Conference and Exhibition, Denver, Colorado, USA. 30 October–2 November 2011. DOI: 10.2118/147444-MS.

Delshad, M., Wheeler, M.F., and Kong, X. 2010. A Critical Assessment of CO_2 Injection Strategies in Saline Aquifers. Paper SPE 132442 presented at the SPE Western Regional Meeting, Anaheim, California, USA. 27–29 May 2010. DOI: 10.2118/132442-MS.

Dzou, L., Petmecky, S., and Pepper, A. 2000. East Texas Basin petroleum systems revisited : Is long distance migration to the giant East Texas field really necessary? *AAPG Annual Convention Program* **9**: A44.

Ehlig-Economides, C. and Economides, M.J. 2009. Sequestering Carbon Dioxide in a Closed Underground Volume. Paper SPE 124430 presented at the SPE Annual Technical Conference and Exhibition, New Orleans, Louisiana. 10/04/2009. DOI: 10.2118/124430-MS.

Eiken, O., Ringrose, P., Hermanrud, C. et al. 2011. Lessons learned from 14 years of CCS operations: Sleipner, In Salah and Snøhvit. *Energy Procedia* **4** (0): 5541-5548. DOI: 10.1016/j.egypro.2011.02.541.

Energy Information Agency. Costs and Indices for Domestic Oil and Gas Field Equipment and Production Operations. www.eia.org. Accessed 16 May 2012.

Essandoh-Yeddu, J. and Gulen, G. 2008. Economic modeling of carbon dioxide integrated pipeline network for enhanced oil recovery and geologic sequestration in the Texas Gulf Coast region. In *Greenhouse Gas Control Technologies*: Proceedings of the 9th International Conference on *Greenhouse Gas Control Technologies*, 16–20 November 2008, Washington, D.C.

Ettouney, H. and El-Dessouky, H. 2002. Evaluating the Economics of Desalination. *Chemical Engineering Progress*.

Ettouney, H.M. 2002. Evaluating the economics of desalination. *Chemical Engineering Progress* **98** (12): 32-39.

Folger, P. 2007. *Direct Carbon Sequestration: Capturing and Storing CO_2*. CRS Report for Congress RL33801. Congressional Research Service.

Frohlich, C., Porter, E., Hayward, C. et al. 2010. Dallas-Fort Worth Earthquakes coincident with activity associated with natural gas production. *The Leading Edge* **29**: 6.

FutureGen Alliance. 2006. *Heart of Brazos Site Environmental Information Volume*, United States Department Of Energy. Washinghton, D.C.

FutureGen Alliance. 2007. *FutureGen Initial Conceptual Design Report*, United States Department of Energy. Washington, D.C.

Ghaderi, S.M., Keith, D.W., and Leonenko, Y. 2009. Feasibility of Injecting Large Volumes of CO_2 into Aquifers. *Energy Procedia* **1** (1): 3113-3120.

Ghomian, Y., Pope, G.A., and Sepehrnoori, K. 2008. Reservoir simulation of CO_2 sequestration pilot in Frio brine formation, USA Gulf Coast. *Energy* **33** (7): 1055-1067.

Gunter, W.D., Wiwehar, B., and Perkins, E.H. 1997. Aquifer disposal of CO_2-rich greenhouse gases: Extension of the time scale of experiment for CO_2-sequestering reactions by geochemical modelling. *Mineralogy and Petrology* **59** (1): 121-140. DOI: 10.1007/bf01163065.

Healy, J.H., Hamilton, R.M., and Raleigh, C.B. 1970. Earthquakes induced by fluid injection and explosion. *Tectonophysics* **9** (2–3): 205-214. DOI: 10.1016/0040-1951(70)90017-x.

Heddle, G., Herzog, H., and Kleet, M. 2003. The Economics of CO_2 Storage. *MIT LFEE* **2003-003**.

IEAGHG. 2005. *IEA GHG Weyburn CO_2 Monitoring and Storage Project*. IEA Greenhouse Gas R&D Programme. Gloucestershire, UK.

IEAGHG. 2005. *Building the Cost Curves for CO_2 Storage: North America*. IEA Greenhouse Gas R&D Programme. Gloucestershire, UK.

IPCC. 2005. *IPCC Special Report on Carbon Dioxide Capture and Storage*. Prepared by Working Group III of the Intergovernmental Panel on Climate Change [Metz, B., O. Davidson, H. C. de Coninck, M. Loos, and L. A. Meyer (eds.)]. Cambridge University Press, Cambridge, United Kingdom and New York, NY, USA.

Juanes, R., Spiteri, E.J., Orr, F.M. et al. 2006. Impact of relative permeability hysteresis on geological CO_2 storage. *Water Resour. Res.* **42** (12): W12418. DOI: 10.1029/2005wr004806.

Jung, W. and Nicot, J.-P. 2010. Impurities in CO_2-Rich Mixtures Impact CO_2 Pipeline Design: Implications for Calculating CO_2 Transport Capacity. Paper SPE 139712 presented at the SPE International Conference on CO_2 Capture, Storage, and Utilization, New Orleans, Louisiana, USA. 10–12 November 2010. DOI: 10.2118/139712-MS.

Kreitler, C.W., Bracken, B., Collins, E.W., Conti, R., Dutton, S.P., Fogg, G.E., Jackson, M.P.A., McGowen., M.K., Pennington, W.D., Seni, S.J., Wilson, B., Wood, D.H., and Wuerch, H.V. 1981. *Geology and Geohydrology of the East Texas Basin -- A report on the Progress of Nuclear Waste Isolation Feasibility Studies*: Bureau of Economic Geology, The University of Texas at Austin.

Kumar, A., Noh, M.H., Ozah, R.C. et al. 2005. Reservoir Simulation of CO_2 Storage in Deep Saline Aquifers. *SPE Journal* **10** (3): pp. 336-348. DOI: 10.2118/89343-PA.

Kumar, N. 2008. CO_2 Sequestration: Understanding the Plume Dynamics and Estimating Risk. M.S. Thesis University of Texas, Austin, Texas.

Kuo, C.W., Perrin, J.C., and Benson, S.M. 2010. Effect of Gravity, Flow Rate, and Small Scale Heterogeneity on Multiphase Flow of CO_2 and Brine. Paper SPE 132607 presented at the SPE Western Regional Meeting, Anaheim, California, USA. 27–29 May 2010. DOI: 10.2118/132607-MS.

Lucier, A., Zoback, M., Gupta, N. et al. 2011. a coupled geomechanical reservoir simulation analysis of carbon dioxide storage in a saline aquifer in the Ohio River Valley. *Environmental Geosciences* **18**: 9.

Majer, E.L., Baria, R., Stark, M. et al. 2007. Induced seismicity associated with Enhanced Geothermal Systems. *Geothermics* **36** (3): 185-222. DOI: 10.1016/j.geothermics.2007.03.003.

McCollum, D.L. and Ogden, J.M. 2006. *Techno-Economic Model for Compression, Transport, and Storage & Correlations for Estimating Carbon Dioxide Density and Viscosity*. Davis: Institute of Transportation Studies, University of California.

McCoy, S.T. and Rubin, E.S. 2008. An engineering-economic model of pipeline transport of CO_2 with application to carbon capture and storage. *International Journal of Greenhouse Gas Control* **2**: 219-229.

Mendes, R.A., Costa, A.M., Sousa Jr., L.C. et al. 2010. Risks And Mitigation Problems In a CO_2 Injection Project For a Petroleum Onshore Field In Brazil. Paper ARMA-10-162 presented at the 44th U.S. Rock Mechanics Symposium, Salt Lake City, Utah. 27–30 June 2010.

MIT. 2007. *The Future of Coal: Options for a Carbon-Constrained World*. Cambridge, MA: Massachusetts Institute of Technology.

National Energy Technology Laboratory. 2007. *Carbon Sequestration Atlas of the United States and Canada*. United States Department of Energy–Office of Fossil Energy.

National Energy Technology Laboratory. 2010. *Carbon Sequestration Atlas of the United States and Canada*, United States Department of Energy–Office of Fossil Energy.

Nicholson, C. 1992. Earthquakes associated with deep well activities- Comments and case histories. Paper 92-1079 presented at the 33th U.S. Symposium on Rock Mechanics (USRMS), Santa Fe, NM. 01/01/1992.

Nunez, V. and Hovorka, S. 2012. Subsurface Monitoring of Large-Scale CO_2 Injection at SECARBC's Phase III Cranfield Site. Paper CMTC 151504 presented at the Carbon Management Technology Conference, Orlando, Florida, USA. 7–9 February 2012. DOI: 10.7122/151504-MS.

Oliver., W.B. 1971. *Depositional Systems in the Woodbine Formation (Upper Cretaceous), Northeast Texas*. Austin: Bureau of Economic Geology, The University of Texas at Austin.

Protti, G. 2005. Win-Win: Enhanced Oil Recovery And CO_2 Storage At EnCana's Weyburn Oilfield. Paper 18-0986 presented at the 18th World Petroleum Congress, Johannesburg, South Africa. 25–29 September 2005.

Pruess, K., Xu, T., Apps, J. et al. 2003. Numerical Modeling of Aquifer Disposal of CO2. *SPE Journal* **8** (1). DOI: 10.2118/83695-PA.

Qi, R., LaForce, T.C., and Blunt, M.J. 2009. Design of carbon dioxide storage in aquifers. *International Journal of Greenhouse Gas Control* **3** (2): 195-205.

R.W. Harden & Associates Inc. 2004. *North Trinity/Woodbine Aquifer Groundwater Availability Model*, The Texas Water Development Board. Austin, TX.

Semiat, R. 2008. Energy issues in desalination processes. *Environmental Science & Technology* **42** (22): 8193-8201.

Seni, S.J. and Jackson, M.P.A. 1984. *Sedimentary Record of Cretaceous and Tertiary salt Movement, East Texas Basin: Times, Rates, and Volumes of Salt Flow and Their Implications for Nuclear Waste Isolation and Petroleum Exploration*. Austin: Bureau of Economic Geology, The University of Texas at Austin.

Taku Ide, S., Jessen, K., and Orr Jr, F.M. 2007. Storage of CO_2 in saline aquifers: Effects of gravity, viscous, and capillary forces on amount and timing of trapping. *International Journal of Greenhouse Gas Control* **1** (4): 481-491.

Texas Commission on Environment Quality. 2007. *Notice of Priority Groundwater Management Area Report Completion and Availability*. Texas Commission on Environment Quality. Austin, TX.

Texas Water Development Board. 2007. *State Water Plan*, Texas Water Development Board. Austin, TX.

Ukaegbu, C., Gundogan, O., Mackay, E. et al. 2009. Simulation of CO_2 storage in a heterogeneous aquifer. *Proceedings Of The Institution Of Mechanical Engineers Part A-Journal Of Power and Energy* **223** (A3): 249-267.

United States Department of Energy. 2010. *A Policy, Legal, and Regulatory Evaluation of the Feasibility of a National pipeline Infrastructure for the Transport and Storage of Carbon Dioxide*, Southern States Energy Board. Norcross, GA.

United States Energy Information Agency. Existing Electric Generating Units in the United States. http://www.eia.doe.gov/cneaf/electricity/page/capacity. Accessed 17 January 2012.

Van der Meer, L.G.H. 1995. The CO_2 storage efficiency of aquifers. *Energy Conversion and Management* **36** (6-9): 513-518.

Veil, J.A. 2007. *Costs for Off-Site Disposal of Nonhazardous Oil Field Wastes: Salt Caverns Versus Other Disposal Methods*, Argonne National Laboratory. Washington, D.C.

Wang, F.P., Ambrose, W.A., Hentz, T.F. et al. 2008. Engineering and Geologic Characterization of Giant East Texas Oil Field: North and South Pilot Studies. Paper SPE 115683 presented at the SPE Annual Technical Conference and Exhibition, Denver, Colorado, USA. 21–24 September 2008. DOI: 10.2118/115683-MS.

Wilkinson, J.R. and Szafranski, R.C. 2009. Subsurface design for safe, efficient and reliable Carbon Dioxide storage projects. Paper IPTC 13072 presented at the International Petroleum Technology Conference, Doha, Qatar. 7–9 December 2009. DOI: 10.2523/13072-MS.

Willhite, G.P. 1986. *Waterflooding*. SPE textbook series, v. 3. Richardson, TX: Society of Petroleum Engineers. Original edition. ISBN 1555630057 9781555630058.

Wilson, E.J. and Mark A. de Figueiredo. 2006. Geologic Carbon Dioxide Sequestration: An Analysis of Subsurface Property Law. *Environmental Law Institute* **36**: 11.

Wiprut, D. and Zoback, M.D. 2000. Fault reactivation and fluid flow along a previously dormant normal fault in the northern North Sea. *Geology* **28** (7): 4.

Wood, D.H. and Guevara, E.H. 1981. Regional Structural Cross Sections and General Stratigraphy, East Texas Basin, Austin, Texas: Bureau of Economic Geology, University of Texas at Austin.

Xu, X.C., Song, C.S., Wincek, R.T. et al. 2003. Separation of CO_2 from power plant flue gas using a novel CO_2 "molecular basket" adsorbent. *Abstracts Of Papers Of The American Chemical Society* **225**: U854-U855.

Yang, Q. 2008. Dynamic Modelling of CO2 Injection in a Closed Saline Aquifer in the Browse Basin, Western Australia. Paper SPE 115236 presented at the SPE Asia Pacific Oil and Gas Conference and Exhibition, Perth, Australia. 20–22 October 2008. DOI: 10.2118/115236-MS.

Yarus, J.M. and Chambers, R.L. 2006. Practical Geostatistics - An Armchair Overview for Petroleum Reservoir Engineers. *SPE Journal of Petroleum Technology* **58** (11): 78-86. DOI: 10.2118/103357-MS.

Yoon-Seok, C., Nesic, S., and Young, D. 2010. Effect of impurities on the corrosion behavior of CO_2 transmission pipeline steel in supercritical CO_2-water environments. *Environmental Science & Technology* **44** (23): 9233-9238.

APPENDIX A

CHANGES IN CO_2 SATURATION AND PRESSURE FOR VARYING FAULT TRANSMISSIBILITY

A.1 Bulk Injection – CO_2 Saturation Maps

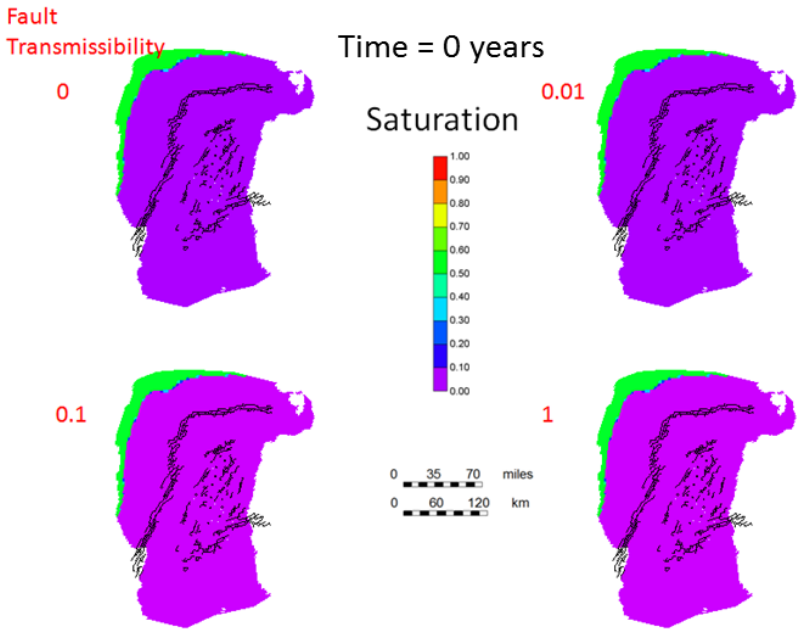

Figure A-1.1—CO_2 saturation at the beginning of bulk injection.

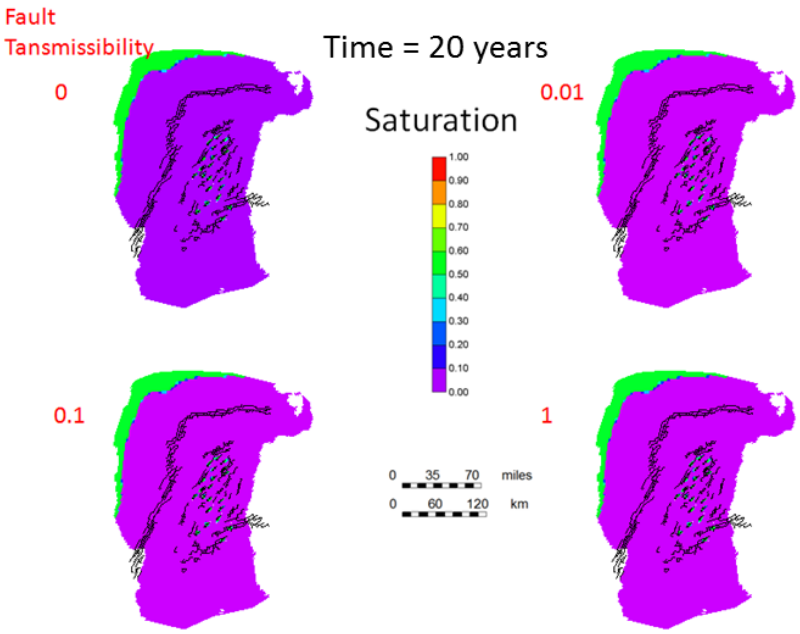

Figure A-1.2— CO_2 saturation at end of bulk injection.

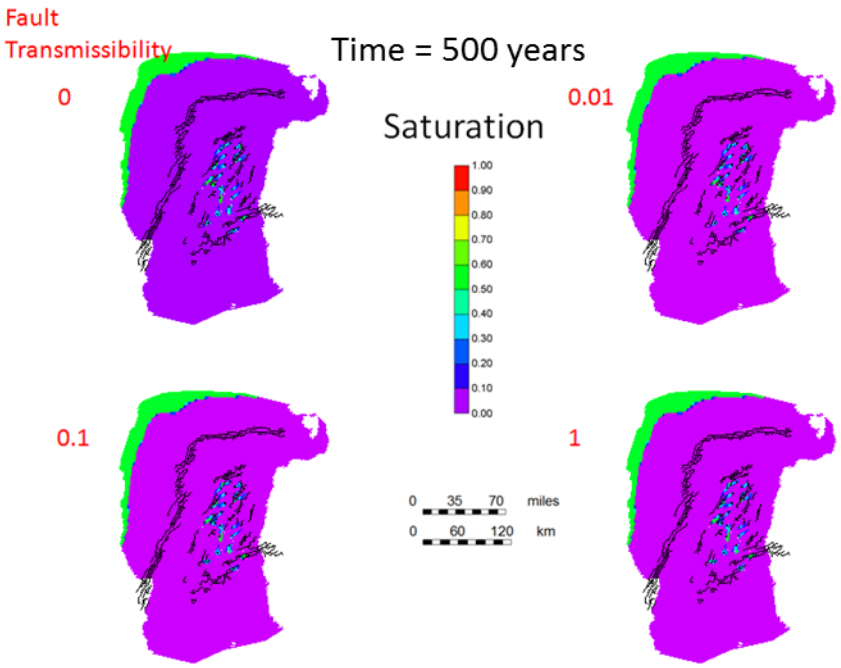

Figure A-1.3—CO_2 saturation at the end of 20 years bulk injection and 500 years monitoring.

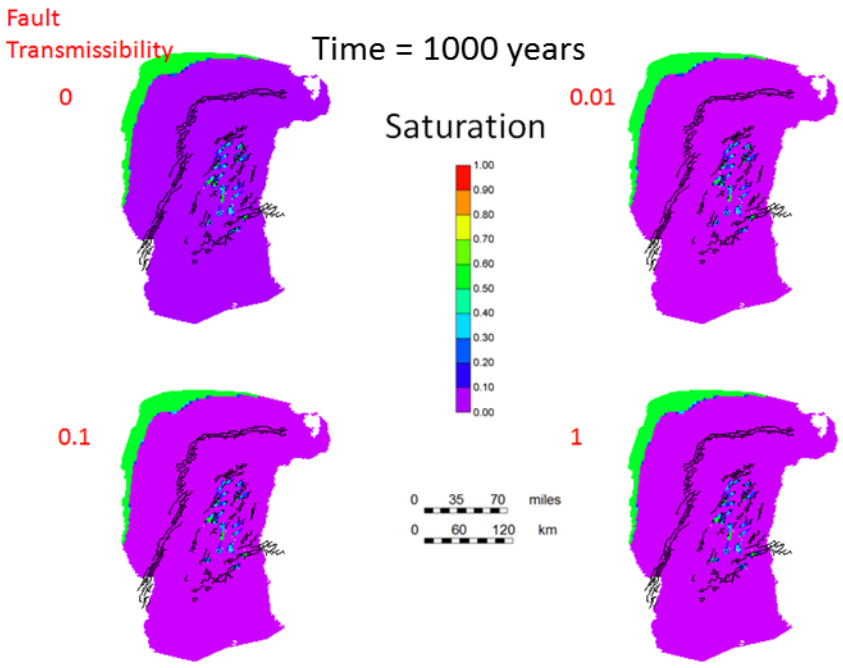

Figure A-1.4—CO_2 saturation at the end of 20 years bulk injection and 1000 years monitoring.

A.2 Bulk Injection – Pressure Change Maps

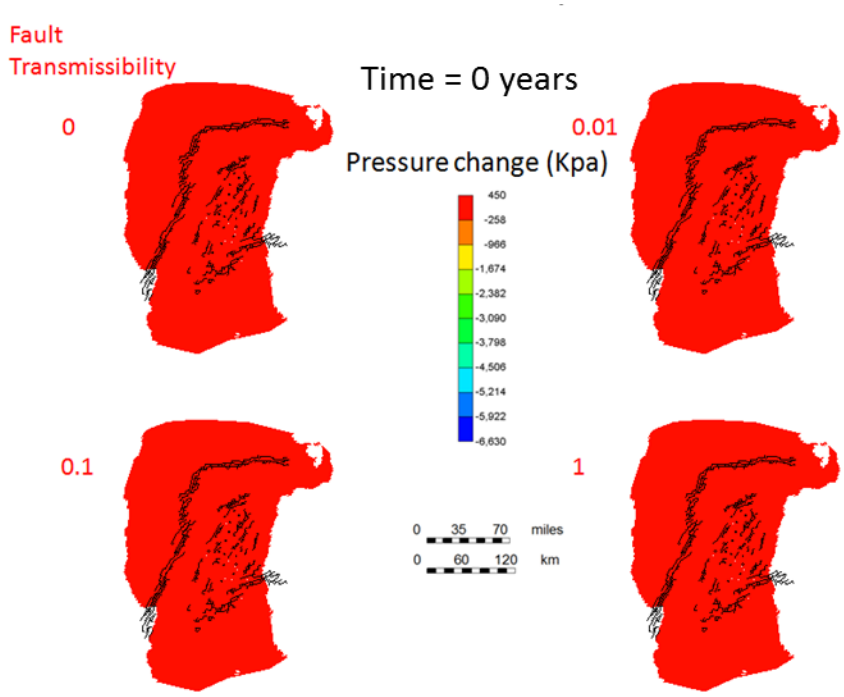

Figure A-2.1—Pressure change at the beginning of CO_2 bulk injection.

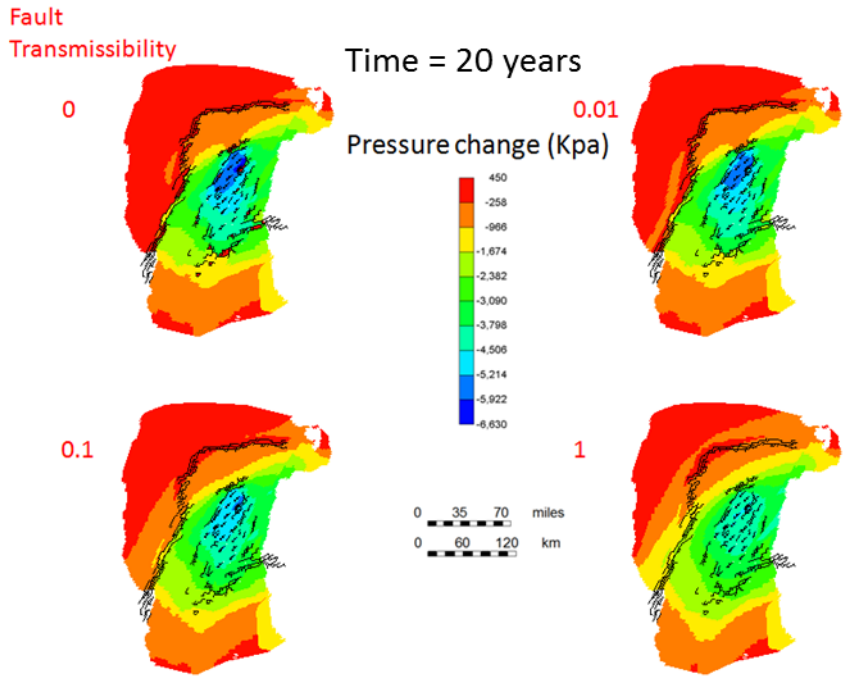

Figure A-2.2—Pressure change at the end of CO_2 bulk injection.

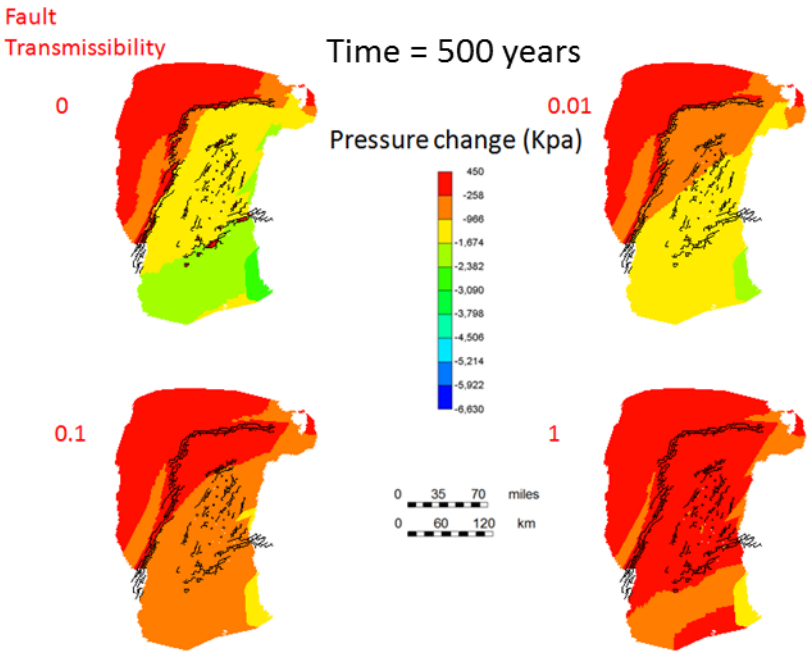

Figure A-2.3—Pressure change after 20 years of CO_2 bulk injection and 500 years monitoring.

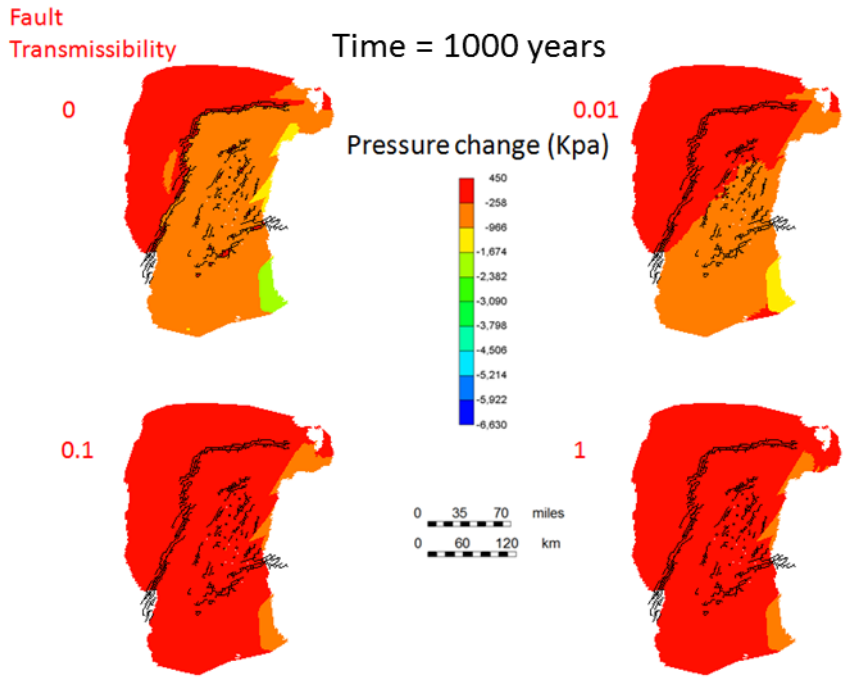

Figure A-2.4— Pressure change after 20 years of CO_2 bulk injection and 1000 years monitoring.

A.3 CO_2-Brine displacement with external brine disposal - CO_2 saturation maps

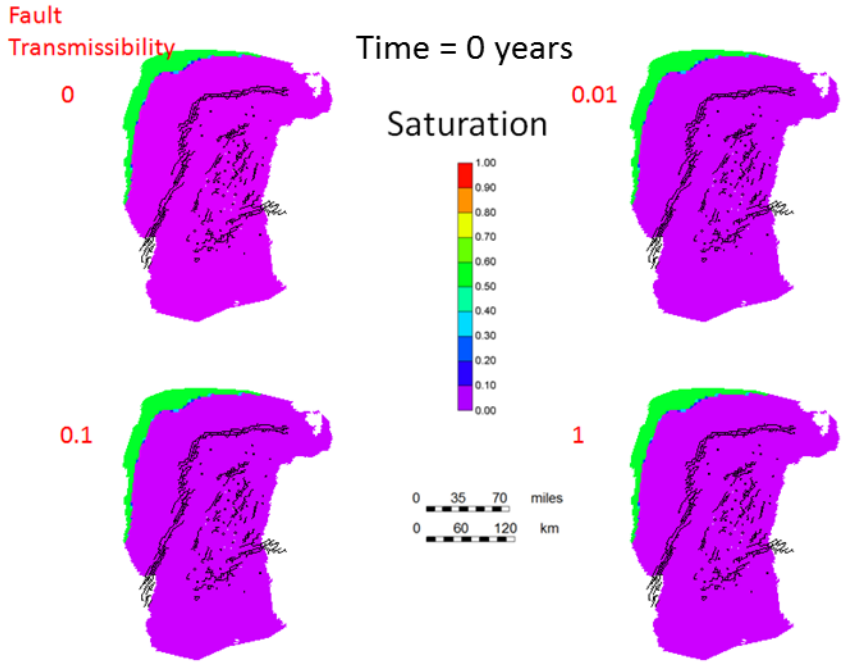

Figure A-3.1—CO_2 saturation at the beginning of CO_2-Brine displacement with external brine disposal.

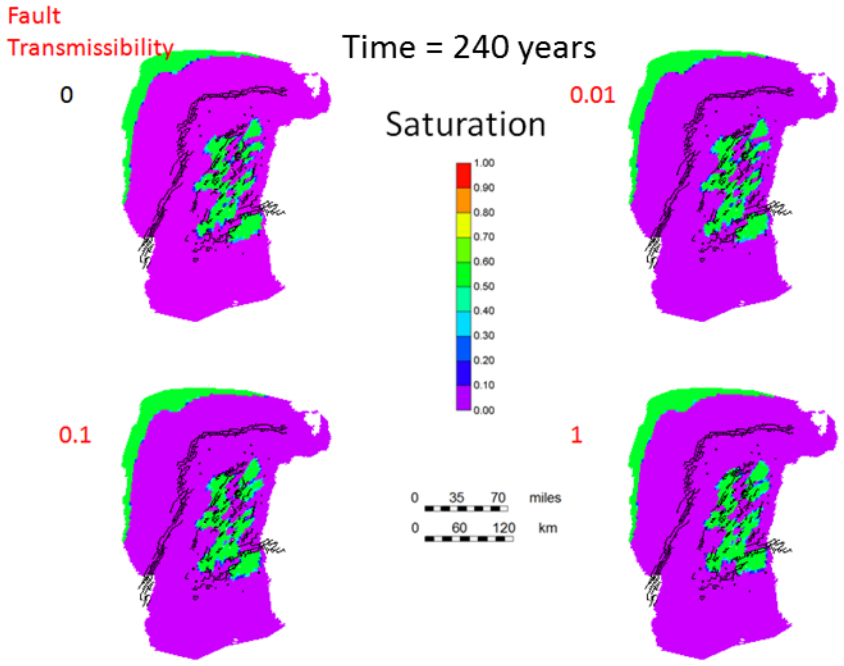

Figure A-3.2—CO_2 saturation at the end of CO_2-Brine displacement with external brine disposal.

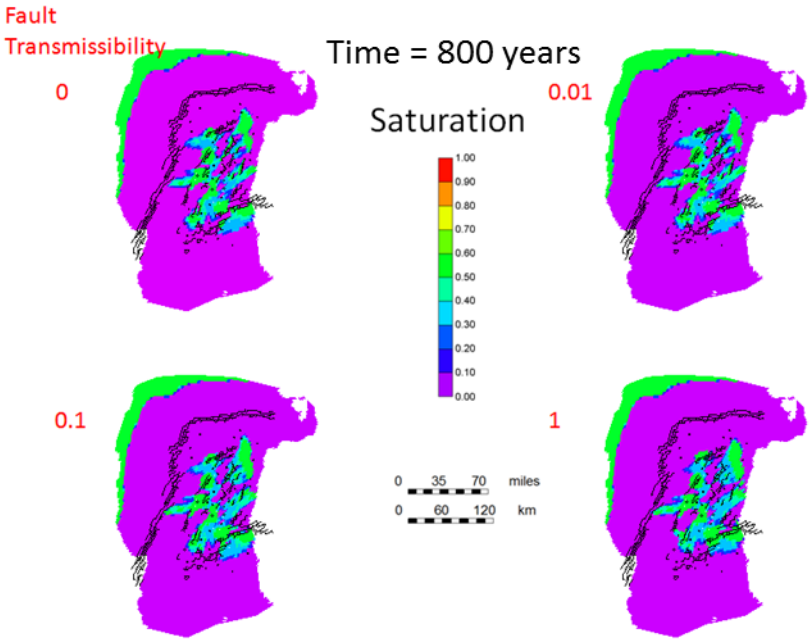

Figure A-3.3—CO_2 saturation after 240 years of CO_2-Brine displacement with external brine disposal and about 500 years monitoring.

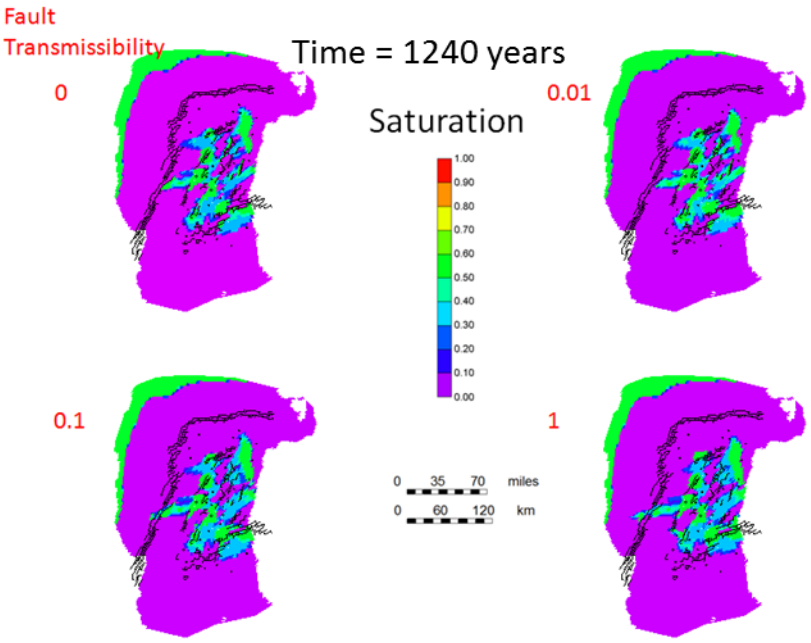

Figure A-3.4—CO_2 saturation after 240 years of CO_2-Brine displacement with external brine disposal and 1000 years monitoring.

A.4 CO_2-Brine displacement with external brine disposal – pressure change maps

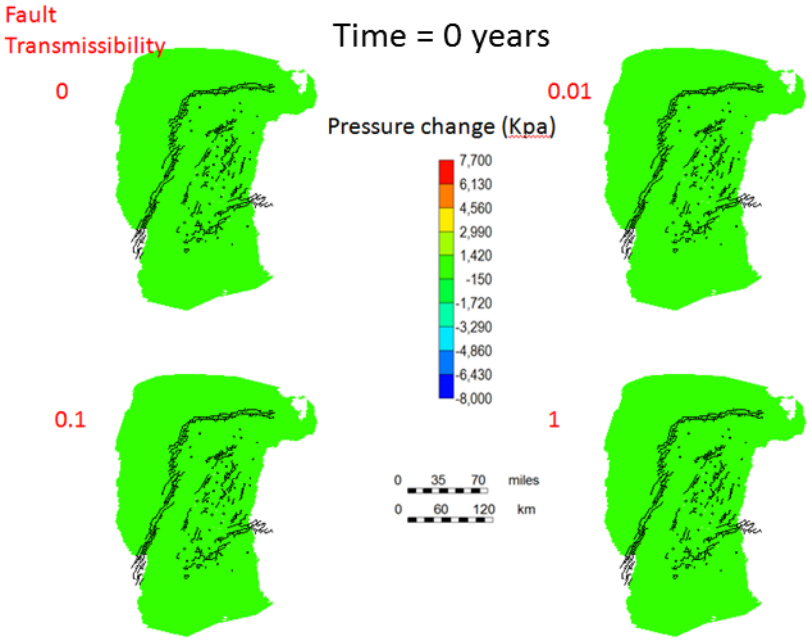

Figure A-4.1—Pressure change at the beginning of CO_2-brine displacement with external brine disposal.

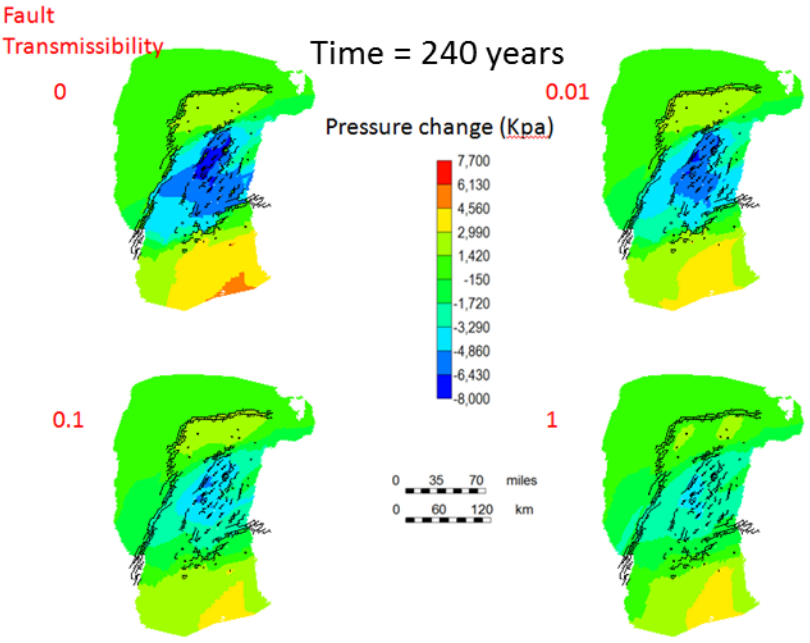

Figure A-4.2—Pressure change at the end of CO_2-brine displacement with external brine disposal.

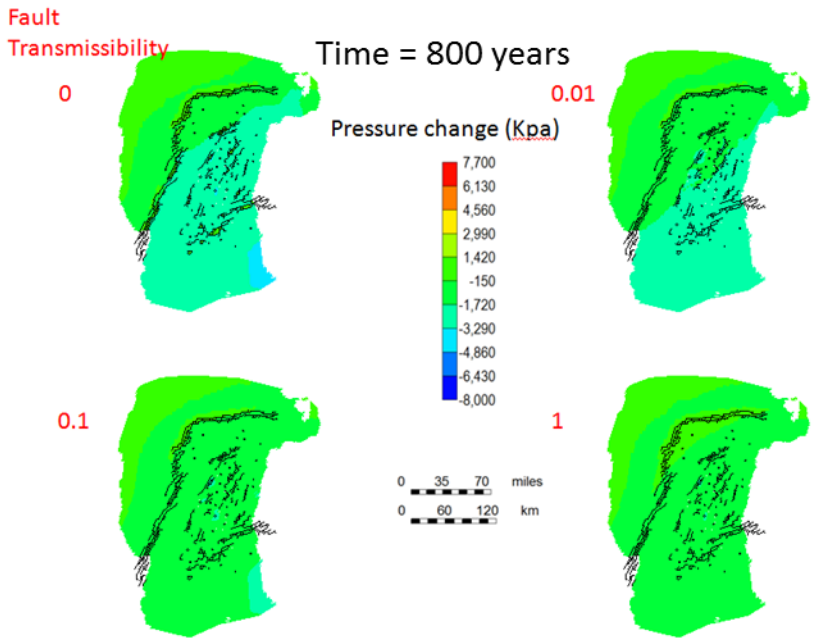

Figure A-4.3—Pressure change after 240 years of CO_2-brine displacement with external brine disposal and about 500 years monitoring.

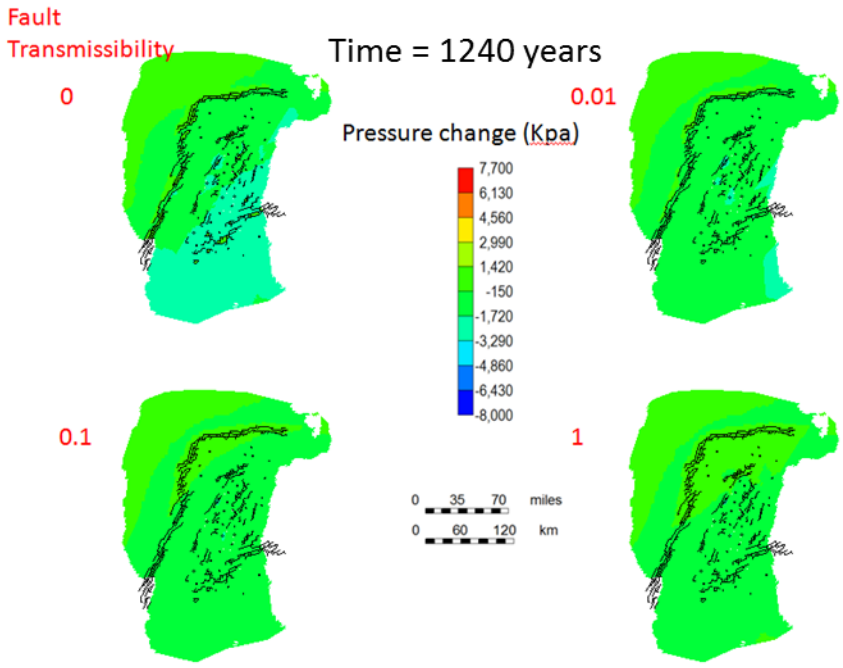

Figure A-4.4—Pressure change after 240 years of CO_2-brine displacement with external brine disposal and 1000 years monitoring.

A.5 CO_2-Brine displacement with internal brine disposal – CO_2 saturation maps

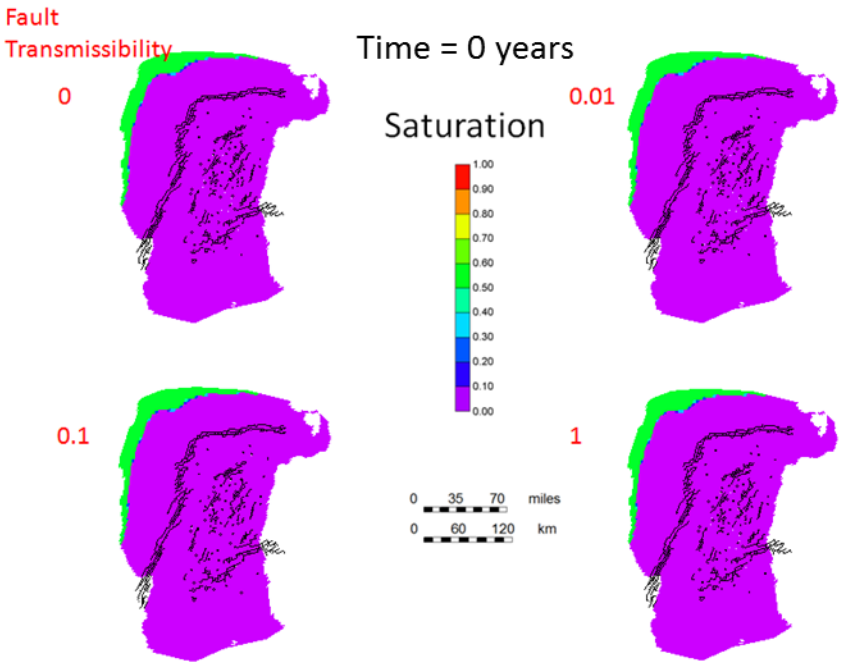

Figure A-5.1—CO_2 saturation at the beginning of CO_2-brine displacement with internal saturated brine reinjection.

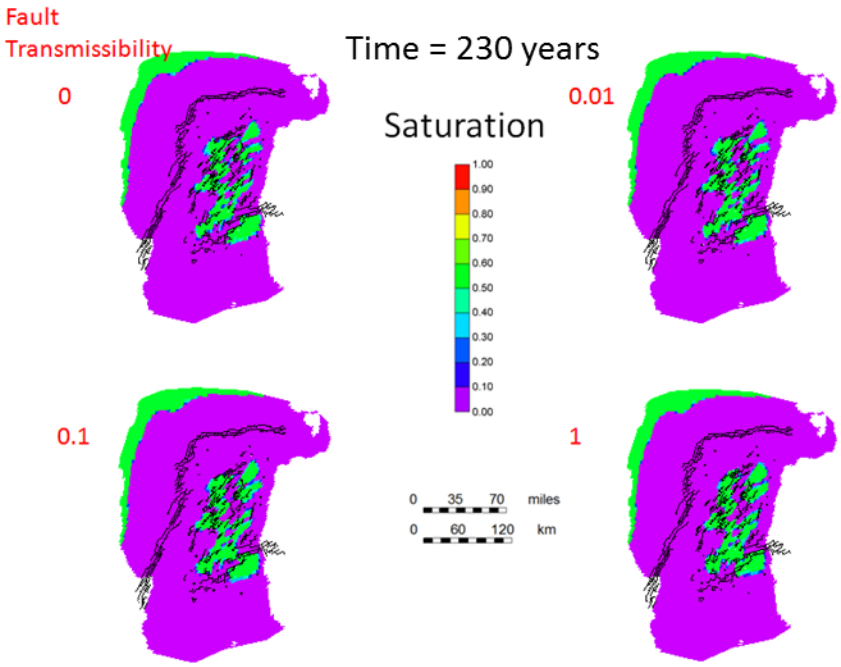

Figure A-5.2—CO_2 saturation at the end of CO_2-brine displacement with internal saturated brine reinjection.

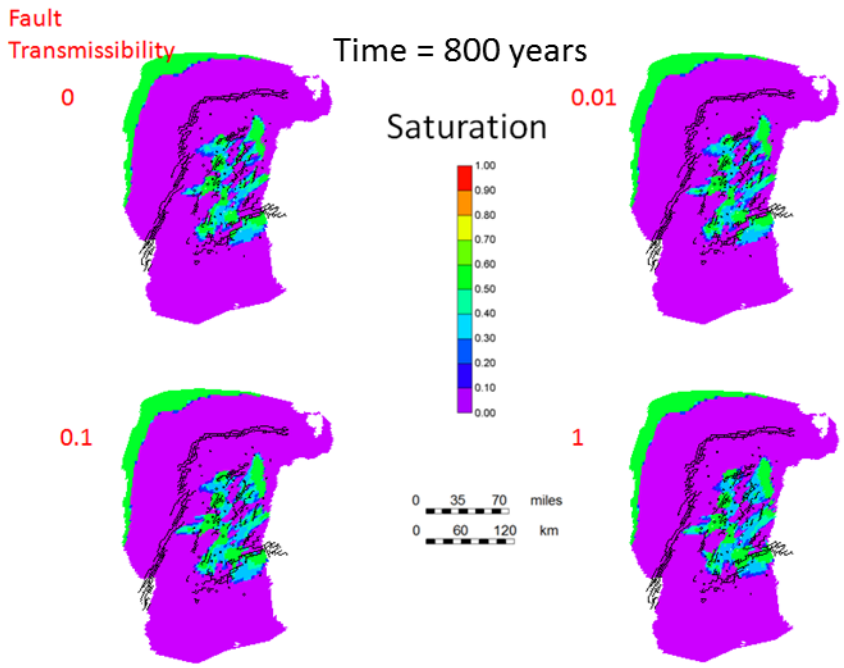

Figure A-5.3—CO_2 saturation after 230 years of CO_2-brine displacement with internal saturated brine reinjection and about 500 years monitoring.

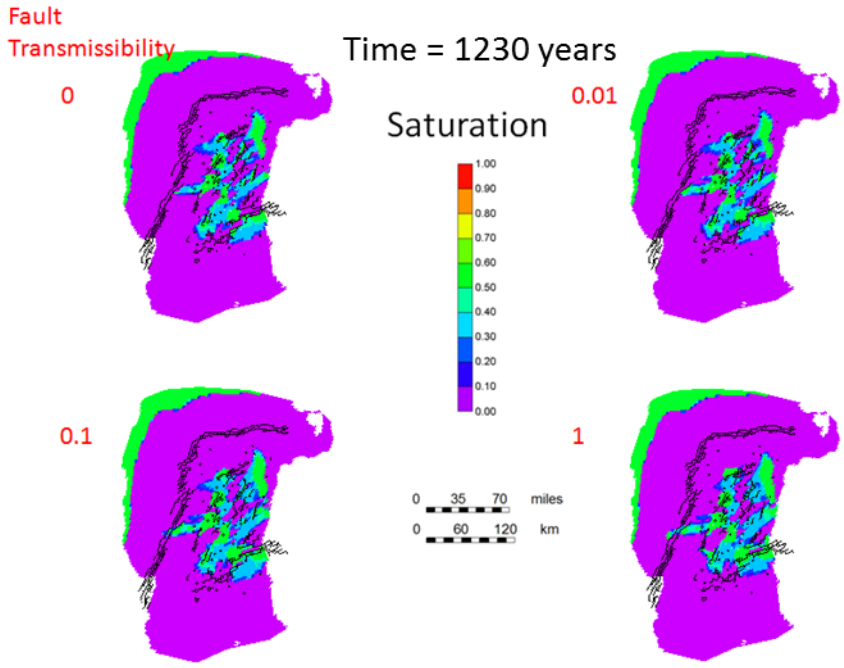

Figure A-5.4—CO_2 saturation after 230 years of CO_2-brine displacement with internal saturated brine reinjection and 1000 years monitoring.

A.6 CO_2-Brine displacement with internal brine disposal – pressure change maps

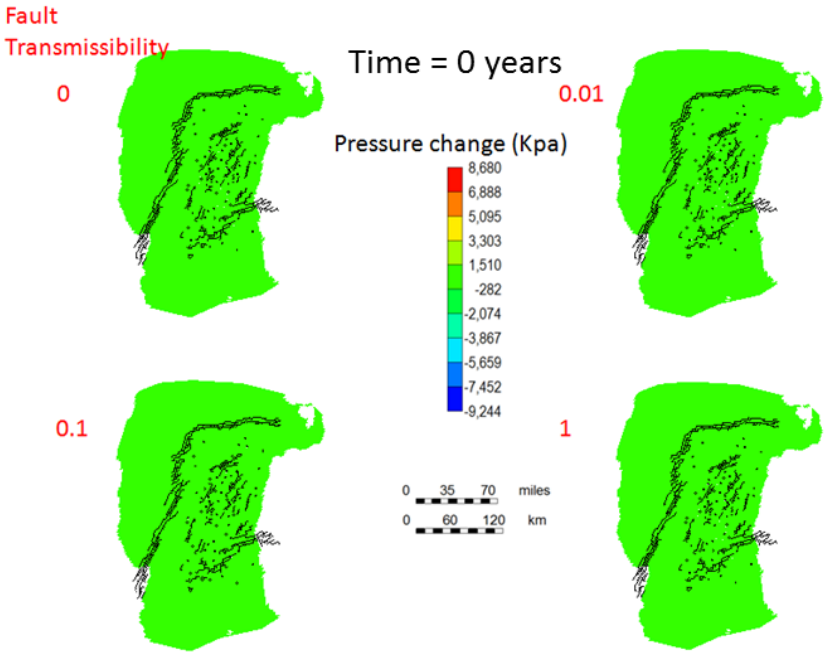

Figure A-6.1—Pressure change at the beginning of CO_2-brine displacement with internal saturated brine reinjection.

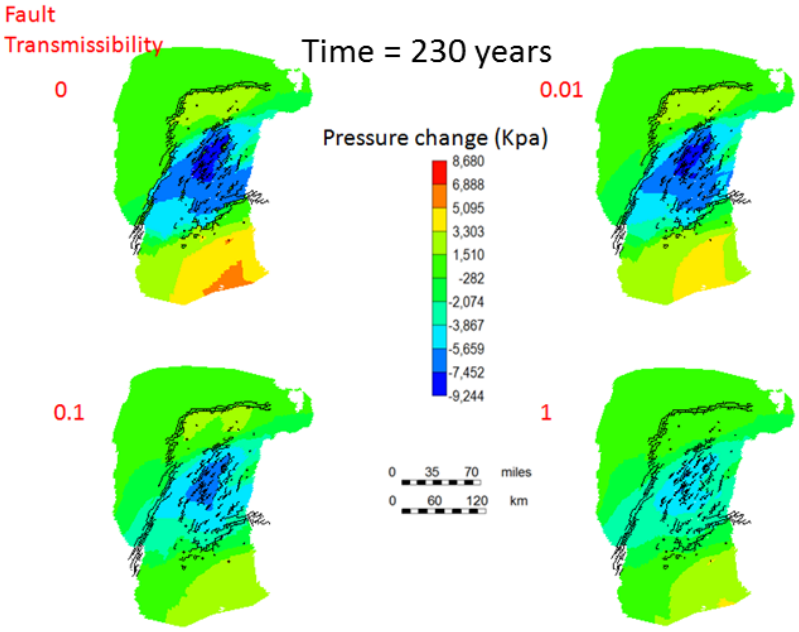

Figure A-6.2— Pressure change at the end of CO_2-brine displacement with internal saturated brine reinjection.

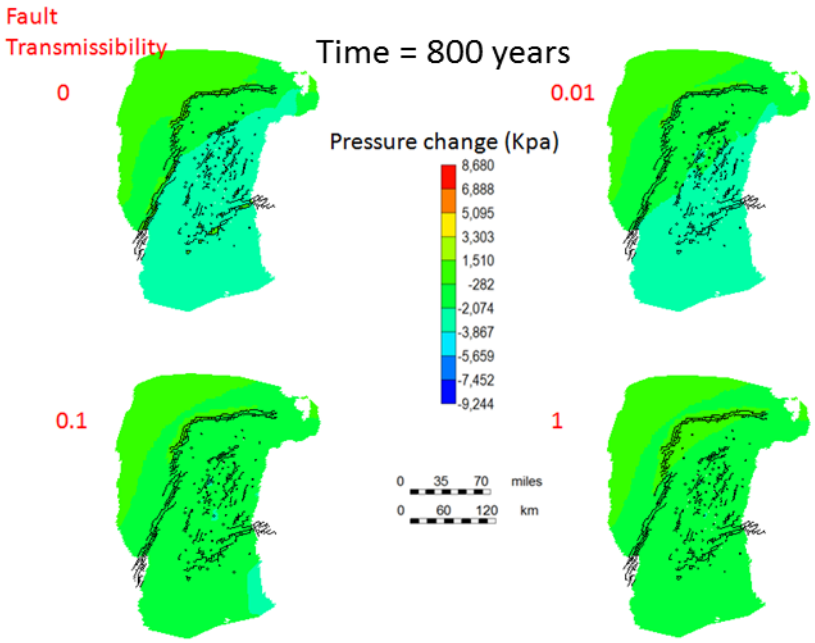

Figure A-6.3— Pressure change after 230 years of CO_2-brine displacement with internal saturated brine reinjection and about 500 years monitoring.

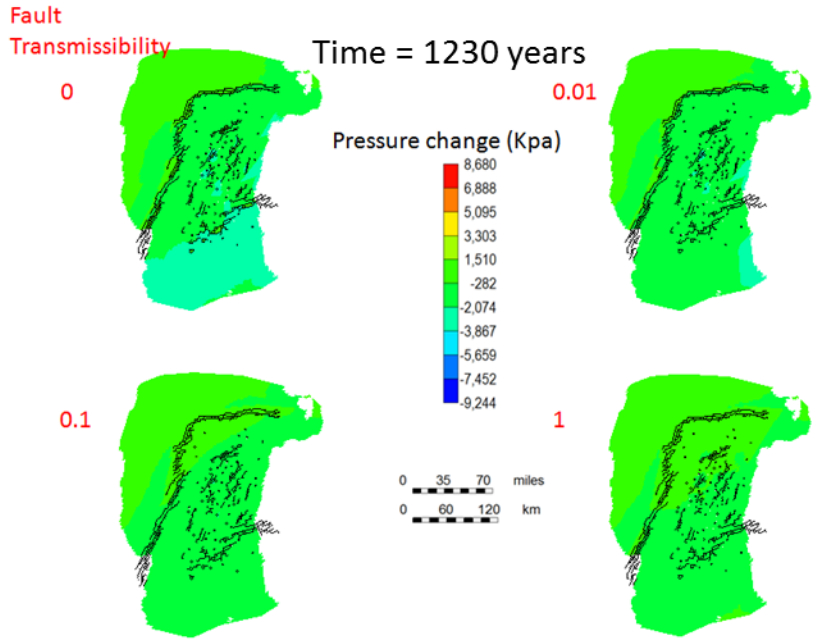

Figure A-6.4— Pressure change after 230 years of CO_2-brine displacement with internal saturated brine reinjection and 1000 years monitoring.

APPENDIX B

INJECTION AND PRODUCTION PRESSURE LOSS

There is frictional pressure loss during CO_2 and brine injection or during brine production depending on the aquifer management strategy being used. The pressure losses in the pipelines are calculated using Equations 5.1 to 5.7 in Chapter V.

Table B-1—CO_2 injection pressure loss

CO_2-INJ	tubing length (m)	ΔP-pipe (MPa)
1	1694	0.164
2	1469	0.143
3	1744	0.169
4	1447	0.141
5	1749	0.170
6	1520	0.148
7	1957	0.190
8	1492	0.145
9	1781	0.173
10	1775	0.172
11	1367	0.133
12	1645	0.160
13	1722	0.167
14	1667	0.162
15	1413	0.137
16	1477	0.143
17	1674	0.162
18	2676	0.260
19	1768	0.172
20	2513	0.244
21	1784	0.173

Table B-2—Brine production pressure loss for CO_2-Brine displacement strategy with external brine disposal

Brine-producer	Q(m^3/d)	tubing length (m)	ΔP (MPa)
1	10,245	1015	0.270
2	10,245	1163	0.310
3	10,245	1146	0.305
4	10,245	1248	0.332
5	10,245	1252	0.333
6	10,245	1321	0.351
7	10,245	1231	0.327
8	10,245	1197	0.318
9	10,245	1078	0.287
10	10,245	1155	0.307
11	10,245	1285	0.342
12	10,245	1493	0.397
13	10,245	1766	0.469
14	10,245	1862	0.495
15	10,245	1095	0.291
16	10,245	1482	0.394
17	10,245	1429	0.380
18	10,245	1129	0.300
19	10,245	1587	0.422
20	10,245	1484	0.395
21	10,245	1931	0.513

Table B-3—Brine production pressure loss for CO_2-brine displacement strategy with internal saturated brine reinjection

Brine-producer	Q(m^3/d)	tubing length(m)	ΔP (MPa)
1	11,730	1015	0.343
2	11,730	1163	0.393
3	11,730	1146	0.388
4	11,730	1248	0.422
5	11,730	1252	0.424
6	11,730	1321	0.447
7	11,730	1231	0.416
8	11,730	1197	0.405
9	11,730	1078	0.365
10	11,730	1155	0.391
11	11,730	1285	0.435
12	11,730	1493	0.505
13	11,730	1766	0.597
14	11,730	1862	0.630
15	11,730	1095	0.370
16	11,730	1482	0.501
17	11,730	1429	0.483
18	11,730	1129	0.382
19	11,730	1587	0.537
20	11,730	1484	0.502
21	11,730	1931	0.653

Table B-4—Brine injection pressure loss for CO_2-brine displacement strategy with internal saturated brine reinjection

Brine-injector	Q(m^3/d)	Tubing length (m)	ΔP (MPa)
1	3460	1015	0.0058
2	3460	1163	0.0066
3	3460	1146	0.0065
4	3460	1248	0.0071
5	3460	1252	0.0071
6	3460	1321	0.0075
7	3460	1231	0.0070
8	3460	1197	0.0068
9	3460	1078	0.0061
10	3460	1155	0.0066
11	3460	1285	0.0073
12	3460	1493	0.0085
13	3460	1766	0.0100
14	3460	1862	0.0106
15	3460	1095	0.0062
16	3460	1482	0.0084
17	3460	1429	0.0081
18	3460	1129	0.0064
19	3460	1587	0.0090
20	3460	1484	0.0084
21	3460	1931	0.0110

APPENDIX C

COMPRESSOR WORK CALCULATION

The saturated vapor pressure of water is 0.10132 MPa at 100ºC. Emerson & Jamieson (1976) showed that the presence of salt lowers the vapor pressure of water according to the following equation, which is valid from 100 to 180ºC.

$$P_1 = P_o 10^{-2.1609\times10^{-4}S - 3.5012\times10^{-7}S^2}$$

Where

P = vapor pressure above salt solution at temperature T (kPa)

P_o = vapor pressure above pure water at temperature T (kPa)

S = Salinity (g salt/kg sea water)

The energy balance across the evaporator is shown in Figure C1

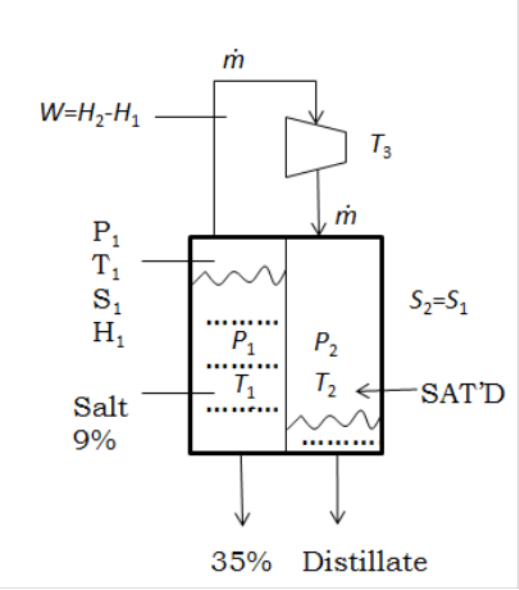

Figure C-1—Evaporator energy balance diagram.

$$\Delta T = T_2 - T_1$$

$$\Delta P = P_2 - P_1$$

$$CR = \frac{P_2}{P_1}$$

For a dry compressor,

$$W = \frac{{H_2}^{vap} - {H_1}^{vap}}{\eta}$$

H_2 = Enthalpy of compressor outlet

H_1 =Enthalpy of compressor inlet

η = Isentropic efficiency

VITA

Name:	Oyewande Ayokunle Akinnikawe
Address:	Department of Petroleum Engineering, Texas A&M University, College Station, TX 77843
Education:	B.S., Chemical Engineering, Obafemi Awolowo University, 2003 M.S., Chemical Engineering, Illinois Institute of Technology, 2006 Ph.D., Petroleum Engineering, Texas A&M University, 2012
Work Experience:	Graduate Research Assistant, Texas A&M University, 2008–2012 Graduate Teaching Assistant for Energy: Sources, Utilization, and Importance to Society (ENGR 101), 2008 – 2011 Energy Engineering Intern, Economides Consultants, 2009
Publications:	Reducing the Green House Gas Emissions from the Transportation Sector, IMETI (2009) Increasing CO_2 Storage Efficiency through a CO_2-Brine Displacement Approach, SPE 139467 (2010)